Escutia, C., Brinkhuis, H., Klaus, A., and the Expedition 318 Scientists
Proceedings of the Integrated Ocean Drilling Program, Volume 318

Methods[1]

Expedition 318 Scientists[2]

Chapter contents

Core recovery and depths

Information assembled in this chapter will help the reader understand the basis for our shipboard observations and preliminary conclusions. It will also enable the interested investigator to identify data and select samples for further analysis. Information presented here concerns only shipboard operations and analyses described in the site chapters. Methods used by various investigators for shore-based analyses of Expedition 318 data will be described in individual publications in various professional journals. This introductory section provides an overview of operations, curatorial conventions, and general core handling and analysis.

Site locations

At all Expedition 318 sites, Global Positioning System (GPS) coordinates from precruise site surveys were used to position the vessel on site. The only seismic system used during the cruise was the Syquest Bathy 2010 CHIRP subbottom profiler, which was monitored on the approach to each site to reconfirm the seafloor depths with those from the precruise survey. Once the vessel was positioned at a site, the thrusters were lowered and a positioning beacon was dropped to the seafloor. The dynamic positioning control of the vessel uses navigational input from the GPS and triangulation to the seafloor beacon, weighted by the estimated positional accuracy (Fig. **F1**). The final hole position was the mean position calculated from the GPS data collected over the time that the hole was occupied.

Drilling operations

The advanced piston corer (APC), extended core barrel (XCB), and rotary core barrel (RCB) systems were used during Expedition 318. These standard coring systems and their characteristics are summarized in Graber et al. (2002). The APC system cuts soft-sediment cores with minimal coring disturbance relative to other Integrated Ocean Drilling Program (IODP) coring systems. After the APC core barrel is lowered through the drill pipe and lands near the bit, the drill pipe is pressured up until the two shear pins that hold the inner barrel attached to the outer barrel fail. The inner barrel then advances into the formation and cuts the core. The driller can detect a successful cut, or "full stroke," from the pressure gauge on the rig floor. The XCB system is deployed when the formation becomes either too stiff for the APC system or when

---

[1] Expedition 318 Scientists, 2011. Methods. *In* Escutia, C., Brinkhuis, H., Klaus, A., and the Expedition 318 Scientists, *Proc. IODP,* 318: Tokyo (Integrated Ocean Drilling Program Management International, Inc.). doi:10.2204/iodp.proc.318.102.2011

[2] **Expedition 318 Scientists' addresses.**

drilling harder substrate such as chert. The XCB cutting shoe (bit) extends as far as ~30.5 cm ahead of the main bit in soft sediments but retracts into the main bit if hard formations are encountered.

APC refusal is conventionally defined in two ways: (1) the piston fails to achieve a complete stroke (as determined from the pump pressure reading) because the formation is too hard or (2) excessive force (>60,000 lb; ~267 kN) is required to pull the core barrel out of the formation. In the case where full or partial stroke can be achieved but excessive force cannot retrieve the barrel, the core barrel can be "drilled over;" after the inner core barrel is successfully shot into the formation, the drill bit is advanced to total depth to free the APC barrel. This strategy allows a hole to be advanced much farther with the APC, the preferred coring tool. Nonmagnetic core barrels are commonly used during all conventional APC coring, but the APC drillover technique is not typically conducted in the first hole at each site if glacial dropstones or other hard rocks might be encountered. Standard steel core barrels were usually used when utilizing the drillover technique because they are stronger than the nonmagnetic barrels.

Most APC/XCB cored intervals were ~9.5 m long, which is the length of a standard core barrel. In some cases, the drill bit can be drilled or "washed" ahead without recovering sediments to advance the drill bit to a target depth where core recovery can be resumed. Such advances are necessary in multiple holes at a site to ensure that coring gaps in one hole were covered by cored intervals in adjacent holes. The amount of advance is usually 1–4 m and accounts for drilling depth shift caused by tides, heave, and other factors (see **"Stratigraphic correlation and composite section"**). An alternative method to adjust the offset is to raise the bit 1–4 m off the bottom of the hole before shooting the next APC core. After any hard horizons are established in Hole A at each site by coring and logging, these intervals can often be drilled through using a center bit to obtain piston cores below. Core recovery information is shown in the "Operations" section of each site chapter.

APC cores can be oriented using the FlexIt tool (see **"Paleomagnetism"**). Formation temperature measurements are usually made in Hole B of each site (see **"Downhole logging"**) so that we could use the formation information from Hole A to avoid any hard layers that might damage the tools. Downhole logging is usually attempted in one hole at each site.

The XCB system was used to advance the hole when APC refusal occurred in a hole before the target depth was reached and when the formation became either too stiff for the APC system or when drilling hard substrate such as cemented layers and nodules or chert. The XCB is a rotary system with a small cutting shoe extending below the large rotary APC/XCB bit. The smaller bit can cut a semi-indurated core with less torque and fluid circulation than the main bit and thus optimizes recovery.

The bottom-hole assembly (BHA) is the lowermost part of the drill string. The exact configuration of the BHA is reported in the "Operations" section in each site chapter. A typical APC/XCB BHA consists of a drill bit (outer diameter = 11⁷⁄₁₆ inches), a bit sub, a seal bore drill collar, a landing saver sub, a modified top sub, a modified head sub, a nonmagnetic drill collar (for APC/XCB), a series of 8 inch (~20.32 cm) drill collars, a tapered drill collar, six joints (two stands) of 5½ inch (~13.97 cm) drill pipe, and one crossover sub. A lockable flapper valve was used so that we could collect downhole logs without dropping the bit when APC/XCB coring.

The RCB system was deployed when the APC or XCB coring rates diminished below an acceptable level or if the bit was destroyed by an increasingly hard formation. Because of the expected drilling conditions caused by glacial deposits and glacially eroded sections, we decided to start with RCB coring at all shelf sites. The RCB is a conventional rotary drilling system and it requires a dedicated RCB BHA and a dedicated RCB drilling bit (outer diameter = 9⅞ inches). A typical BHA for RCB coring includes an RCB drill bit, a mechanical bit release, a modified head sub, an outer core barrel, a modified top sub, and a series of drill collars followed by a tapered drill collar and 5½ inch drill pipe.

IODP depth conventions

For the last few decades, Deep Sea Drilling Project, Ocean Drilling Program (ODP), and IODP Phase 1 reports, diagrams, and publications used three primary designations to reference depth: meters below rig floor (mbrf), meters below seafloor (mbsf), and meters composite depth (mcd). These designations were combinations of origin of depth scales (rig floor or seafloor), measurement units (meters), and method of construction (composite). The designations evolved over many years based on the needs of individual science parties.

Over the course of ODP and IODP scientific drilling, issues with the existing depth scale designations and the lack of a consistent framework became apparent. For example, application of the same designation to scales created with distinctly different tools and methods was common (e.g., mbsf for scales measured by drill string tally and those measured with the wireline). Consequently, new scale-type designations were created ad hoc to differentiate the wireline logging scale from the core depth scale depth-mapping procedures and products could be adequately described. Management and use of multiple maps, composite scales, or splices for a hole or a site was problematic, and the requirement to integrate scientific procedures among three IODP implementing organizations amplified the need to establish a standardized and versatile depth framework.

Given the opportunity offered by the hiatus in IODP drilling operations, a new classification and a nomenclature for depth scale types were defined in 2006–2007 (see IODP Depth Scales Terminology at **www.iodp.org/program-policies/**) (Table **T1**). The framework forms a basis upon which the implementing organizations could address more specific issues of how to manage depth scales, depth maps, and splices. This new depth framework has been implemented within the context of the new Laboratory Information Management System (LIMS; **iodp.tamu.edu/database/index.html**) aboard the R/V *JOIDES Resolution*.

The new methods and nomenclature of calculating sample depth in a hole has changed to be method specific. This will ensure that data acquisition, mapping of scales, and construction of composite scales and splices are unequivocal.

The primary scales are measured by the length of drill string (e.g., drilling depth below rig floor and drilling depth below seafloor [DSF]), length of core recovered (e.g., core depth below seafloor [CSF] and core composite depth below seafloor [CCSF]), and logging wireline (e.g., wireline log depth below rig floor [WRF] and wireline log depth below seafloor [WSF]). All units are in meters. Relationships between scales are either defined by protocol (such as the rules for computation of CSF from DSF) or they are defined based on user-defined correlations (such as stratigraphic correlation of cores between holes to create a common CCSF from the CSF of each hole, or core to log correlation). The distinction in nomenclature should keep the user aware that a nominal depth value at two different scales usually does not refer to the exact same stratigraphic interval.

During Expedition 318, unless otherwise noted, all core depths below seafloor were calculated as CSF-A and CCSF-A and all downhole wireline depths calculated as WSF-A (Table **T1**). For ease of communication of shipboard results, depths are reported in this volume as “mbsf” unless otherwise noted.

Core handling and analysis

As soon as cores arrived on deck, headspace samples were taken using a syringe for immediate hydrocarbon analysis as part of the shipboard safety and pollution prevention program. Core catcher samples were taken for biostratigraphic analysis. Whole-round samples were taken from some core sections for shipboard interstitial water examinations and for microbiological and optical stimulating luminescence age dating. Rhizon interstitial water samples were taken from selected intervals when whole-round samples could not be obtained. (see **“Geochemistry and microbiology”**). In addition, samples were immediately taken from the ends of cut sections for shore-based microbiological analysis.

For the Adélie Drift cores, whole-round core sections were run through the Special Task Multisensor Logger (STMSL), which collects magnetic susceptibility and gamma ray attenuation (GRA) bulk density immediately after entering the core laboratory to facilitate real-time drilling decisions to maximize stratigraphic overlap between holes (see **“Stratigraphic correlation and composite section”**). After the cores reached equilibrium with laboratory temperature (typically after 4 h), whole-round core sections were run through the Whole-Round Multisensor Logger (WRMSL; *P*-wave velocity, density, magnetic susceptibility, and resistivity) and the Natural Gamma Radiation Logger (NGRL). Thermal conductivity measurements were also taken.

The cores were then split lengthwise, from bottom to top, into working and archive halves. Investigators should be aware that older material could have been transported upward on the split face of each section during splitting. The working half of each core was sampled for shipboard biostratigraphy, physical properties, carbonate, paleomagnetism, bulk X-ray diffraction (XRD) mineralogy, and inductively coupled plasma spectroscopy (ICP) and organic geochemical studies. Shipboard sampling was kept to a minimum during Expedition 318 to allow construction of a scientifically appropriate sampling plan at the end of the expedition. Archive-half sections were scanned on the Section Half Multisensor Logger (SHMSL), measured for color reflectance on the Section Half Imaging Logger (SHIL), described visually and by means of smear slides, and finally run through the cryogenic magnetometer.

No core sampling was done on board other than for shipboard analyses and personal samples for research focusing on ephemeral properties. Both halves of the core were then shrink-wrapped, put into labeled plastic tubes, sealed, and transferred to cold storage space aboard the ship. At the end of the expedition, the cores were transferred from the ship into refrigerated trucks and then to cold storage at the IODP Gulf Coast Repository in College Station, Texas (USA).

We modified the core flow for the Adélie Drift cores because of the unique nature of these laminated, potentially high organic content, high sedimentation rate sediments. All whole-round core sections were put though the normal track systems but, when possible, were also put through the cryogenic magnetometer. We only split and processed sections from the first hole. As necessary, these were split one section at a time so that they could be imaged before any alteration occurred as a result of relatively high organic content. Following complete core processing, we subsampled the split sections to prevent any dissolution from acidification of the pore waters. These samples were air dried for postcruise analyses. Once the shipboard analyses were completed, we sealed the core sections along with oxygen absorbers in two layers of shrink-wrap.

Drilling-induced core deformation

Cores may be significantly disturbed and contain extraneous material as a result of the coring and core handling process. In formations with loose sand layers, the sand from intervals higher in the hole may be washed down by the drilling circulation, accumulate at the bottom of the hole, and be sampled with the next core. The top 10–50 cm of each core must therefore be examined critically for potential "fall-in" during description. Common coring-induced deformation includes concave-downward appearance of originally horizontal bedding. In APC cores, the motion of the piston may result in fluidization (flow-in) at the bottom of the cores. Retrieval from depth to the surface may result in elastic rebound. Gas that is in solution at depth may become free and drive apart core segments within the liner. When gas content is high, pressure must be relieved for safety reasons before the cores are cut into segments. This is accomplished by drilling holes into the liner, which forces some sediment out of the liner along with gas. Observed core disturbances are described in the "Lithostratigraphy" section in each site chapter and graphically indicated on the core summary graphic reports ("barrel sheets").

Curatorial procedures and sample depth calculations

Numbering of sites, holes, cores, and samples followed the standard IODP procedure. A full curatorial identifier for a sample consists of the following information: expedition, site, hole, core number, core type, section number, and interval in centimeters measured from the top of the core section and also the sampling tools and volumes taken. For example, a sample identification of "318-U1355A-1H-2, 10–12 cm" represents a sample taken from the interval between 10 and 12 cm below the top of Section 2 of Core 1 ("H" designates that this core was taken with the APC system) of Hole A of Site U1355 during Expedition 318 (Fig. F1). The "U" preceding hole numbers indicates the hole was drilled by the United States Implementing Organization (USIO) platform, the *JOIDES Resolution*. Other core types are designated by "R" for cores taken with the RCB system and "X" for cores taken by the XCB system.

Core intervals are defined by the length of drill string, the seafloor depth, and the amount the driller advances the core barrel, reported in DSF. Once a core is recovered on board, the length of core is measured and this is the "curated" length. The depth of a sample below seafloor (CSF) is calculated by adding the depth of the sample below the section top and the lengths of all higher sections in the core to the core-top depth measured with the drill string (DSF). A soft- to semisoft-sediment core from less than a few hundred meters below seafloor expands upon recovery (typically a few percent to as much as 15%), so the recovered interval does not match the cored interval. In addition, a coring gap typically occurs between cores, as shown by composite depth construction (see **"Stratigraphic correlation and composite section"**). Thus, a discrepancy can exist between the DSF depth and the CSF depth.

For instance, when a recovered core measures >100% of the cored interval, the CSF depth of a sample taken from the bottom of that core will be deeper than that from a sample from the top of the subsequent core. For this expedition, we report all results in the core depth below seafloor method allowing these overlaps (CSF-A) (Table T1), chiefly to avoid confusion during core description and sampling. The primary focus of the Adélie Drift site was to obtain complete sections, so multiple APC holes were drilled to construct a continuous composite sections; these are reported as CCSF. CCSF depths were reported in two manners. CCSF-A is the depth based on a simple alignment of cores from multiple adjacent holes. CCSF-A is generally longer than CSF-A. CCSF-B is the CCSF-A depth divided by a linear scaling factor to "compress" the depth scale to approximate CSF-A.

If a core has incomplete recovery, all cored material is assumed to originate from the top of the drilled interval as a continuous section for curation purposes. The true depth interval within the cored interval is not known. This should be considered as a sampling uncertainty in age-depth analysis and correlation of core data with downhole logging data.

Lithostratigraphy

This section outlines the procedures for documenting the sedimentology of deposits recovered during

Expedition 318, including core description, smear slide description, color spectrophotometry, and XRD of clay mineral preparations. Only general procedures are outlined. All data were uploaded into the IODP-USIO LIMS database and observations were entered using the DESClogik application in Tabular Data Capture mode. DESClogik also includes a graphic display mode for core data (e.g., digital images of section halves and measurement data) that was used for quality control of the uploaded data sets.

Visual core descriptions

Information from macroscopic and smear slide description of each core was recorded manually on visual core description (VCD) forms. Standard sedimentological observations of lithology, sedimentary structures, bioturbation, and diagenesis were made. Entry of descriptive information using the DESClogik program was performed through the Tabular Data Capture mode. Scanned VCD forms were also entered into DESClogik. A template was constructed and tabs and columns were customized to include relevant descriptive information categories (lithology, sedimentary structures, macrofossils, bioturbation, diagenesis, drilling disturbance, clast properties, and clast abundance). A summary description was also entered for each core.

Standard graphic report (barrel sheet)

A simplified one-page graphical representation of each core (barrel sheet) was generated using the LIMS2Excel application and a commercial program (Strater, Golden Software). Barrel sheets are presented with the CSF depth scale, split-core photographs, graphic lithology, and columns for core disturbance, clast abundance, sedimentary structures, macrofossils, diagenesis, bioturbation, shipboard samples, magnetic susceptibility, color reflectance (b*), and GRA density. The graphic lithologies, sedimentary structures, and other visual observations are represented on the barrel sheets by graphic patterns and symbols (Fig. F2). Each barrel sheet also contains the summary description for the core.

Smear slides

Smear slide microscopic analysis was used to determine microfossil constituents and abundance to aid in lithologic classification. Toothpick samples were taken in each lithology and at a frequency of at least one sample every other section (~3 m). For these preparations, the sediment was mixed with distilled water on a glass coverslip and dried on a hot plate at 50°C. The dried sample was then mounted in Norland optical adhesive 61 and fixed in an ultraviolet light box. Type and relative abundance of biogenic and mineralogic components were estimated for each smear slide. Data were entered into LIMS using a custom tabular template in DESClogik.

Lithologic classification scheme

Lithologic terminology for granular sediments and rocks was based on a combination of the classification systems used during ODP Leg 188 and ANDRILL projects (Shipboard Scientific Party, 2001; Naish et al., 2006).

Principal terminology

The principal lithologic name was assigned on the basis of the relative abundances of pelagic biogenic and terrigenous clastic grains.

The principal name of a sediment/rock with <50% pelagic biogenic grains was based on the grain-size characteristics of the terrigenous clastic fraction:

- If the sediment/rocks contain no gravel, then the principal name was determined by the relative abundances of sand, silt, and clay (Fig. F3; after Mazzullo et al.,1988).
- If the sediment/rocks contain terrigenous clastic gravel, then the principal name was determined by the abundance of gravel and the sand/mud ratio of the terrigenous clastic matrix (Fig. F4). This scheme was modified after Moncrieff (1989) to include elements of the Mazzullo et al. (1988) classifications.

The principal name of a sediment/rock with >50% pelagic biogenic grains was classified as an "ooze," modified by the most abundant specific biogenic grain type that forms 50% or more of the sediment/rock (e.g., if diatoms exceed 50%, then the sediment was classified as a "diatom ooze"). However, similar biogenic grain types were grouped together to exceed this 50% abundance threshold (e.g., if diatoms are 40% of the sediment and sponge spicules are 20%, then the sediment was termed "biosiliceous ooze") (Fig. F5).

Major and minor modifiers were applied to any of the principal granular sediment/rock names. The use of major and minor modifiers follows the scheme of ODP Leg 188 (Shipboard Scientific Party, 2001):

- Major modifiers are those components with abundances between 25% and 50% and are indicated by the suffix "-rich" (e.g., "diatom-rich").
- Minor modifiers are those components with abundances of 10%–25% and are indicated by the suffix "-bearing" (e.g., "diatom-bearing").

- If possible, modifiers were assigned on the basis of the most abundant specific grain type (e.g., “silt-rich” or “silt-bearing”).

The Wentworth (1922) scale was used to define grain-size classes. For units with >1% gravel, estimated using the comparison chart of Terry and Chilingar (1955), lithology was defined using the modified Moncrieff (1989) classification scheme.

Clast abundance and properties

Counts were made of the total number of clasts larger than 2 mm in every 10 cm of core. For clasts exceeding 2 cm in width, the lithology, rounding, and surface texture of the clasts was noted separately on the visual core description sheets.

Bioturbation

Ichnofabric description analysis included evaluation of the extent of bioturbation and notation of distinctive biogenic structures. To assess the degree of bioturbation semiquantitatively, the ichnofabric index from Bann et al. (2008) (from 1 to 6) was employed (e.g., 1 = bioturbation absent, 3 = moderate bioturbation, and 6 = total biogenic homogenization of sediment). This index is illustrated using the numerical scale in the Relative Bioturbation column of the barrel sheets. Recognizable biogenic structures and trace fossils were noted and logged in the database.

Core disturbance

Drilling disturbance was characterized in the barrel sheets with the symbols given in Figure F2. Drilling disturbance of relatively soft or firm sediments (i.e., where intergrain motion was possible) was classified into four categories:

1. Slightly disturbed: bedding contacts are slightly bent.
2. Moderately disturbed: bedding contacts are extremely bowed.
3. Extremely disturbed: bedding is completely deformed and may show diapiric or minor flow structures.
4. Soupy: sediments are water saturated and show no traces of original bedding or structure.

Drilling disturbance of lithified sediments (i.e., wherein intergrain motion was not likely because of compaction, cementation, etc.) was classified into five categories:

1. Slightly fractured: core pieces are in place and have very little drilling slurry or brecciation.
2. Moderately fractured: broken core pieces are in place or partly displaced, but original orientation is preserved or recognizable.
3. Moderately fractured or biscuited: core pieces are from the cored interval and are probably in correct stratigraphic sequence (although they may not represent the entire section); intact core pieces are broken into rotated discs (or “biscuits”) as a result of the drilling process.
4. Highly fractured or brecciated: pieces are from the cored interval and are probably in the correct stratigraphic sequence (although they may not represent the entire section), but original orientation is totally lost.
5. Highly fractured or drilling slurry: pieces are from the cored interval and are probably in the correct stratigraphic sequence (although they may not represent the entire section), but original orientation is totally lost; loose pieces of core material are mixed with drilling slurry.

In addition to these main categories for soft and lithified sediments, several other terms were used to characterize drilling disturbance:

- Washed gravel: fine material is suspected to be lost during drilling, with only washed coarse material remaining. This may have resulted from problems in the drilling and recovery of coarse-grained lithologies.
- Flow-in: soupy, displaced sediment pulled into the core liner during retrieval.
- Fall-in: downhole contamination resulting from loose materials falling from the drill hole walls.
- Sand/gravel contamination along core liner: isolated pieces of coarse contamination occurring alongside the core liner away from the core top.

Digital color imaging

The SHIL captures continuous high-resolution images of the archive-half surface for analysis and description. The instrument was used shortly after core splitting in an effort to avoid time-dependent color changes resulting from sediment drying and oxidation. The shipboard system uses a commercial line-scan camera lens (AF Micro Nikkon; 60 mm; 1:2.8 D), with illumination provided by a custom assembly of three pairs of light-emitting diode strip lights that provide constant illumination over a range of surface elevations. Each pair of lights has a color temperature of 6,500 K and emits 90,000 lux at 3 inches. The resolution of the line-scan camera was set at 10 pixels/mm. Users set a crop rectangle for each image to remove extraneous information. Images were saved as high-resolution TIFF files. Available files include the original high-resolution image with grayscale and ruler, as well as reduced JPEG images cropped to show only the section-half surfaces.

Spectrophotometry and colorimetry

The SHMSL employs multiple sensors for the measurement of bulk physical properties in a motorized and computer-controlled section-half logging machine. The sensors included in the SHMSL are reflectance spectroscopy and colorimetry, magnetic susceptibility, and a laser surface analyzer. Reflectance spectroscopy (spectrophotometry) was carried out using an Ocean Optics USB4000 spectrophotometer. This instrument measures the reflectance spectra of the split core from the ultraviolet to near-infrared range. Colorimetric information from split cores is also recorded by this instrument in the L*a*b* color space system. The L*a*b* color space expresses color as a function of lightness (L*) and color values a* and b*, where a* reflects the balance between red (positive a*) and green (negative a*) and b* reflects the balance between yellow (positive b*) and blue (negative b*). When a* and b* are 0, there is no color and L* determines grayscale.

Accurate spectrophotometry using the SHMSL demands a flush contact between the instrument sensors and the split core. A built-in laser surface analyzer aids the recognition of irregularities in the split core surface (e.g., cracks and voids), and data from this tool were recorded in order to provide an independent check on the fidelity of SHMSL measurements.

X-ray diffraction analysis

Selected samples for XRD analysis were obtained from the working halves of the cores at an average spacing of one sample per core. XRD analysis was performed on the clay fraction in most samples. For these preparations, a ~2 g sample was placed in a 50 mL centrifuge tube with 10% acetic acid, sonicated for 15 min, and allowed to stand overnight to remove carbonate material. After centrifuging for 15 min at 1500 rpm, the acetic acid was decanted, 25 mL of distilled water was added, the sample was centrifuged again, and the water was decanted. This washing procedure was repeated two more times to remove both the acid and salts from the sample. After decanting the final wash, 25 mL of 1% sodium metaphosphate solution was added to the sample in a 50 mL beaker. The sample was then placed in a ultrasonic bath for 5 min to suspend the clays by ultrasonic disaggregation and then centrifuged for 5 min at 1000 rpm to settle the >2 µm particles. The clays that remained in suspension were removed from the top ~1 cm of the centrifuge tube and pipetted onto two amorphous quartz sample discs. The sample discs were then left to air dry in a desiccator. After drying, one disc was analyzed and the other solvated with ethylene glycol for ~8 h at 65°C and reanalyzed to determine the presence of expandable clays.

The prepared samples were mounted onto a sample holder and analyzed by XRD using a Bruker D-4 Endeavor diffractometer mounted with a Vantec-1 detector using nickel filtered CuKα radiation. The standard locked coupled scan was as follows:

Voltage = 35 Kv.
Current = 40 mA.
Goniometer scan = 3.5° to 30°2θ.
Step size = ~0.0085°.
Scan speed = 1 s/step.
Divergence slit = 0.3°.

The diffractograms of single samples were evaluated with the Bruker Diffrac-Plus EVA software package. Relative abundances of the major clay mineral groups were established on the basis of maximum peak intensity, preferentially from the glycolated analysis. Quantification of mineral contents was not possible, as the samples were not spiked with a defined amount of a mineral standard for calibration. Therefore, the shipboard results were interpreted qualitatively on the basis of relative occurrences and abundances of the most common clay mineralogical components.

A small number of selected samples were freeze-dried, ground, and mounted on aluminum holders for bulk XRD analysis. Scans of these samples were performed with the same instrument settings as the clay preparations and scanned over a goniometer range of 3.5° to 70°2θ.

Biostratigraphy

Diatoms, organic-walled dinoflagellate cysts, calcareous nannofossils, planktonic and benthic foraminifers, radiolarians, spores, pollen, and other palynomorphs provided preliminary shipboard biostratigraphic and paleoenvironmental information. Ebridians, silicoflagellates, and chrysophyte cysts provided auxiliary biostratigraphic and/or paleoenvironmental information. All microfossil groups were used to characterize water mass changes. In addition, sporomorphs were used to detect influence from land, and benthic foraminifers were used to constrain paleobathymetry.

Shipboard biostratigraphic age assignments were principally based on analysis of core catcher samples. Where necessary, additional toothpick (and/or plug) samples from core material were analyzed for biostratigraphic refinement. Diatoms provided age control for the recent to early Neogene (0–18 Ma) using the constrained optimization (CONOP) average range model by Cody et al. (2008). Cody et al. (2008) use the Gradstein et al. (2004) timescale, which is also adopted for Expedition 318 with the updates outlined by Ogg et al. (2008). This means that all pre-existing biostratigraphic datums tied to older geomagnetic polarity timescales (GPTS) (e.g., Berggren et al., 1995) were recalibrated to the Gradstein et al. (2004) GPTS for Expedition 318 by tying datums to geomagnetic chron boundaries or to a point within chrons (e.g., mid-chron or one-third or two-thirds of a chron, as necessary). We acknowledge the June 2009 ratification of the redefinition of the base of the Pleistocene (see Ogg et al., 2008, and recent revisions), which pushes the Pliostocene/Pleistocene boundary back from 1.806 to 2.588 Ma. Because this change postdates statements in Ogg et al. (2008), we indicate both boundary ages in this report.

Diatoms and radiolarians provided good age control for recent through early Oligocene (<34 Ma), whereas palynomorphs (notably dinoflagellate cysts) were the primary source of age control for the Eocene (>34 Ma). Calcareous nannofossils provided age control for the Oligocene and Oligocene/Miocene boundary interval, whereas planktonic foraminifers provided secondary age control throughout.

Abundance, preservation, and age assignments were entered into LIMS for all identified microfossil taxa. Smear slides made for diatom analysis were also used to document the presence and abundance of other microfossil groups in order to guide additional shipboard (e.g., foraminifers, radiolarians, and calcareous nannofossils) and postcruise (e.g., calcareous nannofossils) sampling efforts.

Siliceous microfossils

Methods

Diatoms, silicoflagellates, ebridians, chrysophyte cysts, and sponge spicules were analyzed from smear slides mounted with Norland optical adhesive 61 (refractive index = 1.56). For radiolarian methods, see the separate section below. Samples with rare to common overall abundance of siliceous microfossils were either disaggregated in distilled water or processed with hydrogen peroxide (H_2O_2) and/or 10% hydrochloric acid (HCl). Strewn slides were prepared from these samples, and, when necessary, the cleaned material was also sieved at >15 µm to improve viewing. Species identification was carried out with Zeiss Axioplan microscopes using bright field illumination at 400×, 630× (oil), and 1000× (oil) magnification. The counting method of Schrader and Gersonde (1978) was utilized for all diatom specimens.

At least two traverses of a 22 mm coverslip were examined (one traverse = 55 fields of view at 630× magnification). An additional scan at 400× was also made to look for age-diagnostic taxa not identified in the first two traverses. Where necessary, taxonomic identification was aided by strewn slide examination at 1000× magnification.

Abundance and preservation

Abundance of individual taxa was quantified by a count tallied over two 22 mm traverses of a smear slide, using 630× magnification. Qualitative siliceous microfossil group abundances were also determined from smear slides, using 630× magnification. Abundance of groups and individual taxa are categorized as follows:

A = abundant (>10 valves per field of view).
C = common (≥1–10 valves per field of view).
F = few (≥1 valve every 10 fields of view and <1 valve per field of view).
R = rare (≥3 valves per traverse and <1 valve per 10 fields of view).
X = trace (<3 valves per traverse, including fragments).
B = barren (no valves or fragments observed).

Preservation of individual siliceous microfossil groups was determined qualitatively and reported in terms of both dissolution/recrystalization and fragmentation as follows:

Dissolution:

G = good preservation (little or no evidence of dissolution and/or recrystallization, primary morphological characteristics only slightly altered, specimens were identifiable to the species level).
M = moderate preservation (specimens exhibit some etching and/or recrystallization, primary morphological characteristics somewhat altered; however, most specimens were identifiable to the species level).
P = poor preservation (specimens were severely etched or overgrown, primary morphological characteristics largely destroyed, specimens often could not be identified at the species and/or generic level).

Fragmentation:

G = good preservation (little or no evidence of fragmentation, specimens were identifiable to the species level).
M = moderate preservation (specimens exhibit some fragmentation, primary morphological characteristics somewhat obscured/lost; however, most specimens were identifiable to the species level).
P = poor preservation (specimens were severely fragmented, primary morphological characteristics largely destroyed; specimens often could not be identified at the species and/or generic level).

Pyritization was also noted and marked as "X" in a separate column in the relevant site chapter tables.

Age assignment and taxonomy

Initial shipboard age assignment of individual samples for 0–18 Ma is mostly based on diatoms using the high-resolution quantitative diatom biochronology by Cody et al. (2008). Species ranges and age assignments are given in Figure F6 and Table T2. We primarily employed the CONOP average range model, drawing on information from the CONOP total range model, where appropriate. We followed the taxonomic concepts of marker species specified comprehensively in appendixes 1a and 1b of Cody et al. (2008).

For strata older than 18 Ma, particularly for the Oligocene and older, age assignment from siliceous microfossils was less well constrained. However, the nearshore biostratigraphic zonation by Olney et al. (2007) was used for nearshore sites for ~18–35 Ma (Fig. F7). For offshore sites older than 18 Ma, the magnetostratigraphically calibrated scheme of Harwood and Maruyama (1992) (to ~35 Ma) was utilized (we updated published ages from the Berggren et al., 1995, timescale to the Gradstein et al., 2004, timescale). Unpublished information by C.E. Stickley for ODP Leg 189 Hole 1172A provided tentative magnetostratigraphically calibrated age information from diatoms, silicoflagellates, and ebridians to ~45 Ma using the unpublished reinterpreted magnetostratigraphy of Hole 1172A by P.K. Bijl (pers. comm., 2010). Silicoflagellates and ebridians provided additional chronostratigraphic information based on various Southern Ocean sites, including the McMurdo Sound Erratics (Bohaty and Harwood, 2000).

Radiolarians

Methods

Samples of sediment, 20 cm^3 in size, were disaggregated by boiling in 35% H_2O_2 with a 1% solution of borax, followed by the addition of 10% HCl to remove carbonate ($CaCO_3$), where present. The samples were washed through a 63 µm mesh sieve and the dried residue was scattered on a glass slide (76 mm × 26 mm), on which gum tragacanth was spread thinly over a small area corresponding to that of a cover glass (40 mm × 24 mm). After moistening to fix the radiolarians on the slide, the free specimens were removed by turning the slide over and patting it gently. Canada balsam (refractive index = 1.55) was used to mount the specimens.

Abundance and preservation

The abundance of radiolarian specimens in one sample is given as

A = abundant (>10,000 specimens in a sample).
C = common (10,000–2,000 specimens in a sample).
F = few (2,000–500 specimens in a sample).
R = rare (<500 specimens in a sample).
B = barren.

The preservation of the radiolarian assemblages is indicated as

VG = very good.
G = good.
M = moderate.
P = poor.

Counts were made to a total of 500 individuals or more per sample. Individual species of radiolarians expressed as a percentage of total radiolarians per sample is given as

A = abundant (>16%).
C = common (4%–16%).
F = few (1%–4%).
R = rare (0.2%–1%).

Zonation scheme

For sediments younger than 23 Ma, the radiolarian zonation scheme and zonal boundary datums follow that by Abelmann (1992) and Lazarus (1992) (Fig. F8). For sediments older than 23 Ma, the lower resolution zonation scheme of Takemura (1992) was used. These zones are (upper to lower) *Lychnocanoma conica, Axoprunum* (?) *irregularis,* and *Eucyrtidium spinosum*.

Calcareous nannofossils

Calcareous nannofossils were encountered during routine smear slide analysis (for diatoms) within Holes U1356A, U1359A–U1359D (mainly U1359D) and U1361A. A representative selection of light microscope images under cross-polarized light was sent off-ship during the expedition to a calcareous nannofossil specialist for preliminary age-assessment.

For additional biostratigraphic information, standard smear slides were processed immediately post-expedition, using Canada balsam mounting medium, and observed in a petrographic polarizing microscope at 1000× magnification.

The abundance of calcareous nannofossils per smear slide is expressed as

A = abundant (>50 nannoliths per field of view)
C = common (10–49 nannoliths per field of view)
F = few (1 to 9 nannoliths per field of view)
R = rare (<1% nannoliths per field of view)
B = barren (no specimens in sample)

The abundance of calcareous nannofossils and/or groups of taxa relative to the total assemblage is categorized as

A = abundant (>50% of the total).
C = common (26%–50% of the total).
F = few (5%–25% of the total).
R = rare (<5% of the total).

Three preservation categories are defined:

G = good (absence of etching and/or overgrowth).
M = moderate (selected specimens with partial dissolution and/or overgrowth).
P = poor (severe dissolution and/or overgrowth; problems identifying specimens).

Zonation scheme

As a general biostratigraphic framework, the calcareous nannofossil standard zonation by Martini (1971) and Okada and Bukry (1980) was used, with additional information from Perch-Nielsen (1985) and Bown (1998). Age assignments were taken from Berggren et al. (1995) and adjusted to the Gradstein et al. (2004) GPTS.

Palynology

Methods

Five to ten grams of sediment was processed per sample, following standard palynologic laboratory protocols as outlined by Brinkhuis et al. (2003a). Briefly, this includes digestion with 30% HCl and 42% hydrofluoric acid (HF) followed by HCl leaching, with centrifuging after each step. Residues were sieved using a nylon 15 µm sieve and strew-mounted on slides using glycerin jelly. For each sample, at least two slides were prepared.

Abundance, preservation, and taxonomy

The following broad palynofacies groups were categorized:

- Marine
- Organic-walled dinoflagellate cysts (dinocysts)
- Foraminifer test linings
- Acritarchs
- Terrestrial
- Sporomorphs
- Black phytoclasts
- Brown phytoclasts
- Fungal spores
- Amorphous organic matter

For qualitative estimates of the abundances of each of these palynofacies groups, the following arbitrary scale was used:

A = abundant.
C = common.
F = few.
T = trace.
B = barren.

When possible, counts of ~150 dinocysts were carried out per sample. Dinocyst taxonomy follows that cited by Fensome and Williams (2004), Fensome et al. (2007, 2008), Clowes and Wilson (2006), Sluijs et al. (2009), and Pross et al. (2010).

Terrestrial palynomorphs identified during these counts were also quantitatively registered, attributing them to five broad categories:

- Saccate pollen
- *Nothofagus* pollen
- Other pollen
- Spores
- Fungal spores

Preservation was qualitatively categorized as one of the following levels:

G = good.
M = moderate.
P = poor.

Age assignments

Over the past ~20 y, numerous marine drill cores and continental sections have been studied for dinocysts throughout the Southern Ocean. The dinocysts provided a suite of regional dinocyst biostratigraphies, such as those from New Zealand (Wilson, 1988; Crouch and Brinkhuis, 2005), Australia (Truswell, 1997), and the Southern Atlantic Ocean (Goodman and Ford, 1983; Wrenn and Hart, 1988). Many of the resulting biozonation schemes are, however, not calibrated to the international timescale (e.g., Gradstein et al., 2004). Moreover, and despite these efforts, the dinocyst biostratigraphy of the Neogene in the Southern Ocean has remained relatively poorly known; in contrast, there are significantly more data available for Paleogene dinocyst events for that region. A first synthesis of magnetostratigraphically calibrated Late Cretaceous–Neogene organic-walled dinocyst events, including those from the Southern Ocean, was provided by Williams et al. (2004). In this synthesis, the southern high-latitude dinocyst bioevents were calibrated to magnetostratigraphically dated successions drilled during Leg 189 using the Gradstein and Ogg (1996) timescale. The most recent update of the integrated magnetostratigraphic dinocyst stratigraphy is presented by Brinkhuis et al. (2009) (Tables T3, T4). This work, which also includes an account of dinocyst events in the high southern latitudes, gives first and last occurrence data for dinocyst taxa calibrated to the Gradstein et al. (2004) timescale. With updates from most recent publications, the data set presented in Tables T3 and

T4 currently provides the best reference point available for dinocyst biostratigraphy of the Antarctic margin.

Planktonic and benthic foraminifers

Methods

Core catcher samples of up to ~20 cm^3 were soaked in a sodium hexametaphosphate solution, disaggregated, wet sieved over a 63 µm sieve, and dried in an oven at 60°C. For more consolidated sediments, samples were treated with potassium hydroxide (KOH) and heated on a hot plate to help disaggregation. Foraminifers were separated and identified under a stereo-binocular microscope.

The abundance of planktonic foraminifers relative to the total sieved residue is categorized as

A = abundant (>50% of the total sieved residue).
C = common (25%–50% of the total sieved residue).
F = few (5%–25% of the total sieved residue).
R = rare (<5% of the total sieved residue).
B = barren (no specimens in sample).

Benthic foraminifer species abundances are recorded as

D = dominant (>50% of total assemblage).
A = abundant (>10%–50% of total assemblage).
C = common (>1%–10% of total assemblage).
F = few (0.1%–1.0% of total assemblage).
R = rare (<0.1% of total assemblage).
B = barren (no specimens observed).

Foraminifer preservation is categorized as

G = good (dissolution effects are rare).
M = moderate (dissolution damage such as etched and partially broken tests or fragments occur frequently).
P = poor (the degree of fragmentation is commonly high and specimens are small, encrusted, and possibly reworked).

Zonation scheme

Planktonic foraminifer zonation and classification follows Berggren (1992a, 1992b) and Berggren et al. (1995), with supplemental ages based on Li et al. (2003). Absolute ages were recalibrated to the Gradstein et al. (2004) GPTS. Taxonomic assignments for planktonic foraminifers follow Kennett and Srinivasan (1983), Leckie et al. (1993), and Pearson et al. (2006).

Whereas benthic foraminifers provide limited biostratigraphic age control, they are most useful for paleoenvironmental reconstruction for Expedition 318. Taxonomic assignments for benthic foraminifers follow Rögl, (1976), Kurihara and Kennett (1986), Leckie and Webb (1986), van Morkhoven et al. (1986), Miller and Katz (1987), Webb (1989), Mackensen et al. (1990), Thomas (1990), Schröder-Adams (1991), Mackensen (1992), Mackensen and Berggren (1992), and Webb and Strong (2006). Paleodepth estimates are based on van Morkhoven et al. (1986) using the following categories:

Neritic = <200 mbsl.
Bathyal = 200–2000 mbsl.
Abyssal = >2000 mbsl.

Paleomagnetism

Samples, instruments, and measurements

Paleomagnetic investigations during Expedition 318 relied on three main types of measurements: (1) those of the natural remanent magnetization (NRM) of archive-half sections before and after alternating-field (AF) demagnetization, (2) those of discrete samples with at least partial AF demagnetization curves and thermal demagnetization on selected specimens, and (3) those of the anisotropy of magnetic susceptibility (AMS) (including bulk magnetic susceptibility, χ). Anhysteretic remanent magnetization (ARM) and isothermal remanent magnetization (IRM) were also studied on selected samples.

Archive halves of cores were measured on the 2G Enterprises cryogenic magnetometer with an inline AF demagnetizer. Discrete samples were measured either on the cryogenic magnetometer or on a spinner magnetometer. AMS and bulk susceptibility were measured with the Kappabridge KLY4-S spinning magnetic susceptometer. ARMs were imparted with the DTech 2000 AF specimen demagnetizer and IRMs were imparted with an ASC impulse magnetizer. Please note that although it is the custom in the paleomagnetic literature to refer to specimens as the objects which are actually measured, in the case of IODP material, there is no difference between the "sample" in the sense of the IODP convention and the specimen in the paleomagnetic sense. We will use the term sample throughout the paleomagnetic reports, by which we mean both sample and specimen.

Cores were not oriented with respect to geographic North during Expedition 318. The sites are quite near the magnetic South Pole. The direction of the geomagnetic field is ~89° up or steeper, and any orientation relying on magnetic methods would be highly unreliable.

The sample and software coordinate systems for the 2G Enterprises Model-760R superconducting rock magnetometer (SRM) and the archive and working halves are shown in Figure F9. Both are "right handed" such that if the $+x$-axis is along the direction of the thumb, the $+y$-axis is along the index finger and the $+z$-axis is along the middle finger. The up arrow is the –*z*-axis by paleomagnetic convention. In order to maintain a consistent reference frame between the two halves of the core, the +*x*-axis is always toward the double lines predrawn onto the core. The core is split so that the double lines are on the working half, so the +*x*-axis is into the core surface for the working half (including discrete samples taken from the working half) and out of the core in the archive half. In the coordinate system defined in the magnetometer software, the +*z*-axis is into the machine and the +*x*-axis is up. The same coordinate system is used in the Molspin Minispin magnetometer.

Discrete samples were taken either in plastic sampling cubes or by sawing the samples into cubes with parallel and cut-off saws. We used the Japanese Natsuhara sampling cubes (7 cm^3), pushing them into the working half with the "up" arrow pointing in the core up direction (Fig. **F10A**). The sample +*x*-axis is toward the double lines on the working half and the up arrow is the –*z*-axis. Sawed samples were scribed with an up arrow and wrapped in parafilm to prevent them from drying out.

The 2G magnetometer software is quite flexible, allowing measurement in any of the 24 possible positions shown in Figure **F10B.** Data are output to files rotated in sample coordinates. The Minispin allows measurement in four or six positions using either a long or short spin time. We used the four position/short spin protocol and simply measured samples multiple times if the circular standard deviation exceeded 5°. Multiple measurements were averaged.

At the high southerly latitudes of our site locations, the magnetic field is presently pointing steeply upward. The reverse direction is steeply downward and unfortunately parallel to the infamous "drill string remanence." Generally speaking, after demagnetization a first-order interpretation would be that "up" directions (–*z*-axis or negative inclinations) are normal and "down" directions (+*z*-axis or positive inclinations) are reverse.

All remanence measurements on the archive halves were made using a 2G Enterprises Model-760R SRM equipped with direct-current superconducting quantum interference devices and an inline, automated AF demagnetizer capable of reaching a peak field of 80 mT. Measurements on the archive halves were taken at 5 cm intervals. We measured the NRM followed by measurements after treatment in alternating fields of 5, 10, 15, and 20 mT on selected cores. After examination of representative demagnetization sequences, a level of demagnetization was chosen that removed the drill string remanence yet preserved enough remanence to be measured on the shipboard magnetometer. Archive halves were demagnetized to either 15 or 20 mT based on these data. In a very few cases, archive halves were demagnetized to 25 mT to ensure that the drill string remanence had been removed to the extent possible.

Because of possible misidentifications of polarity resulting from drill string remanence, we obtained samples from each core, usually one per section. Discrete samples were taken in intervals with the least disturbed bedding (from coring or soft-sediment deformation). These were measured (as time allowed) either in the SRM using a specially designed discrete sample tray (Fig. **F11**) or in the Minispin magnetometer. Because measurement of discrete samples on the 2G magnetometer is not yet done routinely aboard the *JOIDES Resolution*, we attempted to establish a protocol that maximized efficiency while maintaining data reliability.

The discrete sample tray has spaces for 16 samples at 10 cm intervals. This is less than the width of the response function, so we had some concern about interference of sample moments. To investigate this possibility, we made measurements at 0.5 cm intervals on 16 standard samples placed in the top-toward orientation in Figure **F12.** Sample positions are shown as triangles on the right panel and the data acquired by the SRM software are plotted as declination, inclination, and intensity versus track position (centimeters below reference line). From these data, we determined the exact positions of the sample spaces in terms of machine offsets and also determined that for the weak samples encountered during Expedition 318, interference of magnetic moments would not be a problem. We measure 14 samples in a single run, leaving the outermost sample positions empty.

In order to optimize the measurement procedures, we measured seven standard samples using the discrete sample tray (Fig. **F11**) in the 24 possible positions in the SRM (Fig. **F10**). Measurements after subtraction of the background and sample tray measurements are plotted in Figure **F13A.** In general, the circular standard deviations of the replicate measurements were of the order of 5°. It is impractical to measure samples in 24 positions, so we selected three positions that measured each axis along both positive and negative directions: top-toward, top-to-right, and away-up. Means and circular standard deviations for these three selected measurements are shown in Figure **F13B.** The mean of the three measurements was within a few degrees of the means of the original 24 positions; we consider this sufficiently precise for the purposes of this study. Therefore, all cryogenic magnetometer measurements on discrete samples were carried out in these three positions and averaged.

Samples can be demagnetized using the inline AF demagnetizer on the SRM, a Dtech D2000 AF demagnetizer, or the Schonstedt thermal demagnetizer. To compare the Dtech and inline AF demagnetizers, test samples were given an anhysteretic remanence (see below) and demagnetized using the inline AF demagnetizer on the SRM. After remagnetization with a second ARM, they were demagnetized again using the Dtech D2000 AF demagnetizer. For both tests, samples were measured in three positions: top-toward, top-to-right, and away-up. In the inline AF demagnetizer, each specimen was also demagnetized along three axes (*x*, *y*, and *z*) prior to measurement. In the Dtech AF demagnetizer, the specimens were demagnetized along three axes (*x*, *y*, and *z*) and measured in the first position then demagnetized along the *y*-axis and measured in the second position. Finally, the specimens were demagnetized along the *z*-axis and measured in the third position. We show the data for the two experiments in Figure **F14.** Considerable scatter in the measurements can be attributed to both instrument noise (Fig. **F13**) and acquisition of spurious magnetizations in the AF demagnetizers. The fields in the instruments are axial and on the order of tens of nanoTesla, depending on the orientation of the ship, and cannot be demagnetized further. However, no consistent pattern is apparent in the directions acquired, therefore it is not a simple ARM or gyroremanent magnetization (see Tauxe et al., 2010, for details) that would be acquired parallel and perpendicular to the axial field, respectively. In any case, after averaging the three measurements at each step and calculating a best-fit line through the measurements, the directions were within 5° of the known direction of the ARM (along the *x*-axis). Given the ability to measure 14–16 samples in a single demagnetization/measurement sequence, we chose to use the inline SRM AF demagnetizer for analysis of most of the shipboard samples. Each measurement and demagnetization was carried out along the three directions (top-toward, top-to-right, and away-up).

Data from the archive halves and discrete samples were saved in .srm and .dsc file formats and uploaded to LIMS. The data files were also converted to the Magnetics Information Consortium (MagIC) standard format with a set of programs that have been added to the PmagPy software package, available for download at **magician.ucsd.edu/Software/PmagPy.** In particular, we used ODP_srm_magic.py and ODP_dsc_magic.py for the split halves and discrete-sample measurements, respectively. Data downloaded from LIMS in .csv format can be converted to MagIC format using the ODP_csv_magic.py program. The MagIC data format allows analysis of demagnetization diagrams, equal area projections, and various plots versus depth using the standard programs in the PmagPy software package.

We also used the Minispin magnetometer along with the Dtech D2000 AF demagnetizer for certain samples because these instruments can be run in parallel with the cryogenic system. Cross-calibration of intensities is a work in progress, but the directions are completely compatible. Data from the Minispin magnetometer are not currently uploaded into LIMS but can be converted to the MagIC standard format using ODP_spn_magic.py in the PmagPy package. These data are archived by IODP and are available upon request from the IODP Data Librarian.

Our investigations on discrete test samples indicate that demagnetization above ~60 mT with both the inline and Dtech D2000 AF demagnetizers became highly scattered and no longer tracked to the origin, despite averaging (e.g., Fig. **F14**), so discrete samples were not demagnetized above this level.

AMS measurements were made on the Kappabridge KLY4S instrument using the SUFAR program supplied by AGICO, and bulk susceptibility was measured with the SUFAM program. Later in the expedition the AMSSpin program (available for download from **magician.ucsd.edu/Software**) was adapted to the shipboard Kappabridge and used for analysis. This is a much more user-friendly application, and although the data analysis is slightly different than in the AGICO software, the data output are statistically indistinguishable. The Kappabridge measures anisotropy of magnetic susceptibility by rotating the sample along three axes, stacking the data, and calculating the best-fit second-order tensor. It also measures bulk susceptibility (χ). Tensor elements were converted to eigenparameters (eigenvectors V_1, V_2, and V_3 with associated eigenvalues τ_1, τ_2, and τ_3, in which τ_1 is the maximum and τ_3 is the minimum; terminology of Tauxe et al., 2010). These can be interpreted in terms of particle alignment within the sample (Fig. **F15**). Normal sedimentary fabrics are oblate with vertical axes of minimum susceptibility (e.g., Fig. **F15B**). Disturbance by slumping or other deformation generally yields triaxial fabrics (e.g., Fig. **F15D**). We used the bootstrap method of Tauxe et al. (2010) to estimate confidence bounds on AMS eigenparameters.

ARMs can be imparted in the Dtech D2000 AF demagnetizer by applying an alternating field in the presence of a direct-current bias field (Fig. **F16**). In general, ARMs were imparted in an alternating field of 100 mT with a direct-current bias field of 50 µT. Plots of ARM versus susceptibility can be interpreted in terms of changes in grain size and concentration of the magnetic carriers (Fig. **F17;** see Tauxe et al., 2010, for details).

Isothermal remanences were imparted using the ASC impulse magnetizer. These data can be used to characterize magnetic mineralogy and coercivity distributions. Also, when plotted against ARMs or susceptibilities, they can provide information on changes in magnetic grain size and concentration.

Interpretation of magnetostratigraphy

As noted previously, the "drilling remanence" is generally an overprint in a downward directed vertical field. Ordinarily, it is readily distinguished from the original remanent magnetization, but at high latitude it is subparallel or antiparallel to the primary magnetization, making interpretation of polarity zones hazardous. Therefore, we paid careful attention to possible correlations of "polarity zones" with changes in whole-core susceptibility, character of demagnetization diagrams, and possibly also ARM versus susceptibility plots prior to making an interpretation of polarity.

Disturbed sediments, either caused by coring or geological processes (slumping, faulting, etc.) also disturbs the magnetic directions and fabric. High-resolution core photographs were examined for each core section and disturbed intervals were edited out of our magnetic records. Also, the shipboard sedimentologists were frequently consulted during the data editing process.

Once a polarity stratigraphy was established for a given hole, we correlated the pattern to the GPTS (Fig. **F18**). This was done with close collaboration with the shipboard biostratigraphy team. We use the chron terminology of Cande and Kent (1995) and the numerical ages of Gradstein et al. (2004) listed in Table **T5.**

Geochemistry and microbiology

Organic geochemistry

Shipboard organic geochemistry for Expedition 318 was composed of routine analyses of hydrocarbon gas in sediment cores and lipid biomarker reconnaissance.

Description of routine procedures and instrumental analyses used during Expedition 318 are given by Pimmel and Claypool (2001). A detailed description of the nonroutine biomarker analyses is given below.

Hydrocarbon gases

Sediment gas compositions were typically determined once per core. Two sampling methods were employed, headspace sampling and gas void (VAC) sampling using a syringe. Headspace is the gas given off after heating a known quantity of sediment in a vial. VAC is direct extraction of gas from visible expansion voids within the core liner of the recovered core. Sediment plugs for headspace analysis were taken directly after the core was on the catwalk and prepared for analysis by two different methods.

A subsample consisted of 5 cm^3 of sediment, sampled using a cork borer, put in a headspace vial, and crimp-sealed for standard IODP hydrocarbon safety monitoring. When the sediment was too lithified to extract using a cork borer, fragments of core were chiseled out and placed in the vial. The headspace samples for onboard analyses were heated at 70°C for 30 min before injection into the gas chromatograph.

Gases obtained by either headspace or VAC sampling were analyzed by one of two gas chromatography systems, the Agilent/HP 6890 Series II (GC3) or Agilent/HP 6890A natural gas analyzer (NGA). The gases were introduced by injection from a 5 mL syringe directly connected to the gas chromatograph by a 1 cm^3 sample loop. Helium was used as the carrier gas.

The GC3 system determines concentrations of methane (C_1), ethane (C_2), ethene ($C_{2=}$), propane (C_3), and propene ($C_{3=}$) with a flame ionization detector (FID) using a 2.4 m × 3.2 mm stainless steel column packed with 100/120 mesh HayeSep R. Helium was used as the carrier gas, and the gas chromatograph oven temperature was programmed to hold for 0.5 min at 90°C, ramp at 30°C/min to 100°C, ramp at 15°C/min to 110°C, and remain at 110°C for 4.5 min before ramping at 50°C/min to 150°C, with a final holding time of 1.8 min. The FID temperature was 250°C.

The NGA system measures concentrations of C_1–C_7 hydrocarbons with a FID as well as measuring N_2, O_2, and CO_2 with a thermal conductivity detector (TCD). The TCD separation uses three columns, a 6 ft, 2.0 mm inner diameter stainless steel column (Poropak T, 50/80 mesh), a 3 ft, 2.0 mm inner diameter stainless steel molecular sieve column (13×, 60/80 mesh), and a 2.4 m × 3.2 mm stainless steel column packed with 80/100 mesh HayeSep R (Restek). The FID separation was on a DB-1 capillary column (60 m × 0.32 mm) with 1.5 µm phase thickness. The FID separation uses helium as the carrier gas, and the gas chromatograph oven temperature was programmed to hold for 2 min at 50°C, ramp at 8°C/min to 70°C, and then ramp at 25°C/min to 200°C, with a final holding time of 5 min. The FID temperature was 250°C.

Data were collected and evaluated with an Agilent ChemStation data-handling program. For both systems, chromatographic response was calibrated to nine different gas standards with variable quantities of low molecular–weight hydrocarbons, N_2, O_2, CO_2, Ar, and He and checked on a daily basis. The gas components are reported as parts per million by volume (ppmv) of the injected sample. Methane in uppermost headspace samples are also expressed as millimoles per liter of pore volume (mM), assuming a porosity of 0.45, a sample volume of 5 cm^3, and a vial volume of 21.5 cm^3,

C_1 (mM) = ppmv C_1 × ([21.5 – 5]/5)/(23,400 × 0.45) = ppmv C_1 × 0.0003.

Lipid biomarker analysis

Amenable lipids were extracted using a method adapted from Dickson et al. (2009) (Fig. F19). Sediments were freeze-dried using the onboard freeze-drier and homogenized using a grinding machine or pestle and mortar. From 2 to 20 g of the dried, powdered sediment was hydrolyzed and extracted using 10 mL of 0.3 M potassium hydroxide (KOH) in a solution of methanol and 5% water. This involved ultrasonicating for 5 min (3×) and heating in a heating block at 50°C for 2 h. The solvent is removed from the matrix by centrifugation of the sample for 5 min at 3300 rpm and decanted into a 50 mL pear-shaped flask. The sample was further extracted with 7 mL methylene chloride and methanol (3:1; 3×) under ultrasonication for 5 min. The extract solvent was centrifuged and decanted as above, and all extracts were combined in the 50 mL flask. This total lipid extract was concentrated to near dryness using a rotary evaporator under vacuum and was further separated into discrete chemical fractions using methods adapted from Dickson et al. (2009). First, the neutral fraction was recovered using liquid-liquid separation in a test tube. The neutral fraction was further separated into four subfractions using silica gel column chromatography: aliphatic hydrocarbons/*n*-alkanes (N_1), aromatic hydrocarbons (N_2), aldehydes and ketones (N_3), and alcohols (N_4) by elution with *n*-hexane, *n*-hexane/methylene chloride (2:1) mixture, methylene chloride, and methylene chloride/methanol (95:5) mixture, respectively. Alcohols in N_4 were derivatized to trimethylsilyl ethers using BSTFA reagent. Acidic components were extracted with methylene chloride from the remaining solution after acidifying (pH = 1) with HCl. The acidic fraction was concentrated and the carboxylic acids were derivatized to methyl esters with 14% BF_3/methanol at 100°C for 30 min. The methyl esters were recovered using liquid-liquid separation.

The individual lipid fractions were analyzed and structural identification confirmed using an HP 5973 gas chromatograph–mass spectrometer equipped with a 7683 autosampler and fused silica capillary column (DB-1 60 m × 0.317 mm internal diameter × 1.50 µm) and detector. The gas chromatograph oven temperature was programmed to ramp at 30°C/min from 50° to 120°C and then ramp at 5°C/min to 300°C, with a final hold time of 22 min.

Inorganic geochemistry

Interstitial water analyses

Interstitial water analyses for the uppermost 20 mbsf were carried out on cores from Sites U1357 and U1359 in conjunction with sampling for microbiology studies. The sampling strategy is detailed in **"Microbiology."**

Traditional interstitial water squeezing pushes the water out of the sediment by placing it into a titanium squeezer, modified after the stainless steel squeezer of Manheim and Sayles (1974). Gauge pressures up to 20 MPa are applied using a laboratory hydraulic press to extract interstitial water. The interstitial water squeezed out of the sediment was extruded into a prewashed (10% HCl) 50 mL plastic syringe attached to the bottom of the squeezer assembly. The solution was subsequently aliquoted into four parts:

1. One part (10 mL) was filtered through a 0.45 µm polysulfone disposable filter (Whatman) into a centrifuge tube for shipboard routine analyses of salinity, alkalinity and pH, chlorinity, dissolved inorganic carbon (DIC), anions and cations (Cl^-, SO_4^{2-}, Na^+, K^+, Ca^{2+}, and Mg^{2+}), nutrients (PO_4^{3-}, NH_4^+, and $NO_2^- + NO_3^-$), and minor elements (Li, B, Mn, Fe, Sr, Ba, Si, and P).
2. One part (5 mL) was filtered through a 0.45 µm polysulfone disposable filter (Whatman) into a baked small ampoule for shore-based analyses of total organic carbon. $HgCl_2$ (5 µL) was added to each vial.
3. One part (10 mL) was filtered through a 0.45 µm polysulfone disposable filter (Whatman) into a baked large ampoule for shore-based DIC isotope analyses ($\delta^{13}C$). $HgCl_2$ (5 µL) was added to each vial.
4. The remaining interstitial water (at least 7 mL) was filtered though a 0.22 µm polysulfone disposable filter (Millipore) into a baked glass bottle for shore-based analyses of carbohydrate and amino acids.

Salinity, pH, and alkalinity analyses

Interstitial water analyses followed the procedures outlined by Gieskes et al. (1991), Murray et al. (2000), and user manuals for new shipboard instrumentation with modifications as indicated. Interstitial water was analyzed for salinity with a Reichert special scale, previously calibrated using the International Association of Physical Sciences of the Ocean

(IAPSO) seawater standard. Alkalinity and pH were measured after squeezing by Gran titration with a Metrohm autotitrator. The IAPSO seawater standard was used for standardization of alkalinity.

Ion chromatography

Sulfate, chloride, magnesium, calcium, sodium, and potassium concentrations in interstitial water were determined with a Dionex ICS-3000 ion chromatograph on 1:200 diluted aliquots in 18 MΩ water. The IAPSO seawater standard was used for standardization of measurements made on the ion chromatograph.

Spectrophotometric analyses

Phosphate, ammonium, and total nitrate and nitrite concentrations in the interstitial water were determined by an OI Analytical DA3500 discrete analyzer spectrophotometer unit, an automated system that controls sample analysis and reagent aspiration, dispensing, heating, and mixing. In the phosphate method, orthophosphate reacts with Mo(VI) and Sb(III) in an acidic solution to form an antimony phosphomolybdate complex. Ascorbic acid reduces this complex to form a blue color, measured at 880 nm. Potassium phosphate monobasic (KH_2PO_4) was used to produce a calibration curve and as an internal standard. In the ammonium method, phenol undergoes diazotization and the subsequent diazo compound is oxidized by sodium hypochlorite to yield a blue color, measured spectrophotometrically at 640 nm. Ammonium chloride (NH_4Cl) was used to produce a calibration curve and as an internal standard. In the nitrate/nitrite method, the sample passes through an open-tubular copperized cadmium coil, which reduces nitrate to nitrite. Both the reduced nitrate and any pre-existing nitrite are diazotized with sulfanilamide and coupled with *N*-(1-naphthyl)ethylenediamine dihydrochloride to form a colored azo dye, measured spectrophotometrically at 540 nm.

Major and trace element analyses by ICP-AES

Concentrations of selected elements (Li, B, Mn, Fe, Sr, Ba, and Si) in the interstitial waters were determined by inductively coupled plasma–atomic emission spectroscopy (ICP-AES) with a Teledyne Prodigy high-dispersion ICP-AES. The method for shipboard ICP-AES analysis of samples is described in detail in ODP *Technical Note 29* (Murray et al., 2000).

Each batch of ~20 samples run on the ICP-AES contained 6 artificial standards of known increasing concentrations for all elements of interest, as well as 2 additional standards to monitor instrumental drift. Samples were analyzed in batches to take advantage of achieved calibration and each sample was analyzed three times from the same dilute solution (i.e., in triplicate) within a given sample run. Samples and standards were diluted 1:10 prior to analyses using 2% HNO_3.

Following each run of the instrument, the measured raw-intensity values are transferred to a data file. Instrumental drift was negligible during swift analyses of pore waters, and therefore no correction was applied. A calibration line for each element was calculated using the results for the known standard solutions. Element concentrations in the samples were subsequently calculated from the relevant calibration line. Replicate analyses of one of the artificial standards was used to estimate precision and accuracy for minor elements, which typically was between 2% and 5%, except for Si runs from Site U1357 (5%–10% errors).

Dissolved inorganic carbon

A portion of undiluted interstitial water (2 mL) was used to determine DIC using a UIC 5011 CO_2 coulometer. Accuracy during individual batches of analyses was determined by running 500 µL of a 100 mM Na_2CO_3 standard every 10 samples. Reproducibility for this standard throughout the course of sample analyses was within 1%.

Sediment samples

We routinely took one 5 cm^3 sample of sediment for bulk geochemistry from the working half of each core. The samples were selected in collaboration with the sedimentologists to represent the major lithologic units recovered, or any layer of special interest. Samples for geochemistry were freeze-dried for ~12 h and crushed to a fine powder using a pestle and agate mortar. Geochemical analyses carried out included percent carbonate and elemental analyses of carbon, nitrogen, and sulfur, as well as major and minor element geochemistry (ICP-AES).

For intervals sampled for microbiology, squeeze cakes from the interstitial water samples were freeze-dried for onshore elemental analyses (C/N) and analyses of amino acids and carbohydrates.

Inorganic carbon and carbonate

Freeze-dried and ground sediment (10–20 mg) was reacted with 1 N HCl. The liberated CO_2 was backtitrated to a colorimetric end point. Sediment carbonate content (in weight percent) is calculated from inorganic carbon (IC) content by assuming all carbonate occurs as calcium carbonate:

$$CaCO_3 = IC \times 8.33.$$

Inorganic carbon content of sediment samples was determined using a UIC 5011 CO_2 coulometer. Accuracy during individual batches of analyses was determined by running a carbonate standard (100 wt% $CaCO_3$) every 10 samples. Reproducibility of the standard was found to be within 1%.

Elemental analyses (C, N, and S)

Freeze-dried and ground sediment (10–15 mg) was weighed into tin cups. After addition of a vanadium pentoxide catalyst, the sample was combusted in a stream of oxygen at 1800°C. The reaction gases were passed through a reduction chamber to reduce nitrogen oxides to nitrogen and sulfur trioxide to sulfur dioxide. Gases were subsequently separated by a chromatographic column before detection by thermal conductivity.

Total carbon, nitrogen, and sulfur contents of sediment samples were determined with a ThermoElectron Corporation FlashEA 1112 carbon-hydrogen-nitrogen-sulfur (CHNS) elemental analyzer equipped with a ThermoElectron packed column CHNS/NCS and a thermal conductivity detector. All measurements were calibrated to a sulfanilamide standard, which was run every 10 samples and yielded reproducibilities of 1–2 wt% for carbon and nitrogen and 3–5 wt% for sulfur.

Total organic carbon (TOC_{DIFF}) content was calculated as the difference between total carbon (TC) and inorganic carbon (IC) from coulometry:

$$TOC_{DIFF} = TC - IC.$$

Major and trace element analyses by ICP-AES

The method for shipboard ICP-AES analysis of bulk rock samples was described in detail in ODP *Technical Note 29* (Murray et al., 2000). The following protocol is an abbreviated form of this procedure with minor modifications. For flux fusion, 100 mg of ground and homogenized sediment was weighed and added to a vial containing 400 mg of preweighed lithium metaborate ($LiBO_2$) powder (sample flux = 1:4). All samples and standards were weighed on the Cahn C-31 microbalance, with typical weighing errors around ±0.05 mg under relatively smooth sea-surface conditions and ±0.1 mg in rougher seas. When weighing errors were significantly larger, sample processing was halted until calmer seas were reached again. After homogenization of both powders, the mixture was poured into a Pt-Au crucible and 10 µL of 0.172 µM LiBr was added to prevent the cooled bead from sticking to the crucible. Samples were fused individually at 1050°C for ~12 min in an internal-rotating induction furnace (Bead Sampler NT-2100) and subsequently cooled to form a bead. After cooling, the bead was dissolved in 50 mL of 10% HNO_3 (trace metal grade) in an acid-washed high-density polypropylene (HDPE) Nalgene wide-mouth bottle, which was then agitated on a Burrell wrist-action bottle shaker for 1.5 h. After complete sample dissolution, samples were filtered through a 0.45 µm Acrodisc into an acid-washed 60 mL HDPE Nalgene bottle. Next, 1.25 mL aliquots of this filtered solution were transferred to scintillation vials and diluted with 8.75 mL of 10% HNO_3 for triplicate analysis by ICP-AES (final dilution factor for each sample = ~4000).

Each batch of 20–30 samples run on the ICP-AES contained two procedural blanks, six referenced standards (BHVO-2, BCR-2, JG-2, SO-1, LKSD-1, and RGM-1), and 5–10 drift standards (BHVO-2) to monitor instrumental drift. Samples were analyzed in batches to take advantage of achieved calibration, and each sample was analyzed three times from the same dilute solution (i.e., in triplicate) within a given sample run.

We determined major (Si, Ti, Al, Fe, Mn, Ca, Na, K, and P) and trace (Ba, Sr, V, Sc, and Co) element concentrations. Following each run of the instrument, the measured raw-intensity values were transferred to a data file and corrected for instrument drift and procedural blank. Drift correction was applied to each element by linear interpolation between the drift-monitoring solutions. After drift correction and blank subtraction, a calibration line for each element was calculated using the results for certified rock standards. Element concentrations in the samples were then calculated from the relevant calibration lines. Replicate analyses of rock standards was used to estimate precision and accuracy for major and trace elements, which were between 5% and 20%, dependent on the element of interest.

Microbiology

Core handling and sampling

Microbiology sampling was carried out for Holes U1357C and U1359B. Core sections dedicated to microbiology were handled with aseptic techniques to minimize contamination, as previously described for ODP Leg 201 (Shipboard Scientific Party, 2003; adjustments as described below).

Whole-round samples 10 cm in length were taken at high resolution for microbiology in the uppermost 20 mbsf. Sampling intervals were approximately every 20 cm within the top 4 mbsf, every 30 cm from 4 to 6 mbsf, every 50 cm from 5 to 10 mbsf, and every 1 m from 10 to 20 mbsf. Whole-round samples for interstitial waters were taken adjacent to all microbiology samples. Microbiology whole-round samples were cut using sterilized spatulas, capped with sterilized end caps, and immediately brought to the cold room (<8°C) for subsampling.

Beyond the uppermost 20 m, 5 mL samples were taken with a sterile 5 mL syringe barrel from the bottom of approximately every fourth section at Sites U1357 and U1359. Before sampling, the bottom of each section was scraped with a sterile spatula. The samples were immediately frozen at –80°C for onshore deoxyribonucleic acid analyses.

Further handling of the microbiology whole-round samples was done under a laminar flow hood in the cold room utilizing sterile techniques. Within the hood, each whole-round was removed from the core liner, and the surface was carefully scraped with a sterile scalpel to remove potential contamination from seawater and sediment smearing. A subsample from each whole-round sample was taken with a sterile 5 mL syringe barrel, stored frozen at –80°C in a 2 oz whirlpak bag, and saved for onshore molecular analysis. After subsampling, the remaining whole-round sample was placed into large whirlpak bags, which were gently folded over and placed into vacuum seal bags. Oxygen scrubbers were added to each vacuum-sealed bag to scavenge any remaining oxygen. Sealed samples were stored at –80°C for onshore analysis.

Physical properties

Expedition 318 physical property shipboard measurements were made in order to characterize lithologic units and detect changes in sediment properties that could be related to lithologic changes, diagenetic features, or consolidation history. Furthermore, these measurements aid to identify natural and/or coring induced discontinuities and the interpretation of seismic reflection and downhole geophysical logs. The primary objectives of the Expedition 318 physical property program were to collect medium-resolution data for

- Examining variations in physical properties related to the variations in sediment composition (and therefore depositional history) on the Wilkes Land margin;
- Providing estimates of sediment properties, which can be used to reconstruct glacial and interglacial/proglacial depositional processes;
- More fully understanding the strength of hemipelagic sediments in the context of sea level change, sequence stratigraphy, and possible changes of physical properties across unconformities;
- Investigating data sets to aid in the interpretation of seismic reflection and downhole geophysical measurements, including the construction of synthetic seismograms;
- Providing porosity information to construct quantitative algorithms used to decompact the sediments recovered by the backstripping method to resolve any possible eustatic signal recovered; and
- Facilitating hole to hole correlation, thereby allowing real-time stratigraphic correlation and feedback to the drillers, and the construction of a composite stratigraphic section for multiply cored sites.

Physical properties were measured on whole-round sections with the WRMSL. After being brought in from the catwalk, sections were allowed to equilibrate to ambient room temperature (i.e., 20°–22°C) to ensure thermal homogeneity in order to minimize temperature effects on physical property measurements and to protect sensors from damage. The WRMSL incorporates a GRA density meter, a magnetic susceptibility loop sensor, and a compressional *P*-wave velocity logger (PWL).

For Sites U1357 and U1359, where multiple holes were drilled, we also used the STMSL. The purpose of the STMSL during Expedition 318 was to rapidly record medium- to high-resolution sets of GRA density and magnetic susceptibility data. The GRA bulk density meter and magnetic susceptibility loop incorporated in the STMSL are effectively identical to those of the WRMSL. The spacing distance between STMSL measurements was typically 5 cm for GRA density and magnetic susceptibility measurements. Scanning time averaged 8 s per measurement.

Natural gamma radiation (NGR) was also measured on whole-round sections using the NGRL. Moisture and density (MAD) measurements were made on discrete samples taken from the section halves. Bulk properties determined by MAD analyses include wet bulk density, dry bulk density, grain density, water content, and porosity (Blum, 1997).

Whole-Round Multisensor Logger and Special Task Multisensor Logger measurements

GRA bulk density, magnetic susceptibility, and compressional *P*-wave velocity were measured nondestructively with the WRMSL on all whole-round core sections. The quality of the WRMSL data is highly dependent on the condition of the core. To optimize WRMSL performance, sampling intervals and measurement residence times were the same for all sensors for any one core. Sampling intervals were set at 2.5 cm for density and magnetic susceptibility and 5 cm for *P*-wave velocity, and integration times were set for 10 s for GRA density and 2 s for magnetic susceptibility. These intervals and integration times were set so that a 9.5 m long core would take ~1.2 h to pass through the WRMSL, taking ~14 s per point of measurement. These sampling intervals are common denominators of the distances between the sensors installed on the WRMSL (30–50 cm) and allowed a combination of sequential measurements that optimized the total measurement time. On the STMSL the sampling intervals for the two sensors were set at 5 cm so that a 9.5 m long core took <40 min.

Gamma ray attenuation bulk density

Bulk density reflects the combined effect of the lithology, variations in porosity, grain density (dominant mineralogy), and coring disturbance. Porosity is mainly controlled by lithology, texture, compaction, and cementation (controlled by both mechanical and chemical processes).

Because the attenuation coefficient is similar for most common minerals and aluminum, bulk density was obtained through direct calibration of the density meter using aluminum rods of different diameters mounted in a core liner that is filled with distilled water. The GRA density meter has a spatial resolution of <1 cm. The GRA density meter uses a 10 mCi ^{137}Cs capsule as the gamma ray source (with the principal energy peak at 0.662 MeV) and a scintillation detector. The narrow collimated peak is attenuated as it passes through the center of the core. Incident photons are scattered by the electrons of the sediment material by Compton scattering.

The attenuation of the incident intensity (I_0) is directly related to the electron density in the sediment core of diameter D, which can be related to bulk density given the average attenuation coefficient (in micrometers) of the sediment (Evans, 1965; Harms and Choquette, 1965).

Magnetic susceptibility

Magnetic susceptibility provides information on the magnetic composition of the sediments that can often be related to mineralogical composition (e.g., terrigenous versus biogenic materials) and diagenetic overprinting. Sediments rich in biogenic opal have generally low to negative magnetic susceptibility because practically no clay or magnetite is present. In such cases, measured values approach the detection limit of magnetic susceptibility sensors.

Magnetic susceptibility was measured with the Bartington Instruments MS2C system with a loop sensor on the WRMSL. The magnetic susceptibility loop operates at a frequency of 621 Hz. The output of the magnetic susceptibility sensors was set to the IODP standard SI unit setting. However, to actually obtain the dimensionless SI volume-specific magnetic susceptibility values, the instrument units stored in the IODP database must be multiplied by a correction factor to compensate for instrument scaling and the geometric ratio, including core disturbance, between core and loop dimensions. This correction was not undertaken during Expedition 318, and all magnetic susceptibility values are therefore relative (instrument units).

P-wave velocity

P-wave velocity varies with lithology, porosity, and bulk density of material; state of stress; temperature; and fabric or degree of fracturing. In marine sediments and rocks, velocity is controlled by degree of consolidation and lithification, fracturing, and occurrence and abundance of free gas and gas hydrate. Microscopic and macroscopic fracturing may completely attenuate the signal so that it is not possible to obtain data from the PWL. Together with bulk density, velocity data are used to derive porosities and to calculate acoustic impedance and reflection coefficients that can be used to construct synthetic seismograms and to estimate the depths of seismic horizons.

P-wave velocities were measured with the PWL on the WRMSL and with the *P*-wave caliper (PWC) and *P*-wave bayonets (PWB). The PWL measures the ultrasonic *P*-wave velocity of the whole-round sample in the core liner. The PWV and PWB measure the *P*-wave velocity in a Cartesian coordinate system on section halves. The PWC measures the *P*-wave velocity vertically to the sectional plane of the working half (x-axis), whereas the PWB measures the cross-section (y-axis) and the long axis (z-axis) of the core.

All tools transmit a 500 kHz *P*-wave pulse through the core section at a specified repetition rate. This signal is coupled to the sample by the plastic pole pieces of the transducers and the pressure applied by the linear actuator. In contrast to the PWC and PWB, no water is used to improve coupling between the transducers of the PWL and the liner because the pressure applied by the actuator is known to be sufficient for reliable *P*-wave measurements. The transmitting and receiving ultrasonic transducers are aligned so that wave propagation is perpendicular to the section's long axis.

Traveltime is determined by signal processing software that automatically detects first arrival of the *P*-wave signal to a precision of 50 ns. It is a challenge for an automated routine to pick the first arrival of a potentially weak signal with significant background noise. The search method skips the first positive amplitude and finds the second positive amplitude using a detection threshold limit, typically set to 30%

of the maximum amplitude of the signal. It then finds the preceding zero crossing and subtracts one period to determine the first arrival. To avoid extremely weak signals, minimum signal strength can be set (typically 0.02 V) and weaker signals are ignored. To avoid cross-talk signals from the receiver at the beginning of the record, a delay (typically 0.01 ms) can be set to force the amplitude search to begin in the quiet interval preceding the first arrival. In addition, a trigger (typically 4 V) to initiate the arrival search process and the number of waveforms to be stacked (typically five) can also be set. A linear voltage differential transformer is used to measure the separation of the transducer to derive a travel path length for the signal (i.e., the slightly compressed core diameter). After corrections for system propagation delay, liner thickness, and liner material velocity, the ultrasonic *P*-wave velocity is calculated.

Natural gamma radiation

The NGRL measures gamma rays emitted from whole-round core sections. Gamma rays arise primarily as a result of the decay of uranium, thorium, and potassium isotopes. Data generated from this instrument are used to augment geologic interpretations and fine tune stratigraphic correlations. NGR logging is also quite useful as representing the same parameter, which could also be measured in downhole logs.

The main NGR detector unit consists of 8 NaI scintillator detectors, 7 plastic scintillator detectors, 22 photomultipliers, and passive lead shielding. The NaI detectors are covered by at least 8 cm of lead shielding. In addition, lead separators (~7 cm of low-background lead) are positioned between the NaI detectors. The inner half of the lead shielding closest to the NaI detectors is composed of low-background lead, whereas the outer half is composed of regular (virgin) lead. In addition to this passive lead shielding, the NGR employs a plastic scintillator to suppress the high-energy gamma (γ) and muon (μ) components of cosmic radiation by producing a veto signal when charged particles from cosmic radiation pass through the plastic scintillator.

A measurement run consists of two positions on each core section counted for at least 5 min each (10 min for Site U1357 cores) for a total of 16 measurements per section. Complete spectra for each measurement are uploaded to LIMS. Background measurement measures the signal generated when an acrylic liner containing a small amount of low-background lead is in the Ti boat inside the NGRL.

Moisture and density

Wet and dry bulk density, grain density, water content, and porosity were determined from measurements of wet sediment mass, dry sediment mass, and dry sediment volume. In soft sediments, ~10 cm^3 samples were extracted, usually from the middle of each core section, and placed in preweighed 16 mL Wheaton beakers. Stiff sediments were sampled, where appropriate, by extracting ~10 cm^3 blocks using a spatula and placed into a beaker as above. Indurated sediments were sampled by cut cubes that are ~2.5 cm in height, width, and depth. One sample was routinely collected in each undisturbed section where recovery was good and sedimentation rates were high.

Sample mass was determined to a precision of 0.01 g using two Mettler Toledo electronic balances and a computer averaging system to compensate for the ship's motion. Dry sample volumes were determined using a hexapycnometer system that consists of six custom-configured Micromeritics AccuPyc 1330TC helium-displacement pycnometers with a precision of 1% of the nominal full-scale volume. Volume measurements were preceded by three purges of the sample chambers with helium warmed to ~25°C. Three acquisition cycles were used for each sample. A reference volume was included within each sample set and rotated sequentially among the cells to check for instrument drift and systematic error. Sample beakers used for discrete determination of moisture and density were calibrated before the cruise. Dry mass and volume were measured after samples were heated in an oven at 105° ± 5°C for 24 h and allowed to cool in a desiccator. Procedures for the determination of these properties comply with the American Society for Testing and Materials (ASTM) designation (D) 2216 (ASTM International, 1990). Fundamental phase relationships and assumptions for the calculations of all physical property parameters are discussed by Blum (1997) and summarized in **"Mass and volume calculation"** and **"Calculation of bulk properties."**

Mass and volume calculation

Method C, sediments and hard rock

Wet mass (M_{wet}), dry mass (M_{dry}), and dry volume (V_{dry}) are measured in the laboratory. The mass ratio (r_m) is a computational constant of 0.965 (i.e., 0.965 g of freshwater per 1 g of seawater). Salt precipitated in sediment pores during the drying process is included in the M_{dry} and V_{dry} values. The mass of the evaporated water (M_{water}) and the salt (M_{salt}) in the sample are given by

$$M_{\mathrm{water}} = M_{\mathrm{wet}} - M_{\mathrm{dry}}$$

and

$$M_{\mathrm{salt}} = M_{\mathrm{water}}\,[s/(1-s)],$$

where s is the assumed saltwater salinity (0.035) corresponding to a pore water density (ρ_{pw}) of 1.024 g/cm^3 (from experimental and empirical relations between salinity and density at laboratory conditions; Blum 1997) and a salt density (ρ_{salt}) of 2.22 g/cm^3. The corrected mass of pore water (M_{pw}), volume of pore water (V_{pw}), mass of solids excluding salt (M_{solid}), mass of salt (M_{salt}), volume of salt (V_{salt}), wet volume (V_{wet}), and volume of solids excluding salt (V_{solid}) are, respectively,

$$M_{pw} = (M_{wet} - M_{dry})/r_m,$$

$$V_{pw} = M_{pw}/\rho_{pw},$$

$$M_{solid} = M_{wet} - M_{pw},$$

$$M_{salt} = M_{pw} - (M_{wet} - M_{dry}),$$

$$V_{salt} = M_{salt}/\rho_{salt},$$

$$V_{wet} = V_{dry} - V_{salt} + V_{pw},$$

and

$$V_{solid} = V_{wet} - V_{pw}.$$

Method D, hard rock and measured volume of soft sediment

Wet (or total) volume (V_t), dry mass (M_{dry}), and dry volume (V_{dry}) are measured in the laboratory. The total mass including the fresh water that was in the pores is calculated using (density of water of 1 g/cm^3) by

$$M_t = M_{dry} + (V_t - V_{dry}) \times \rho_w.$$

Assuming a pore water density of 1.024, the volume of the pore water is calculated by

$$V_{pw} = (V_t - V_{dry})/\rho_{pw}.$$

Finally, the mass of the pore water is

$$M_{pw} = V_{pw} \times \rho_{pw}.$$

Calculation of bulk properties

For all sediment samples, water content (w) is expressed as the ratio of the mass of pore water to the wet sediment (total) mass:

$$w = M_{pw}/M_{wet}.$$

Wet bulk density (ρ_{wet}), dry bulk density (ρ_{dry}), sediment grain density (ρ_{solid}), porosity (ϕ), and void ratio (VR) are calculated from

$$\rho_{wet} = M_{wet}/V_{wet},$$

$$\rho_{dry} = M_{solid}/V_{wet},$$

$$\rho_{solid} = M_{solid}/V_{solid},$$

$$\phi = V_{pw}/V_{wet} \times 100,$$

and

$$VR = V_{pw}/V_{solid}.$$

Thermal conductivity

Thermal conductivity is the measure of a material's ability to transmit heat by molecular conduction. Thermal conductivity and temperature measurements of sediments and rock sections are used to determine heat flow. Heat flow is not only characteristic of the material but is also an indicator of type and age of ocean crust and fluid circulation processes at shallow and great depths. Thermal conductivity was measured on one section of unsplit soft-sediment core (usually at 75 cm) using the TK04 measurement system (see Blum, 1997), which employs the transient linear heat source method in full-space configuration (Von Herzen and Maxwell, 1959), after the core equilibrated to ambient temperature. The full-space needle, containing a heater wire and calibrated thermistor, was inserted into the sediment through a small hole drilled into the core liner. The TK04 system uses an automated routine to find the conductivity by least-squares fitting to the measured temperature time series. No calibration was required for this system because each probe is calibrated prior to leaving the factory. However, Macor standard samples are provided to assure quality of the needles regularly. Measurements were taken after the core temperature was equilibrated to laboratory temperature. Special care was taken to minimize measurement drift by covering the needle point of entry and insulating it from external temperature shifts. Measurement errors are 5%–10%.

Stratigraphic correlation and composite section

When coring multiple holes at Sites U1357, U1359, and U1361, stratigraphic correlation was carried out onboard to correlate adjacent holes using Correlator software (version 1.68). This software allows for the depth adjustment of individual or multiple cores to enable correlations to be made between cores in separate holes based on the patterns of shipboard core logging data.

Depth adjustment of individual cores is often necessary for a variety of reasons, including gaps between two adjacent cores, incomplete recovery, and differences in seafloor topography between holes or inconsistent mudline definition. Genuine stratigraphic inconsistencies also may occur between holes because of slight differences in sedimentation rates and erosion histories. Further complication of the correlation procedure may stem from a lack of unambiguous tie points between holes. Ambiguities may arise caused by genuine inconsistencies in the physical properties of contemporaneous strata, inaccuracies/imprecision of the physical property data, and drilling disturbances that affect the quality of the data.

Possession of two or more overlapping records from adjacent holes provides an opportunity for the construction of a spliced stratigraphic record against a common composite core depth below seafloor (CCSF; see below and Table T1). This spliced record has the potential to optimize both the completeness of the site's stratigraphic record and the reliability of the associated stratigraphic data. For Sites U1357, U1359, and U1361 drilled during Expedition 318, the key physical property data that were utilized to aid correlation were NGR, magnetic susceptibility, and GRA bulk density. The recovery of a complete sediment section of APC-cored intervals was crucial to the paleoceanographic objectives of Sites U1357, U1359, and U1361. Drilling of parallel holes at these sites was planned to ensure that intervals missing from one APC hole as a result of recovery gaps between cores could be recovered in an adjacent hole. A composite depth section has been developed for these multiply cored sites to confirm continuity of recovery.

Adjustments to the shipboard core depth below seafloor, method A (CSF-A; see below and Table T1), depth scale are required for several reasons (e.g., Ruddiman et al., 1987; Hagelberg et al., 1992). Elastic rebound and gas expansion of the sediment following core recovery causes the cored sediment sequence to be expanded relative to the cored interval. As a result, the composite depth scale increases downhole relative to the CSF-A scale, typically on the order of 10%. In addition, the ship's motion, which is affected by tides and heave, can influence the in situ depth at which a core is cut. Portions of the sediment sequence are usually missing, even between cores that have >100% recovery.

A composite depth scale places coeval, laterally continuous stratigraphic features into a common frame of reference by shifting the CSF-A depth scales of individual cores to maximize the correlation between holes. The individual cores are shifted vertically without permitting expansion or contraction of the relative depth scale within any individual core. A horizontal feature recovered from several adjacent holes will have approximately the same core composite depth below seafloor, appended (CCSF-A), which is equivalent to the ODP meters composite depth scale. However, it will most likely have a different CSF-A scale, which is equivalent to the ODP meters below seafloor depth scale. Horizontal features will have exactly the same CCSF-A in two holes at the correlation tie points. Most other intervals cannot be precisely correlated (offsets of a few millimeters to several centimeters) because of differential stretching and squeezing within cores. APC recovery gaps between cores in one hole are typically from 0.5 to 2 m and rarely exceed 5 m. After establishing a CCSF-A scale, a complete stratigraphic record is spliced from the data of the multiple holes.

The methods used during Expedition 318 to construct composite depth and spliced sections were similar to those used during ODP Leg 138 (Hagelberg et al., 1992) and numerous subsequent paleoceanographic ODP legs and IODP expeditions. For each site, the hole to hole correlation was based on 2.5 or 5 cm spaced physical property data (see **"Physical properties"**).

Correlations were carried out visually by selecting a tie point from primarily the WRMSL data in one hole and comparing it directly with the same point measured from the length of the drill string advance, on a core by core basis. The core that has the most pristine record of the upper portion of the upper few meters of the sedimentary record, particularly the mudline, was chosen as the first (anchor) point of the composite section. The CCSF-A of the first core is thus the same as its CSF-A depth. A tie point that gave the preferred correlation was selected between data from this core and a core in an adjacent hole. All data from the second hole below the correlation point were vertically shifted to align the tie points horizontally between the holes. Once the depth adjustment was made, the shifted section became the reference section and a tie was made to a core from another hole. The process continued downhole, vertically shifting the data from one core at a time relative to data from the other hole. The tie points were added to the "affine" table, which records all of the depth adjustments ("offsets") that define the composite depth scale in CCSF-A. The composite depth scale is presented in tabular form in the "Stratigraphic correlation and composite depth" section of the chapters for the multiply cored sites (see the **"Site U1357," "Site U1359,"** and **"Site U1361"** chapters). For each core, the depth adjustment required to convert from the CSF-A scale to the CCSF-A scale is given as the cumulative depth offset added to the IODP curatorial subbottom depth (in CSF-A).

During the composite section construction procedure, a spliced record was assembled that provides a single representative sedimentary record suited for postcruise sampling and studies. Splice ties were established as close to the composite depth tie points as the Correlator program allowed. Intervals were chosen for the splice so that section continuity was maintained and disturbed intervals were avoided. Further adjustments to the composite depth section by detailed correlation that includes expanding and compressing the depth scale within individual core intervals are required to align all features exactly.

This practice ensures that missing sedimentary sections from most intercore gaps within a given hole are recovered in one or more adjacent holes. At least two complete holes and a third partial hole are usually necessary to recover a complete section in the APC portion of a site. Additional complete holes are cored to allow options for construction of alternate splices, where possible.

Our goals for stratigraphic correlation, in priority order are

- To guide drilling to ensure recovery of a complete stratigraphic section,
- To establish a composite depth scale,
- To define a stratigraphically complete and representative sampling splice (and if possible one or more alternate splices), and
- To evaluate and (if possible) refine shipboard stratigraphic age models by synthesizing all available age information, including the potential for tuning of lithologic variations to reference records.

As a result of this stratigraphic correlation process, several different depth models are created. The following section provides detailed discussion of the definitions of these depth scales and the process by which they were created (see also **"Core recovery and depths"** and Table T1).

Depth scales

Core depth below seafloor, method A

Initial depths for the top and bottom of each core are assigned during drilling, based on the length of the drill string below the ship's drilling rig floor and the length of recovered sediment. In IODP this is referred to as CSF-A, which is equivalent to the ODP meters below seafloor depth scale. The zero point on the CSF-A scale is defined by the mudline in the first core of each hole. It is often difficult to tell whether this empirical mudline recovered the true sediment/water interface. Some holes are started from below the sediment water interface. In this case the zero depth point in CSF-A units may be substantially offset from the zero depth point in adjacent holes that recovered the sediment/water interface.

Within each core, CSF-A depths are calculated based on the drilling depth to the top of the core, and by adding the depth offset of each data point within a section to the sum of the overlying sections. "Created lengths," which are the lengths of the core liner sections measured with a ruler on the core-receiving platform ("catwalk"), are used for calculating CSF-A depths. Errors between sections because of the use of created lengths to determine depth in a given core may be as much as several centimeters, especially lower in each core where the sum of several section created lengths is used for the depth calculation. In spite of these potential errors, the use of created lengths provides for consistency in the database (i.e., the depths are precise, even if not completely accurate).

The CSF-A scale is also inaccurate because of ship heave (which is not compensated for in APC coring), tidal variations in sea level, and other sources of error.

Core composite depth scale, appended

Before a splice can be constructed, the cores from the various holes must be stratigraphically correlated with each other. Such correlation transfers initial estimates of depths of drilling (CSF-A) into a composite depth scale referred to as CCSF-A. This IODP depth scale is approximately equivalent to the ODP meters composite depth scale.

At each site, the first selected core becomes the "anchor point" in the composite depth scale for all the holes and is usually the only core in which depths are the same on both the CSF-A and CCSF-A scales. From this anchor, core-logging data are correlated among holes downsection. An affine value specific to each core is added to the CSF-A in sequence down the holes.

It is not possible to align all features perfectly between holes, so where possible the affine values are chosen to maximize correlations at the levels that splice tie points are defined between holes (see below).

Composite depth scale construction

The raw stratigraphic data were imported into the shipboard Correlator software program. Input data for this program were downloaded from the ship's database (LIMS) using the Web-based LIMS to Correlator tool, but we also directly uploaded comma-delimited Microsoft Excel files. Upload of the resulting depth models to LIMS was attempted with the AffineSpliceUploader program.

Correlator enables the graphical construction of a composite depth scale for each hole at a given site by depth-shifting individual cores to maximize the correlation of core logging data among multiple holes. For hole to hole correlations and for plotting results, data were filtered to avoid incorporating anomalous data influenced by edge effects at section boundaries or core tops or in voids where no sediment was present; however, all original data were retained in LIMS.

Depth intervals within cores are not squeezed or stretched by Correlator; therefore, it is not possible to align all the correlative features within each core. Stretching or squeezing between cores from different holes may reflect small-scale differences in sedimentation and/or distortion caused by the coring and archiving processes. For example, the tops of APC cores are often stretched and the bottoms compressed, although this depends on lithology and extent of lithification.

Correlations among cores from adjacent holes are evaluated visually and statistically (by cross-correlation). The depth offsets for each core that are necessary to convert CSF-A to CCSF-A are recorded in an affine table for each site. The CCSF-A for any point within a core equals the CSF-A plus the affine offset. Correlation at finer resolution is not possible with Correlator because depth adjustments are applied linearly to individual cores; at this stage of depth scale development, no adjustments in the length of each core, such as numerically squeezing and stretching, are made within cores. Such finer scale adjustment of individual cores relative to the splice (e.g., Hagelberg et al., 1995; Pälike et al., 2005) or relative to logging data (e.g., Harris et al., 1995) can be done following the development of the composite section.

The length of the CCSF-A scale at a given site is typically ~10% greater than the length of the cored section in any one hole, as indicated by the CSF-A scale. Although the exact reasons for this apparent expansion of the sediment column are unknown, it is commonly attributed to rebound following release of overburden in the deeper sections, stretching during the coring process, gas expansion during the core recovery process, and other factors (Moran, 1997).

Splice

The splice is a composite core section representing the best available representation of a complete stratigraphic column at a site. It is composed of core sections from adjacent holes such that coring gaps in one hole are filled with core from an adjacent hole. The objective of the splice is to fill coring gaps and an effort has been made to minimize inclusion of disturbed sections by using the core disturbance classification made by the sedimentologists. The shipboard splice is ideally suited to guide core sampling for detailed paleoceanographic studies. A splice table and figure are presented in the site chapters that summarize the tie points between intervals from each hole used to construct the splice. The portion of the CCSF-A scale that is applied to the splice is referred to as core composite depth below seafloor, method D (CCSF-D). Within the splice sections, CCSF-D is identical to CCSF-A.

The choice of splice tie points is somewhat subjective. The method used in the construction of a splice followed three rules. First, where possible we avoided using the top and bottom 50 cm of cores, where disturbance caused by drilling artifacts (even if not apparent in core logging data) was most likely. We also avoided reassembled first sections of cores that were severely disturbed unless it was the only representation of a sedimentary interval. Second, we attempted to incorporate those realizations of the stratigraphic section that in our judgment were most representative of the holes recovered. Third, we tried to minimize tie points (i.e., to use the longest possible sections within individual cores) in order to simplify sampling.

Where possible, additional shipboard splices may be constructed, so that more than one copy of a complete stratigraphic section is available for high-resolution sampling. Where this is done, multiple splices would all have depth scales designated as CCSF-D. Therefore, the final composite depth scale, CCSF-D, is only formally defined in the primary shipboard splice. Composite depth scales for any alternate splices are also assigned CCSF-D scales, but this scale is slightly different than CCSF-D in the primary splice. To avoid confusion, alternative splices can be designated numerically, CCSF-D2, D3, and so on, depending on the number of additional splices. A solution to the problem of comparing different splices is to create an additional depth scale that numerically stretches and squeezes features into a splice-correlated scale (core composite depth below seafloor, method C). Such scales are applied to individual holes and thus may be discontinuous. In ODP, such a scale was referred to as "revised meters composite depth." During Expedition 318, we did not create splice-correlated scales because of software limitations.

Downhole logging

Downhole logs are used to determine physical, chemical, and structural properties of the formation penetrated by a borehole. The data are rapidly collected, continuous with depth, and measured in situ; they can be interpreted in terms of the stratigraphy, lithology, mineralogy, and geochemical composition of the penetrated formation. Where core recovery is incomplete or disturbed, log data may provide the only way to characterize the borehole section.

Where core recovery is good, log and core data complement one another and may be interpreted jointly.

Downhole logs measure formation properties on a scale that is intermediate between those obtained from laboratory measurements on core samples and geophysical surveys. They are useful in calibrating the interpretation of geophysical survey data (e.g., through the use of synthetic seismograms) and provide a necessary link for the integrated understanding of physical properties on all scales.

Wireline logging

During wireline logging operations, the logs are recorded with a variety of Schlumberger logging tools combined into several tool strings, which are lowered into the hole after completion of coring operations. Three tool strings were used during Expedition 318: the triple combination (triple combo; (gamma radiation, porosity, density, and resistivity), the Formation MicroSanner (FMS)-sonic (FMS resistivity image of the borehole wall and sonic velocities), and the Versatile Seismic Imager (VSI; seismic check shots) (Fig. F20; Table T6). Each tool string also contains a telemetry cartridge for communicating through the wireline to the Schlumberger data acquisition system (MAXIS unit) on the drillship.

In preparation for logging, the boreholes were flushed of debris by circulating viscous drilling fluid and filled with a seawater-based logging gel (sepiolite mud mixed with seawater and weighted with barite; approximate density = 10.5 lb/gal) to help stabilize the borehole walls. The BHA was pulled up to ~100 m WSF to cover the unstable upper part of the hole. The tool strings were then lowered downhole on a seven-conductor wireline cable before being pulled up at constant speed, typically 250–550 m/h, to provide continuous measurements of several properties simultaneously. A wireline heave compensator (WHC) was used when necessary to minimize the effect of ship's heave on the tool position in the borehole (see below). During each logging run, incoming data were recorded and monitored in real time on the MCM MAXIS logging computer.

Logged sediment properties and tool measurement principles

The logged properties, and the principles used in the tools to measure them, are briefly described below. The main logs are listed in Table T7. More detailed information on individual tools and their geological applications may be found in Serra (1984, 1986, 1989), Schlumberger (1989, 1994), Rider (1996), Goldberg (1997), Lovell et al. (1998), and Ellis and Singer (2007). A complete online list of acronyms for the Schlumberger tools and measurement curves is at **www.slb.com/modules/mnemonics/index.aspx.**

Natural radioactivity

The Hostile Environment Natural Gamma Ray Sonde was used on the triple combo and FMS-sonic tool strings to measure and classify natural radioactivity in the formation. It uses two bismuth germanate scintillation detectors and five-window spectroscopy to determine concentrations of K, Th, and U. The radioactive isotopes of these three elements dominate the natural radiation spectrum.

The Scintillation Gamma Ray Tool (SGT) uses a sodium iodide scintillation detector to measure the total natural gamma ray emission, combining the spectral contributions of potassium, thorium, and uranium concentrations in the formation. The SGT is not a spectral tool but provides high-resolution total gamma ray measurements.

The inclusion of a gamma ray sonde in every tool string allows use of the gamma ray data for depth correlation between logging strings and passes.

Density

Formation density was measured with the Hostile Environment Litho-Density Sonde (HLDS). The sonde contains a radioactive cesium (^{137}Cs) gamma ray source (622 keV) and far and near gamma ray detectors mounted on a shielded skid, which is pressed against the borehole wall by a hydraulically activated eccentralizing arm. Gamma rays emitted by the source undergo Compton scattering, in which gamma rays are scattered by electrons in the formation. The number of scattered gamma rays that reach the detectors is proportional to the density of electrons in the formation, which is in turn related to bulk density. Porosity may also be derived from this bulk density if the matrix (grain) density is known. Good contact between the tool and borehole wall is essential for good HLDS logs; poor contact results in underestimation of density values.

The HLDS also measures photoelectric absorption as the photoelectric effect (PEF). Photoelectric absorption of the gamma rays occurs when their energy is reduced below 150 keV after being repeatedly scattered by electrons in the formation. Because PEF depends on the atomic number of the elements in the formation, it also varies according to the chemical composition of the minerals present and can be used for the identification of some minerals. For example, the PEF of calcite = 5.08 barns per electron (b/e$^-$), illite = 3.03 b/e$^-$, quartz = 1.81 b/e$^-$, and kaolinite = 1.49 b/e$^-$.

Porosity

Formation porosity was measured with the Accelerator Porosity Sonde. The sonde includes a minitron neutron generator that produces fast (14.4 MeV) neutrons and five neutron detectors (four epithermal and one thermal) positioned at different spacings from the minitron. The tool's detectors count neutrons that arrive at the detectors after being scattered and slowed by collisions with atomic nuclei in the formation.

The highest energy loss occurs when neutrons collide with hydrogen nuclei, which have practically the same mass as the neutron (the neutrons bounce off of heavier elements without losing much energy). If the hydrogen (i.e., water) concentration is low, as in low-porosity formations, neutrons can travel farther before being captured, and the count rates increase at the detector. The opposite effect occurs in high-porosity formations where the water content is high. However, because hydrogen bound in minerals such as clays or in hydrocarbons also contributes to the measurement, the raw porosity value is often an overestimate.

Upon reaching thermal energies (0.025 eV), the neutrons are captured by the nuclei of Cl, Si, B, and other elements, resulting in a gamma ray emission. This neutron capture cross section (Σ_f) is also measured by the tool.

Electrical resistivity

The phasor dual induction/spherically focused resistivity tool (DIT) was used to measure electrical resistivity. The DIT provides three measures of electrical resistivity, each with a different depth of investigation into the formation. The two induction devices (deep and medium depths of penetration) transmit high-frequency alternating currents through transmitter coils, creating magnetic fields that induce secondary currents in the formation. These currents produce a new inductive signal, proportional to the conductivity of the formation, which is measured by the receiving coils. The measured conductivities are then converted to resistivity (in ohm-meters). The spherically focused resistivity is measured by an electrode device that sends a current into the formation while trying to maintain a constant voltage drop. The amount of current necessary to keep the voltage gives a direct measure of resistivity. This device uses several electrodes to focus the current flow into the formation so that equipotential surfaces are spherical and has a higher vertical resolution than the induction measurements. Calcite, silica, and hydrocarbons are electrical insulators, whereas ionic solutions like pore water are conductors. Electrical resistivity, therefore, can be used to evaluate porosity for a given salinity and resistivity of the pore water.

Acoustic velocity

The Dipole Sonic Imager measures the transit times between sonic transmitters and an array of eight receivers. It combines replicate measurements, thus providing a measurement of compressional velocity through sediments that is relatively free from the effects of formation damage and of an enlarged borehole (Schlumberger, 1989). Along with the monopole transmitters found on most sonic tools, it also has two cross-dipole transmitters, which allow an additional measurement of shear wave velocity. Dipole measurements are necessary to measure shear velocities in slow formations, whose shear velocity is less than the velocity of sound in the borehole fluid. Such slow formations are typically encountered in deep ocean drilling.

Formation MicroScanner

The FMS provides high-resolution electrical resistivity images of borehole walls. The tool has four orthogonal arms and pads, each containing 16 button electrodes that are pressed against the borehole wall during the recording. The electrodes are arranged in two diagonally offset rows of eight electrodes each. A focused current is emitted from the button electrodes into the formation, with a return electrode near the top of the tool. Resistivity of the formation at the button electrodes is derived from the intensity of current passing through the button electrodes. Processing transforms these measurements into oriented high-resolution images that reveal the geologic structures of the borehole wall. Features such as bedding, stratification, fracturing, slump folding, and bioturbation can be resolved; the images are oriented to magnetic north, so that fabric analysis can be carried out and the dip and direction (azimuth) of planar features in the formation can be measured.

The maximum extension of the FMS caliper arms is 15 inches. In holes with a diameter larger than 15 inches, the pad contact will be inconsistent and the FMS images may appear out of focus and too conductive. Irregular borehole walls will also adversely affect the images if contact with the wall is poor.

Accelerometry and magnetic field measurement

Three-component acceleration and magnetic field measurements were made with the General Purpose Inclinometry Tool (GPIT). The primary purpose of this tool, which incorporates a three-component accelerometer and a three-component magnetometer, is to determine the acceleration and orientation of the FMS-sonic tool string during logging. Thus, the FMS images can be corrected for irregular tool motion, and the dip and direction (azimuth) of features in the FMS image can be determined. During Expedition 318, it was also used to record the downhole tool motion and evaluate in real time the performance of the new WHC.

Vertical seismic profile

In a vertical seismic profile (VSP) experiment, a borehole seismic tool is anchored against the borehole wall at regularly spaced intervals and records the full waveform of elastic waves generated by a seismic source positioned just below the sea surface. These "check shot" measurements relate depth in the hole to traveltime in reflection seismic lines. The VSI used here contains a three-axis geophone. In the planned VSP/check shots, the VSI was to be anchored against the borehole wall at 25 m station intervals, with 5–10 air gun shots typically taken at each station. The recorded waveforms were stacked and a one-way traveltime was determined from the median of the first breaks for each station. The seismic source used was a Sercel G. Gun Parallel Cluster, composed of two 250 in^3 air guns separated by 1 m. It was positioned on the port side of the *JOIDES Resolution* at a water depth of ~7 mbsl with a borehole offset of ~30 m. The VSI was deployed in Hole U1359D, but the caliper arm failed to open and the geophone could not be clamped against the borehole wall. However, one valid check shot one-way time was obtained with the tool resting on the bottom of the hole.

Precautions were taken to protect marine mammals. If there were no mammals in or approaching the safety radius (940 m for water depths >1000 mbsl, 1410 m for water depths between 100 and 1000 mbsl), air gun operations commenced using a ramp-up, or "soft start" procedure (gradually increasing the operational pressure and air gun firing interval) to provide time for undetected animals to respond to the sounds and vacate the area. Once the air guns were at full power, the check shot survey proceeded. Marine mammal observations continued during the check shot survey, and if a mammal entered the safety radius, the survey was suspended.

Log data quality

The principal influence on log data quality is the condition of the borehole wall. Where the borehole diameter varies over short intervals because of washouts or ledges made of layers of harder material, the logs from tools that require good contact with the borehole wall (i.e., the FMS and density tools) may be degraded. Deep investigation measurements such as gamma ray, resistivity, and sonic velocity, which do not require contact with the borehole wall, are generally less sensitive to borehole conditions. Very narrow ("bridged") sections will also cause irregular log results. The quality of the borehole is improved by minimizing the circulation of drilling fluid while drilling, flushing the borehole to remove debris, and logging as soon as possible after drilling and conditioning are completed.

The quality of the logging depth determination depends on several factors. The depth of the logging measurements is determined from the length of the cable played out from the winch on the ship. The seafloor (mudline) is identified on the natural gamma ray log by the abrupt reduction in gamma ray count at the water/sediment boundary. Discrepancies between the drillers depth and the wireline log depth occur because of core expansion, incomplete core recovery, or incomplete heave compensation for the drillers depth. In the case of log depth, discrepancies between successive runs occur because of incomplete heave compensation, incomplete correction for cable stretch, and cable slip. In the case of very fine sediments in suspension, the mudline can be an elusive datum. Tidal changes in sea level will also have an effect. To minimize the wireline tool motion caused by ship heave, a new hydraulic WHC was used to adjust the wireline length for rig motion during wireline logging operations.

Wireline heave compensator

Expedition 318 continued evaluation of the new WHC system. Such WHC systems are designed to compensate for the vertical motion of the ship and maintain a steady motion of the logging tools (Goldberg, 1990). The new WHC uses vertical acceleration measurements made by a motion reference unit (MRU), located under the rig floor near the center of gravity of the ship, to calculate the vertical motion of the ship. It then adjusts the length of the wireline by varying the distance between two sets of pulleys through which the cable passes. Real-time measurements of uphole (surface) and downhole acceleration are made simultaneously by the MRU and by the GPIT, respectively. A Lamont-developed software package allows these data to be analyzed and compared in real time, displaying the actual motion of the logging tool string, and enabling evaluation of the efficiency of the compensator. In addition to an improved design and smaller footprint compared to the previous system, location of the WHC with the winch unit on the starboard side of the derrick contributes to a significant reduction in the time necessary to prepare for logging operations.

Logging data flow and log depth scales

Data for each wireline logging run were monitored in real time and recorded using the Schlumberger MAXIS 500 system. The depths of the initial logging data are referenced to the rig floor [WRF]). After logging was completed, the data were shifted to a seafloor reference (WSF), based on the step in gamma radiation at the water/sediment interface. These data were made available to the science party.

The downhole log data were also transferred onshore to Lamont-Doherty Earth Observatory for standardized data processing. The main part of the processing is depth matching to remove depth offsets between different logging runs, which results in a new depth scale, wireline matched depth below seafloor. Also, corrections are made to certain tools and logs, documentation for the logs (with an assessment of log quality) is prepared, and the data are converted to ASCII format for the conventional logs and GIF for the FMS images. Schlumberger GeoQuest's GeoFrame software package is used for most of the processing. The data were transferred back to the ship within a few days of logging and made available (in ASCII and DLIS formats) through the shipboard IODP logging database.

Core-log-seismic integration

A depth-traveltime relationship must be determined at each site to correlate core and log data acquired in depth with seismic reflection measurements that are a function of traveltime. A direct measurement of the depth-traveltime relationship is given by the first arrival times in the zero-offset VSP (see above).

It can also be estimated by constructing synthetic seismograms, which are computed from reflection coefficients resulting from downhole contrasts in P-wave velocity and density, to match the seismic traces closest to the borehole. When the quality of the shipboard sonic logs was sufficient, synthetic seismograms were calculated from the density and V_P logs using the IESX seismic interpretation package (part of the Schlumberger GeoFrame software suite), which allows for interactively adjusting the depth-traveltime relationship until a good match is achieved between features in the synthetic seismogram and in the measured seismic data. A calibrated depth-traveltime relationship allows for correlation of the borehole stratigraphy with seismic reflection features (e.g., to assign ages to prominent seismic reflectors that can then be correlated away from the drill site).

In situ temperature measurements

In situ temperature measurements were made with the advanced piston corer temperature tool (APCT-3) on cores from Site U1359. The APCT-3 fits directly into the coring shoe of the APC and consists of a battery pack, data logger, and a platinum resistance-temperature device calibrated over a temperature range from 0° to 30°C. Before entering the borehole, the tool was first stopped at the mudline for 5 min to thermally equilibrate with bottom water and give a bottom water temperature. After the APC penetrated the sediment, it was held in place for 10 min as the APCT-3 recorded the temperature of the cutting shoe every second. When the APC is plunged into the formation, there is an instantaneous temperature rise from frictional heating. This heat gradually dissipates into the surrounding sediments as the temperature at the APCT-3 equilibrates toward the temperature of the sediments.

The equilibrium temperature of the sediments was estimated by applying a mathematical heat-conduction model to the temperature decay record (Horai and Von Herzen, 1985). The synthetic thermal decay curve for the APCT-3 tool is a function of the geometry and thermal properties of the probe and the sediments (Bullard, 1954; Horai and Von Herzen, 1985). The equilibrium temperature must be estimated by applying a fitting procedure (Pribnow et al., 2000). However, where the APC has not achieved a full stroke, or where ship heave pulls the APC up from full penetration, the temperature equilibration curve will be disturbed and temperature determination is more difficult. The nominal accuracy of the APCT-3 measurements is ±0.05°C.

The APCT-3 data were combined with measurements of thermal conductivity (see "Physical properties") obtained from whole-core samples to obtain heat flow values. Heat flow was calculated according to the Bullard method, to be consistent with the synthesis of ODP heat flow data by Pribnow et al. (2000).

References

Abelmann, A., 1992. Early to middle Miocene radiolarian stratigraphy of the Kerguelen Plateau, Leg 120. *In* Wise, S.W., Jr., Schlich, R., et al., *Proc. ODP, Sci. Results,* 120: College Station, TX (Ocean Drilling Program), 757–783. **doi:10.2973/odp.proc.sr.120.165.1992**

ASTM International, 1990. Standard method for laboratory determination of water (moisture) content of soil and rock (Standard D2216–90). In *Annual Book of ASTM Standards for Soil and Rock* (Vol. 04.08): Philadelphia (Am. Soc. Testing Mater.). [revision of D2216-63, D2216-80]

Bann, K.L., Fielding, C.R., MacEachern, J.A., and Tye, S.C., 2008. Sedimentology and ichnology of mixed wave- and storm-dominated deltaic deposits: examples from the Permian of Australia. *In* Hampson, G.J., Dalrymple, R., and Burgess, P. (Eds.), *Advances in Shelf and Shoreline Stratigraphy.* Spec Publ.—SEPM (Soc. Sediment. Geol.).

Below, R., 1981. Dinoflagellaten-Zysten aus dem oberen Hauterive bisunteren Cenoman Südwest-Marokkos. *Palaeontographica, Abt. B,* 176:1–145.

Berggren, W.A., 1992a. Neogene planktonic foraminifer magnetobiostratigraphy of the southern Kerguelen Plateau (Sites 747, 748, and 751). *In* Wise, S.W., Jr., Schlich, R., et al., *Proc. ODP, Sci. Results,* 120: College Station, TX (Ocean Drilling Program), 631–647. **doi:10.2973.odp.proc.sr.120.153.1992**

Berggren, W.A., 1992b. Paleogene planktonic foraminifer magnetobiostratigraphy of the southern Kerguelen Plateau (Sites 747–749). *In* Wise, S.W., Jr., Schlich, R., et al., *Proc. ODP, Sci. Results,* 120: College Station, TX (Ocean Drilling Program), 551–568. **doi:10.2973.odp.proc.sr.120.151.1992**

Berggren, W.A., Kent, D.V., Swisher, C.C., III, and Aubry, M.-P., 1995. A revised Cenozoic geochronology and chronostratigraphy. *In* Berggren, W.A., Kent, D.V., Aubry, M.-P., and Hardenbol, J. (Eds.), *Geochronology, Time Scales and Global Stratigraphic Correlation.* Spec. Publ.—SEPM (Soc. Sediment. Geol.), 54:129–212.

Bijl, P.K., Pross, J., Stickley, C.E., Huber, M., Guerstein, R., Houben, A.J.P., Warnaar, J., Sluijs, A., Visscher, H., and Brinkhuis, H., in press. Environmental forcing on Paleogene Southern Ocean biogeography, *Paleoceanography.*

Blum, P., 1997. Physical properties handbook: a guide to the shipboard measurement of physical properties of deep-sea cores. *ODP Tech. Note,* 26. **doi:10.2973/odp.tn.26.1997**

Bohaty, S.M., and Harwood, D.M., 2000. Ebridian and silicoflagellate biostratigraphy from Miocene and Eocene McMurdo erratics and the Southern Ocean. *In* Stillwell, J.D., and Feldmann, R.M. (Eds.), *Paleobiology and Paleoenvironments of Eocene Rocks, McMurdo Sound, East Antarctica.* Antarct. Res. Ser., 76:99–159.

Bown, P.R. (Ed.), 1998. *Calcareous Nannofossil Biostratigraphy:* Dordrecht, The Netherlands (Kluwer Academic Publ.).

Brinkhuis, H., and Biffi, U., 1993. Dinoflagellate cyst stratigraphy of the Eocene/Oligocene transition in central Italy. *Mar. Micropaleontol.,* 22(1–2):131–183. **doi:10.1016/0377-8398(93)90007-K**

Brinkhuis, H., Bujak, J.P., Smit, J., Versteegh, G.J.M., and Visscher, H., 1998. Dinoflagellate-based sea surface temperature reconstructions across the Cretaceous-Tertiary boundary. *Palaeogeogr., Palaeoclimatol., Palaeoecol.,* 141(1–2):67–83. **doi:10.1016/S0031-0182(98)00004-2**

Brinkhuis, H., and Leereveld, H., 1988. Dinoflagellate cysts from the Cretaceous/Tertiary boundary sequence of El Kef, northwest Tunisia. *Rev. Palaeobot. Palynol.,* 56(1–2):5–19. **doi:10.1016/0034-6667(88)90071-1**

Brinkhuis, H., Munsterman, D.K., Sengers, S., Sluijs, A., Warnaar, J., and Williams, G.L., 2003a. Late Eocene–Quaternary dinoflagellate cysts from ODP Site 1168, off western Tasmania. *In* Exon, N.F., Kennett, J.P., and Malone, M.J., *Proc. ODP, Sci. Results,* 189: College Station, TX (Ocean Drilling Program), 1–36. **doi:10.2973/odp.proc.sr.189.105.2003**

Brinkhuis, H., Powell, A.J., and Zevenboom, D., 1992. High-resolution dinoflagellate cyst stratigraphy of the Oligocene/Miocene transition interval in Northwest and central Italy. *In* Head, M.J., and Wrenn, J.H. (Eds.), *Neogene and Quaternary Dinoflagellate Cysts and Acritarchs:* Salt Lake City (Publishers Press), 219–258.

Brinkhuis, H., Pross, J., Pearce, M.A., Head, M.J., and Schiøler, P., 2009. *Advanced Course in Jurassic-Cretaceous-Cenozoic Organic-Walled Dinoflagellate Cysts: Morphology, Paleoecology and Stratigraphy; Urbino, Italy, July 2009:* Utrecht, The Netherlands (Lab. Palaeobot. Palynol., Utrecht Univ.).

Brinkhuis, H., and Schiøler, P., 1996. Palynology of the Geulhemmerberg Cretaceous/Tertiary boundary section (Limburg, The Netherlands). *Geol. Mijnbouw,* 75:193–213.

Brinkhuis, H., Sengers, S., Sluijs, A., Warnaar, J., and Williams, G.L., 2003b. Latest Cretaceous–earliest Oligocene and Quaternary dinoflagellate cysts, ODP Site 1172, East Tasman Plateau. *In* Exon, N.F., Kennett, J.P., and Malone, M.J., *Proc. ODP, Sci. Res.,* 189: College Station, TX (Ocean Drilling Program), 1–36. **doi:10.2973/odp.proc.sr.189.106.2003**

Brinkhuis, H., and Zachariasse, W.J., 1988. Dinoflagellate cysts, sea level changes and planktonic foraminifers across the Cretaceous–Tertiary boundary at El Haria, northwest Tunisia. *Mar. Micropaleontol.,* 13(2):153–191. **doi:10.1016/0377-8398(88)90002-3**

Bujak, J.P., Downie, C., Eaton, G.L., and Williams, G.L., 1980. Dinoflagellate cysts and acritarchs from the Eocene of southern England. *Spec. Pap. Paleontol.,* 24.

Bujak, J., and Mudge, D., 1994. A high-resolution North Sea Eocene dinocyst zonation. *J. Geol. Soc. (London, U. K.),* 151(3):449–462. **doi:10.1144/gsjgs.151.3.0449**

Bullard, E.C., 1954. The flow of heat through the floor of the Atlantic Ocean. *Proc. R. Soc. London, Ser. A,* 222:408–429.

Cande, S.C., and Kent, D.V., 1995. Revised calibration of the geomagnetic polarity timescale for the Late Cretaceous and Cenozoic. *J. Geophys. Res., [Solid Earth],* 100(B4):6093–6095. **doi:10.1029/94JB03098**

Clowes, C.D., and Wilson, G.J., 2006. Some new species of *Corrudinium* Stover and Evitt, 1978 (Dinophyceae) from the Eocene of New Zealand. *N. Z. J. Geol. Geophys.,* 49(3):399–408.

Cody, R.D., Levy, R.H., Harwood, D.M., and Sadler, P.M., 2008. Thinking outside the zone: high-resolution quantitative diatom biochronology for the Antarctic Neogene. *Palaeogeogr., Palaeoclimatol., Palaeoecol.,* 260(1–2):92–121. **doi:10.1016/j.palaeo.2007.08.020**

Crouch, E.M., and Brinkhuis, H., 2005. Environmental change across the Paleocene–Eocene transition from eastern New Zealand: a marine palynological approach. *Mar. Micropalaeontol.,* 56(3–4):138–160. **doi:10.1016/j.marmicro.2005.05.002**

Davey, R.J., 1979. The stratigraphic distribution of dinocysts in the Portlandian (Latest Jurassic) to Barremian (Early Cretaceous) of northwest Europe. *AASP Contrib. Ser.,* 5B:48–81.

Davey, R.J., and Verdier, J.-P., 1971. An investigation of microplankton assemblages from the Albian of the Paris Basin. *Verh.—K. Ned. Akad. Wet., Afd. Natuurkd., Eerste Reeks,* 26:1–58.

Davey, R.J., and Verdier, J.P., 1973. An investigation of microplankton assemblages from latest Albian (Vraconian) sediments. *Rev. Esp. Micropaleontol.,* 5(2):173–212.

Davey, R.J., and Verdier, J.P., 1974. Dinoflagellate cysts from the Aptian type sections at Gargas and La Bédoule, France. *Palaeontology,* 17:623–653.

de Graciansky, P.-C., Hardenbol, J., Jacquin, T., and Vail, P.R. (Eds.), 1998. Mesozoic and Cenozoic Sequence Stratigraphy of European Basins. *Spec. Publ.—Soc. Econ. Paleontol. Mineral.,* 60.

De Schepper, S., and Head, M.J., 2008. Age calibration of dinoflagellate cyst and acritarch events in the Plio-Pleistocene of the eastern North Atlantic (DSDP Hole 610A). *Stratigraphy,* 5(2):137–161.

de Verteuil, L., and Norris, G., 1996. Miocene dinoflagellate stratigraphy and systematics of Maryland and Virginia. *Micropaleontology,* 42(Suppl.). **doi:10.2307/1485926**

Dickson, A.J., Beer, C.J., Dempsey, C., Maslin, M.A., Bendle, J.A., McClymont, E.L., and Pancost, R.D., 2009. Oceanic forcing of the marine isotope Stage 11 interglacial. *Nat. Geosci.,* 2(6):428–433. **doi:10.1038/ngeo527**

Duxbury, S., 1977. A palynostratigraphy of the Berriasian to Barremian of the Speeton Clay of Speeton, England. *Palaeontographica, Abt. B,* 160:17–67.

Duxbury, S., 1980. Barremian phytoplankton from Speeton, east Yorkshire. *Palaeontographica, Abt. B,* 173:107–146.

Duxbury, S., 1983. A study of dinoflagellate cysts and acritarchs from the lower Greensand (Aptian to lower Albian) of the Isle of Wight, southern England. *Palaeontographica, Abt. B,* 186:18–80.

Eldrett, J.S., Harding, I.C., Firth, J.V., and Roberts, A.P., 2004. Magnetostratigraphic calibration of Eocene–Oligocene dinoflagellate cyst biostratigraphy from the Norwegian–Greenland Sea. *Mar. Geol.,* 204(1–2):91–127. **doi:10.1016/S0025-3227(03)00357-8**

Ellis, D.V., and Singer, J.M., 2007. *Well Logging for Earth Scientists,* (2nd ed.): Dordrecht, The Netherlands (Springer).

Evans, H.B., 1965. GRAPE—a device for continuous determination of material density and porosity. *Trans. SPWLA Annu. Logging Symp.:* 6(2):B1–B25.

Fensome, R.A., Guerstein, G.R., and Williams, G.L., 2007. New insights on the Paleogene dinoflagellate cyst genera *Enneadocysta* and *Licracysta* gen. nov. based on material from offshore eastern Canada and southern Argentina. *Micropaleontology,* 52(5):385–410. **doi:10.2113/gsmicropal.52.5.385**

Fensome, R.A., and Williams, G.L., 2004. *The Lentin and Williams Index of Fossil Dinoflagellates*. AASP Contrib. Ser., 42.

Fensome, R.A., Williams, G.L., and MacRae, R.A., 2008. Late Cretaceous and Cenozoic fossil dinoflagellates and other palynomorphs from the Scotian margin, offshore eastern Canada. *J. Syst. Palaeontol.,* 7(1):1–79. **doi:10.1017/S1477201908002538**

Foucher, J.-C., 1979. Distribution stratigraphique des kystes de dinoflagellés et des acritarches dans le Crétacé supérieur du bassin de Paris et de l'Europe septentrionale. *Palaeontographica, Abt. B,* 169:78–105.

Gersonde, R., 1991. Taxonomy and morphostructure of late Neogene diatoms from Maud Rise (Antarctic Ocean). *Polarforschung,* 59(3):141–171.

Gieskes, J.M., Gamo, T., and Brumsack, H., 1991. Chemical methods for interstitial water analysis aboard *JOIDES Resolution. ODP Tech. Note,* 15. **doi:10.2973/odp.tn.15.1991**

Goldberg, D., 1990. Test performance of the Ocean Drilling Program wireline heave motion compensator. *Sci. Drill.,* 1:206–209.

Goldberg, D., 1997. The role of downhole measurements in marine geology and geophysics. *Rev. Geophys.,* 35(3):315–342. **doi:10.1029/97RG00221**

Goodman, D.K., and Ford, L.N., Jr., 1983. Preliminary dinoflagellate biostratigraphy for the middle Eocene to lower Oligocene from the southwest Altantic Ocean. *In* Ludwig, W.J., Krasheninnikov, V.A., et al., *Init. Repts. DSDP,* 71: Washington, DC (U.S. Govt. Printing Office), 859–977. **doi:10.2973/dsdp.proc.71.131.1983**

Graber, K.K., Pollard, E., Jonasson, B., and Schulte, E. (Eds.), 2002. Overview of Ocean Drilling Program engineering tools and hardware. *ODP Tech. Note,* 31. **doi:10.2973/odp.tn.31.2002**

Gradstein, F.M., and Ogg, J., 1996. A Phanerozoic time scale. *Episodes,* 19:3–5.

Gradstein, F.M., Ogg, J.G., and Smith, A. (Eds.), 2004. *A Geologic Time Scale 2004:* Cambridge (Cambridge Univ. Press). **http://cambridge.org/uk/catalogue/catalogue.asp?isbn=9780521781428**

Habib, D., and Drugg, W.S., 1983. Dinoflagellate age of Middle Jurassic–Early Cretaceous sediments in the Blake-Bahama Basin. *In* Gradstein, F.M., Sheridan, R.E., et al., *Init. Repts. DSDP,* 76: Washington, DC (U.S. Govt. Printing Office), 623–638. **doi:10.2973/dsdp.proc.76.126.1983**

Hagelberg, T., Shackleton, N., Pisias, N., and Shipboard Scientific Party, 1992. Development of composite depth sections for Sites 844 through 854. *In* Mayer, L., Pisias, N., Janecek, T., et al., *Proc. ODP, Init. Repts.,* 138: College Station, TX (Ocean Drilling Program), 79–85. **doi:10.2973/odp.proc.ir.138.105.1992**

Hagelberg, T.K., Pisias, N.G., Shackleton, N.J., Mix, A.C., and Harris, S., 1995. Refinement of a high-resolution, continuous sedimentary section for studying equatorial Pacific Ocean paleoceanography, Leg 138. *In* Pisias, N.G., Mayer, L.A., Janecek, T.R., Palmer-Julson, A., and van Andel, T.H. (Eds.), *Proc. ODP, Sci Results,* 138: College Station, TX (Ocean Drilling Program), 31–46. **doi:10.2973/odp.proc.sr.138.103.1995**

Harding, I.C., 1990. A dinocyst calibration of the European Boreal Barremian. *Palaeontographica, Abt. B,* 218:1–76.

Harms, J.C., and Choquette, P.W., 1965. Geologic evaluation of a gamma-ray porosity device. *Trans. SPWLA Annu. Logging Symp.:* 6:C1–C37.

Harris, S., Hagelberg, T., Mix, A., Pisias, N.G., and Shackleton, N.J., 1995. Sediment depths determined by comparisons of GRAPE and logging density data during Leg 138. *In* Pisias, N.G., Mayer, L.A., Janecek, T.R., Palmer-Julson, A., and van Andel, T.H. (Eds.), *Proc. ODP, Sci. Results,* 138: College Station, TX (Ocean Drilling Program), 47–57. **doi:10.2973/odp.proc.sr.138.104.1995**

Harwood, D.M., and Bohaty, S.M., 2001. Early Oligocene siliceous microfossil biostratigraphy of Cape Roberts Project Core CRP-3, Victoria Land Basin, Antarctica. *Terra Antart.,* 8(4):315–338.

Harwood, D.M., and Maruyama, T., 1992. Middle Eocene to Pleistocene diatom biostratigraphy of Southern Ocean sediments from the Kerguelen Plateau, Leg 120. *In* Wise, S.W., Jr., Schlich, R., et al., *Proc. ODP, Sci. Results,* 120: College Station, TX (Ocean Drilling Program), 683–733. **doi:10.2973/odp.proc.sr.120.160.1992**

Head, M.J., 1993. Dinoflagellates, sporomorphs, and other palynomorphs from the upper Pliocene St. Erth beds of Cornwall, southwestern England. *Paleontol. Soc. Mem.,* 31.

Head, M.J., 1998. New goniodomacean dinoflagellates with a compound hypotractal archaeopyle from the late Cenozoic: *Capisocyst* Warny and Wrenn, emend. *J. Paleontol.,* 72(5):797-809. **http://jpaleontol.geoscienceworld.org/cgi/content/abstract/72/5/797**

Head, M.J., 2000. *Geonettia waltonensis,* a new goniodomacean dinoflagellate from the Pliocene of the North Atlantic region, and its evolutionary implications. *J. Palaeontol.*, 74(5):812–827. **doi:10.1666/0022-3360(2000)074<0812:GWANGD>2.0.CO;2**

Head, M.J., and Norris, G., 2003. New species of dinoflagellate cysts and other palynomorphs from the latest Miocene and Pliocene of DSDP Hole 603C, western North Atlantic. *J. Paleontol.*, 77(1):1–15. **doi:10.1666/0022-3360(2003)077<0001:NSODCA>2.0.CO;2**

Head, M.J., Norris, G., and Mudie, P.J., 1989. Palynology and dinocyst stratigraphy of the upper Miocene and lowermost Pliocene, ODP Leg 105, Site 646, Labrador Sea. *In* Srivastava, S.P., Arthur, M.A., Clement, B., et al., *Proc. ODP, Sci. Results,* 105: College Station, TX (Ocean Drilling Program), 423–451. **doi:10.2973/odp.proc.sr.105.135.1989**

Heilmann-Clausen, C., 1985. Dinoflagellate stratigraphy of the uppermost Danian to Ypresian in the Viborg I borehole, central Jylland, Denmark. *Dan. Geol. Unders., Raekke A,* 7:1–69.

Heilmann-Clausen, C., and Costa, L.I., 1989. Dinoflagellate zonation of the uppermost Paleocene? to lower Miocene in the Wursterheide Research Well, NW Germany. *Geol. Jahrb.,* 111:431–521.

Helby, R., Morgan, R., and Partridge, A.D., 1987. A palynological zonation of the Australian Mesozoic. *In* Jell, P.A. (Ed.), *Studies in Australian Mesozoic Palynology.* Mem.—Assoc. Australas. Palaeontol., 4:1–94.

Hoedemaeker, P.J., and Leereveld, H., 1995. Biostratigraphy and sequence stratigraphy of the Berriasian–lowest Aptian (Lower Cretaceous) of the Rio Argos succession, Caravaca, SE Spain. *Cretaceous Res.,* 16(2–3):195–230. **doi:10.1006/cres.1995.1016**

Hoek, R.P., Eshet, Y., and Almogi-Labin, A., 1996. Dinoflagellate cyst zonation of Campanian–Maastrichtian sequences in Israel. *Micropaleontology,* 42(2):125–150. **doi:10.2307/1485866**

Hollis, C.J., Handley, L., Crouch, E.M., Morgans, H.E.G., Baker, J.A., Creech, J., Collins, K.S., Gibbs, S.J., Huber, M., Schouten, S., Zachos, J.C., and Pancost, R.D., 2009. Tropical sea temperatures in the high latitude South Pacific during the Eocene. *Geology,* 37(2):99–102. **doi:10.1130/G25200A.1**

Horai, K., and Von Herzen, R.P., 1985. Measurement of heat flow on Leg 86 of the Deep Sea Drilling Project. *In* Heath, G.R., Burckle, L.H., et al., *Init. Repts. DSDP,* 86: Washington, DC (U.S. Govt. Printing Office), 759–777. **doi:10.2973/dsdp.proc.86.135.1985**

Houben, A.J.P., Bijl, P.K., Sluijs, A., and Brinkhuis, H., submitted. Phthanoperidinium escutiae sp. nov., a new and biostratigraphically important earliest Oligocene dinoflagellate cyst from the southern Atlantic Ocean, *Rev. Palaeobot. Palynol.*

Jarvis, I., Carson, G., Hart, M., Leary, P., and Tocher, B., 1988. The Cenomanian–Turonian (Late Cretaceous) anoxic event in SW England: evidence from Hooken Cliffs near Beer, se Devon. *Newsl. Stratigr.,* 18:147–164.

Kennett, J.P., and Srinivasan, M.S., 1983. *Neogene Planktonic Foraminifera: A Phylogenetic Atlas:* Stroudsburg, PA (Hutchinson Ross).

Kirsch, K.H., 1991. Dinoflagellaten-Zysten aus der Oberkreide des Helvetikums und Nordultrahelvetikums von Oberbayern. *Münchner Geowiss. Abh., Reihe A, Geol. Palaeontol.,* 22:1–306.

Köthe, A., 1990. Paleogene dinoflagellates from northwest Germany: biostratigraphy and paleoenvironment. *Geol. Jahrb., Reihe A,* 118:3–111.

Kuhlmann, G., Langereis, C.G., Munsterman, D., van Leeuwen, R.-J., Verreussel, R., Meulenkamp, J.E., and Wong, T.E., 2006. Integrated chronostratigraphy of the Pliocene–Pleistocene interval and its relation to the regional stratigraphical stages in the southern North Sea region. *Geol. Mijnbouw,* 85(1):19–35.

Kurihara, K., and Kennett, J.P., 1986. Neogene benthic foraminifers: distribution in depth traverse, southwest Pacific. *In* Kennett, J.P., von der Borch, C.C., et al., *Init. Repts. DSDP,* 90: Washington, DC (U.S. Govt. Printing Office), 1037–1077. **doi:10.2973/dsdp.proc.90.121.1986**

Lavelle, M., 2001. Strontium isotope stratigraphy and age model for CRP-2/2A, Victoria Land Basin, Antarctica. *Terra Antart.,* 7(4):611–619.

Lazarus, D., 1992. Antarctic Neogene radiolarians from the Kerguelen Plateau, Legs 119 and 120. *In* Wise, S.W., Jr., Schlich, R., et al., *Proc. ODP, Sci. Results,* 120: College Station, TX (Ocean Drilling Program), 785–809. **doi:10.2973/odp.proc.sr.120.192.1992**

Leckie, R.M., Farnham, C., and Schmidt, M.G., 1993. Oligocene planktonic foraminifer biostratigraphy of Hole 803D (Ontong Java Plateau) and Hole 628A (Little Bahama Bank), and comparison with the southern high latitudes. *In* Berger, W.H., Kroenke, L.W., Mayer, L.A., et al., *Proc. ODP, Sci. Results,* 130: College Station, TX (Ocean Drilling Program), 113–136. **doi:10.2973/odp.proc.sr.130.012.1993**

Leckie, R.M., and Webb, P.-N., 1986. Late Paleogene and early Neogene foraminifers of Deep Sea Drilling Project Site 270, Ross Sea, Antarctica. *In* Kennett, J.P., von der Borch, C.C., et al., *Init. Repts. DSDP,* 90: Washington, DC (U.S. Govt. Printing Office), 1093–1142. **doi:10.2973/dsdp.proc.90.124.1986**

Leereveld, H., 1995. Dinoflagellate cysts from the Lower Cretaceous Rio Argos succession (southeast Spain) [Ph.D. thesis]. Univ. Utrecht.

Li, Q., McGowran, B., and Brunner, C.A., 2003. Neogene planktonic foraminiferal biostratigraphy of Sites 1126, 1128, 1130, 1132, and 1134, ODP Leg 182, Great Australian Bight. *In* Hine, A.C., Feary, D.A., and Malone, M.J. (Eds.), *Proc. ODP, Sci. Results,* 182: College Station, TX (Ocean Drilling Program), 1–67. **doi:10.2973/odp.proc.sr.182.005.2003**

Londeix, L., 1990. La distribution des kystes de dinoflagellés dans les sédiments hémipélagiques (Ardèche) et pélagiques (Arc de Castellane, s.e. de la France) en domaine vocontien, du Valanginien terminal au Barrémien inférieur - biostratigraphie et relations avec la stratigraphie sequentielle. Tome II -annexes [Ph.D. thesis]. Univ. Bordeaux.

Londeix, L., and Jan Du Chêne, R., 1998. Burdigalian dinocyst stratigraphy of the stratotypic area (Bordeaux, France). *Geobios,* 31(3):283–294. **doi:10.1016/S0016-6995(98)80012-0**

Louwye, S., Head, M.J., and De Schepper, S., 2004. Dinoflagellate cyst stratigraphy and palaeoecology of the Pliocene in northern Belgium, southern North Sea Basin. *Geol. Mag.,* 141(3):353–378. **doi:10.1017/S0016756804009136**

Louwye, S., and Mertens, K.N., 2008. New dinoflagellate cysts from the Miocene of the Porcupine Basin, offshore southwest Ireland. *Palynology,* 32(1):131–142. **doi:10.2113/gspalynol.32.1.131**

Lovell, M.A., Harvey, P.K., Brewer, T.S., Williams, C., Jackson, P.D., and Williamson, G., 1998. Application of FMS images in the Ocean Drilling Program: an overview. *In* Cramp, A., MacLeod, C.J., Lee, S.V., and Jones, E.J.W. (Eds.), *Geological Evolution of Ocean Basins: Results from the Ocean Drilling Program.* Geol. Soc. Spec. Publ., 131(1):287–303. **doi:10.1144/GSL.SP.1998.131.01.18**

Mackensen, A., 1992. Neogene benthic foraminifers from the southern Indian Ocean (Kerguelen Plateau): biostratigraphy and paleoecology. *In* Wise, S.W., Jr., Schlich, R., et al., *Proc. ODP, Sci. Results,* 120: College Station, TX (Ocean Drilling Program), 649–673. **doi:10.2973/odp.proc.sr.120.167.1992**

Mackensen, A., and Berggren, W.A., 1992. Paleogene benthic foraminifers from the southern Indian Ocean (Kerguelen Plateau): biostratigraphy and paleoecology. *In* Wise, S.W., Jr., Schlich, R., et al., *Proc. ODP, Sci. Results,* 120: College Station, TX (Ocean Drilling Program), 603–630. **doi:10.2973/odp.proc.sr.120.168.1992**

Mackensen, A., Grobe, H., Kuhn, G., and Fütterer, D.K., 1990. Benthic foraminiferal assemblages from the eastern Weddell Sea between 68 and 73°S: distribution, ecology and fossilization potential. *Mar. Micropaleontol.,* 16(3–4):241–283. **doi:10.1016/0377-8398(90)90006-8**

Manheim, F.T., and Sayles, F.L., 1974. Composition and origin of interstitial waters of marine sediments, based on deep sea drill cores. *In* Goldberg, E.D. (Ed.), *The Sea* (Vol. 5): *Marine Chemistry: The Sedimentary Cycle:* New York (Wiley), 527–568.

Martini, E., 1971. Standard Tertiary and Quaternary calcareous nannoplankton zonation. *Proc. Int. Conf. Planktonic Microfossils,* 2:739–785.

Mazzullo, J.M., Meyer, A., and Kidd, R.B., 1988. New sediment classification scheme for the Ocean Drilling Program. *In* Mazzullo, J.M., and Graham, A.G. (Eds.), *Handbook for shipboard sedimentologists*. ODP Tech. Note, 8:45–67. **doi:10.2973/odp.tn.8.1988**

McIntosh, W.C., 2000. ^{40}Ar/^{39}Ar geochronology of tephra and volcanic clasts in CRP-2A, Victoria Land Basin, Antarctica. *Terra Antart.,* 7(4):621–630.

McMinn, A., 1992. Pliocene through Holocene dinoflagellate cyst biostratigraphy of the Gippsland Basin, Australia. *In* Head, M.J., and Wrenn, J.H. (Eds.), *Neogene and Quaternary Dinoflagellate Cysts and Acritarchs:* Salt Lake City, UT (Publishers Press), 147–161.

Miller, K.G., and Katz, M.E., 1987. Oligocene to Miocene benthic foraminiferal and abyssal circulation changes in the North Atlantic. *Micropaleontology,* 33(2):97–149. **doi:10.2307/1485489**

Moncrieff, A.C.M., 1989. Classification of poorly-sorted sedimentary rocks. *Sediment. Geol.,* 65(1–2):191–194. **doi:10.1016/0037-0738(89)90015-8**

Monteil, E., 1985. Les dinokystes du Valanginien du Bassin du Sud-Est (Ardèche, France) [Ph.D Thesis]. L'Univ. Pierre et Marie Curie, Paris.

Monteil, E., 1992. Kystes de dinoflagellés index (Tithonique-Valanginien) du sud-est de la France: proposition d'une nouvelle zonation palynologique. *Rev. Paleobiol.,* 11:299–306.

Moran, K., 1997. Elastic property corrections applied to Leg 154 sediment, Ceara Rise. *In* Shackleton, N.J., Curry, W.B., Richter, C., and Bralower, T.J. (Eds.), *Proc. ODP, Sci. Results,* 154: College Station, TX (Ocean Drilling Program), 151–155. **doi:10.2973/odp.proc.sr.154.132.1997**

Mudge, D.C., and Bujak, J.P., 1994. Eocene stratigraphy of the North Sea Basin. *Mar. Petrol. Geol.,* 11(2):166–181. **doi:10.1016/0264-8172(94)90093-0**

Munsterman, D.K, and Brinkhuis, H., 2004. A southern North Sea Miocene dinoflagellate cyst zonation. *Geol. Mijnbouw,* 83(4):267–285. **http://www.njgonline.nl/publish/articles/000060/article.pdf**

Murray, R.W., Miller, D.J., and Kryc, K.A., 2000. Analysis of major and trace elements in rocks, sediments, and interstitial waters by inductively coupled plasma–atomic emission spectrometry (ICP-AES). *ODP Tech. Note,* 29. **doi:10.2973/odp.tn.29.2000**

Naish, T.R., Levy, R.H., Powell, R.D., and MIS Science and Operations Team Members, 2006. *Scientific Logistics*

Implementation Plan for the ANDRILL McMurdo Ice Shelf Project, ANDRILL Contribution 7: Lincoln, NE (Univ. Nebraska-Lincoln). **http://www.andrill.org/projects/mis**

Ogg, J.G., Ogg, G., and Gradstein, F.M., 2008. *The Concise Geologic Time Scale*: Cambridge (Cambridge Univ. Press). **http://www.cambridge.org/catalogue/catalogue.asp?isbn=9780521898492**

Okada, H., and Bukry, D., 1980. Supplementary modification and introduction of code numbers to the low-latitude coccolith biostratigraphic zonation (Bukry, 1973; 1975). *Mar. Micropaleontol.,* 5:321–325. **doi:10.1016/0377-8398(80)90016-X**

Olney, M.P., Scherer, R.P., Harwood, D.M., and Bohaty, S.M., 2007. Oligocene–early Miocene Antarctic nearshore diatom biostratigraphy. *Deep-Sea Res., Part II*, 54(21–22):2325–2349. **doi:10.1016/j.dsr2.2007.07.020**

Pälike, H., Moore, T., Backman, J., Raffi, I., Lanci, L., Parés, J.M., and Janecek, T., 2005. Integrated stratigraphic correlation and improved composite depth scales for ODP Sites 1218 and 1219. *In* Wilson, P.A., Lyle, M., and Firth, J.V. (Eds.), *Proc. ODP, Sci. Results,* 199: College Station, TX (Ocean Drilling Program), 1–41. **doi:10.2973/odp.proc.sr.199.213.2005**

Pearce, M.A., 2000. Palynology and chemostratigraphy of the Cenomanian to lower Campanian chalk of southern and eastern England [Ph.D. thesis]. Kingston Univ., London.

Pearce, M.A., Jarvis, I., Swan, A.R.H., Murphy, A.M., Tocher, B.A., and Edmunds, W.M., 2003. Integrating palynological and geochemical data in a new approach to palaeoecological studies: Upper Cretaceous of the Banterwick Barn Chalk Borehole, Berkshire, UK. *Mar. Micropaleontol.,* 47(3–4):271–306. **doi:10.1016/S0377-8398(02)00132-9**

Pearson, P.N., Olsson, R.K., Huber, B.T., Hemleben, C., and Berggren, W.A. (Eds.), 2006. *Atlas of Eocene Planktonic Foraminifera*. Spec. Publ.—Cushman Found. Foraminiferal Res., 41.

Perch-Nielsen, K., 1985. Cenozoic calcareous nannofossils. *In* Bolli, H.M., Saunders, J.B., and Perch-Nielsen, K. (Eds.), *Plankton Stratigraphy:* Cambridge (Cambridge Univ. Press), 427–554.

Pimmel, A., and Claypool, G., 2001. Introduction to shipboard organic geochemistry on the *JOIDES Resolution. ODP Tech. Note,* 30. **doi:10.2973/odp.tn.30.2001**

Powell, A.J. (Ed.), 1992. *A Stratigraphic Index of Dinoflagellate Cysts:* London (Springer).

Powell, A.J., Brinkhuis, H., and Bujak, J.P., 1996. Upper Paleocene–lower Eocene dinoflagellate cyst sequence biostratigraphy of southeast England. *In* Knox, R.W.O'B, Corfield, R.M., and Dunay, R.E. (Eds.), *Correlation of the Early Paleogene in Northwest Europe*. Geol. Soc. Spec. Publ., 101(1):145–183. **doi:10.1144/GSL.SP.1996.101.01.10**

Pribnow, D.F.C., Kinoshita, M., and Stein, C.A., 2000. *Thermal Data Collection and Heat Flow Recalculations for ODP Legs 101–180:* Hanover, Germany (Inst. Joint Geosci. Res., Inst. Geowiss. Gemeinschaftsauf. [GGA]). **http://www-odp.tamu.edu/publications/heatflow/ODPReprt.pdf**

Prince, I.M., 1997. Palynology of the upper Turonian to lower Campanian chalks of Southern England [Ph.D. thesis]. Univ. Wales, Aberystwyth, U. K.

Prince, I.M., Jarvis, I., and Tocher, B.A., 1999. High-resolution dinoflagellate cyst biostratigraphy of the Santonian–basal Campanian (Upper Cretaceous): new data from Whitecliff, Isle of Wight, England. *Rev. Palaeobot. Palynol.,* 105:143–169.

Pross, J., Houben, A.J.P., van Simaeys, S., Williams, G.L., Kotthoff, U., Coccioni, R., Wilpshaar, M., and Brinkhuis, H., 2010. Umbria-Marche revisited: a refined magnetostratigraphic calibration of dinoflagellate cyst events for the Oligocene of the western Tethys. *Rev. Palaeobot. Palynol.,* 158(3–4):213–235. **doi:10.1016/j.revpalbo.2009.09.002**

Prössl, K.F., 1990. Dinoflagellaten der Kreide—Unter-Hauterive bis Ober-Turon—im Niedersächsischen Becken. Stratigraphie und Fazies in der Kernbohrung Konrad 101 sowie einiger anderer Bohrungen in Nordwestdeutschland. *Palaeontographica, Abt. B,* 218:93–191.

Raine, J.I., Askin, R.A., Crouch, E.M., Hannah, M.J., Levy, R.H., and Wrenn, J.H., 1997. Palynomorphs. *In* Hannah, M.J., and Raine, J.I. (Eds), *Southern Ocean Late Cretaceous/Early Cenozoic Biostratigraphic Datums*. Inst. Geol. Nucl. Sci., Sci. Rep., 97:25–33.

Rider, M.H., 1996. *The Geological Interpretation of Well Logs* (2nd ed.): Caithness (Whittles Publ.).

Robaszynski, F., Alcayde, G., Amedro, F., Badillet, G., Damotte, R., Foucher, J.-C., Jardine, S., Legoux, O., Manivit, H., Monciardini, C., and Sornay, J., 1982. Le Turonien de la région-type: Saumurois et Touraine. Stratigraphie, biozonations, sédimentologie. *Bull. Cent. Rech. Explor.-Prod. Elf-Aquitaine,* 6:119–225.

Rögl, F., 1976. Late Cretaceous to Pleistocene foraminifera from the Southeast Pacific Basin, DSDP Leg 35. *In* Hollister, C.D., Craddock, C., et al., *Init. Repts. DSDP,* 35: Washington, DC (U.S. Govt. Printing Office), 539–555. **doi:10.2973/dsdp.proc.35.133.1976**

Roncaglia, L., Field, B.D., Raine, J.I., Schiøler, P., and Wilson, G.J., 1999. Dinoflagellate biostratigraphy of Piripauan–Haumurian (Upper Cretaceous) sections from the northeast South Island, New Zealand. *Cretaceous Res.,* 20(3):271–314. **doi:10.1006/cres.1999.0153**

Ruddiman, W.F., Cameron, D., and Clement, B.M., 1987. Sediment disturbance and correlation of offset holes drilled with the hydraulic piston corer: Leg 94. *In* Ruddiman, W.F., Kidd, R.B., Thomas, E., et al., *Init. Repts. DSDP,* 94: Washington, DC (U.S. Govt. Printing Office), 615–634. **doi:10.2973/dsdp.proc.94.111.1987**

Scherer, R.P., Bohaty, S.M., and Harwood, D.M., 2000. Oligocene and lower Miocene siliceous microfossil biostratigraphy of Cape Roberts Project core CRP-2/2A, Victoria Land Basin, Antarctica. *Terra Antart.,* 7(4):417–442.

Schiøler, P., and Wilson, G.J., 1993. Maastrichtian dinoflagellate zonation in the Dan Field, Danish North Sea. *Rev. Palaeobot. Palynol.,* 78(3–4):321–351. **doi:10.1016/0034-6667(93)90070-B**

Schlumberger, 1989. *Log Interpretation Principles/Applications:* Houston (Schlumberger Educ. Serv.), SMP–7017.

Schlumberger, 1994. *IPL Integrated Porosity Lithology:* Houston (Schlumberger Wireline Testing), SMP-9270.

Schrader, H.J., and Gersonde, R., 1978. Diatoms and silicoflagellates. *In* Zachariasse, W.J., et al. (Eds.), *Micropaleontological Counting Methods and Techniques: An Exercise of an Eight Metres Section of the Lower Pliocene of Cap Rossello, Sicily.* Utrecht Micropaleontol. Bull., 17:129–176.

Schröder-Adams, C.J., 1991. Middle Eocene to Holocene benthic foraminifer assemblages from the Kerguelen Plateau (southern Indian Ocean). *In* Barron, J., Larsen, B., et al., *Proc. ODP, Sci. Results,* 119: College Station, TX (Ocean Drilling Program), 611–630. **doi:10.2973/odp.proc.sr.119.152.1991**

Serra, O., 1984. *Fundamentals of Well-Log Interpretation* (Vol. 1): *The Acquisition of Logging Data:* Amsterdam (Elsevier).

Serra, O., 1986. *Fundamentals of Well-Log Interpretation* (Vol. 2): *The Interpretation of Logging Data.* Amsterdam (Elsevier).

Serra, O., 1989. *Formation MicroScanner Image Interpretation:* Houston (Schlumberger Educ. Serv.), SMP-7028.

Shipboard Scientific Party, 2001. Explanatory notes. *In* O'Brien, P.E., Cooper, A.K., Richter, C., et al., *Proc. ODP, Init. Repts.,* 188: College Station, TX (Ocean Drilling Program), 1–66. **doi:10.2973/odp.proc.ir.188.102.2001**

Shipboard Scientific Party, 2003. Explanatory notes. *In* D'Hondt, S.L., Jørgensen, B.B., Miller, D.J., et al., *Proc. ODP, Init. Repts.,* 201: College Station, TX (Ocean Drilling Program), 1–103. **doi:10.2973/odp.proc.ir.201.105.2003**

Sluijs, A., and Brinkhuis, H., 2009. A dynamic climate and ecosystem state during the Paleocene–Eocene Thermal Maximum: inferences from dinoflagellate cyst assemblages on the New Jersey shelf. *Biogeosciences,* 6(8):1755–1781. **doi:10.5194/bg-6-1755-2009**

Sluijs, A., Brinkhuis, H., Williams, G.L., and Fensome, R.A., 2009. Taxonomic revision of some Cretaceous–Cenozoic spiny organic-walled peridiniacean dinoflagellate cysts. *Rev. Palaeobot. Palynol.,* 154(1–4):34–53. **doi:10.1016/j.revpalbo.2008.11.006**

Stover, L.E., and Hardenbol, J., 1993. Dinoflagellates and depositional sequences in the lower Oligocene (Rupelian) Boom Clay Formation, Belgium. *Bull. Soc. Belge Geol.,* 102(1–2):5–77.

Stover, L.E., and Williams, G.L., 1995. A revision of the Paleogene dinoflagellate genera *Areosphaeridium* Eaton 1971 and *Eatonicysta* Stover and Evitt 1978. *Micropaleontology,* 41(2):97–141. **doi:10.2307/1485947**

Takemura, A., 1992. Radiolarian Paleogene biostratigraphy in the southern Indian Ocean, Leg 120. *In* Wise, S.W., Jr., Schlich, R., et al., *Proc. ODP, Sci. Results,* 120: College Station, TX (Ocean Drilling Program), 735–756. **doi:10.2973/odp.proc.sr.120.177.1992**

Tauxe, L., Butler, R.F., and Van Der Voo, R., 2010. *Essentials of Paleomagnetism:* Berkeley (Univ. California Press).

Terry, R.D., and Chilingar, G.V., 1955. Summary of "Concerning some additional aids in studying sedimentary formations," by M. S. Shvetsov. *J. Sediment. Res.,* 25(3):229–234. **http://jsedres.geoscienceworld.org/cgi/content/abstract/25/3/229**

Thomas, E., 1990. Late Cretaceous through Neogene deep-sea benthic foraminifers (Maud Rise, Weddell Sea, Antarctica). *In* Barker, P.F., Kennett, J.P., et al., *Proc. ODP, Sci. Results,* 113: College Station, TX (Ocean Drilling Program), 571–594. **doi:10.2973/odp.proc.sr.113.123.1990**

Tocher, B.A., and Jarvis, I., 1987. Dinoflagellate cysts and stratigraphy of the Turonian (Upper Cretaceous) chalk near Beer, southeast Devon, England. *In* Hart, M.B. (Ed.), *Micropalaeontology of Carbonate Environments:* Chichester, U.K. (Ellis Horwood), 138–175.

Torricelli, S., Knezaurek, G., and Biffi, U., 2006. Sequence biostratigraphy and paleoenvironmental reconstruction in the early Eocene Figols Group of the Tremp–Graus Basin (south-central Pyrenees, Spain). *Palaeogeogr., Palaeoclimatol., Palaeoecol.,* 232(1):1–35. **doi:10.1016/j.palaeo.2005.08.009**

Truswell, E.M., 1997. Palynomorph assemblages from marine Eocene sediments on the West Tasmanian continental margin and the South Tasman Rise. *Aust. J. Earth Sci.,* 4(5):633–654. **doi:10.1080/08120099708728342**

van Morkhoven, F.P.C.M., Berggren, W.A., and Edwards, A.S., 1986. *Cenozoic Cosmopolitan Deep-Water Benthic Foraminifera.* Bull. Cent. Rech. Explor.—Prod. Elf-Aquitaine, 11.

Van Simaeys, S., De Man, E., Vandenberghe, N., Brinkhuis, H., and Steurbaut, E., 2004. Stratigraphic and paleoenvironmental analysis of the Rupelian–Chattian transition in the type region: evidence from dinoflagellate cysts, foraminifera and calcareous nannofossils. *Palaeogeogr., Palaeoclimatol., Palaeoecol.,* 208(1–2):31–58. **doi:10.1016/j.palaeo.2004.02.029**

Verdier, J.-P., 1975. Les kystes de dinoflagellés de la section de Wissant et leur distribution stratigraphique au Crétacé moyen. *Rev. Micropaleontol.,* 17:191–197.

Versteegh, G.J.M., 1997. The onset of major Northern Hemisphere glaciations and their impact on dinoflagellate cysts and acritarchs from the Singa section, Calabria (southern Italy) and DSDP Holes 607/607A (North Atlantic). *Mar. Micropaleontol.,* 30(4):319–343. **doi:10.1016/S0377-8398(96)00052-7**

Versteegh, G.J.M., and Zevenboom, D., 1995. New genera and species of dinoflagellate cysts from the Mediterranean Neogene. *Rev. Palaeobot. Palynol.,* 85(3–4):213–229. **doi:10.1016/0034-6667(94)00127-6**

Von Herzen, R., and Maxwell, A.E., 1959. The measurement of thermal conductivity of deep-sea sediments by a needle-probe method. *J. Geophys. Res.,* 64(10):1557–1563. **doi:10.1029/JZ064i010p01557**

Webb, P.N., 1989. Benthic foraminifera. *In* Barrett, P.J. (Ed.), *Antarctic Cenozoic Hisory from the CIROS-1 Drillhole, McMurdo Sound.* DSIR Bull., 245:99–118.

Webb, P.-N., and Strong, C.P., 2006. Foraminiferal biostratigraphy and palaeocology in upper Oligocene–lower Miocene glacial marine sequences 9, 10, and 11, CRP-2/2A drill hole, Victoria Land Basin, Antarctica. *Palaeo-*

geogr., Palaeoclimatol., Palaeoecol., 231(1–2):71–100. **doi:10.1016/j.palaeo.2005.07.036**

Wentworth, C.K., 1922. A scale of grade and class terms for clastic sediments. *J. Geol.,* 30(5):377–392. **doi:10.1086/622910**

Williams, G.L., Brinkhuis, H., Pearce, M.A., Fensome, R.A., and Weegink, J.W., 2004. Southern Ocean and global dinoflagellate cyst events compared: index events for the Late Cretaceous–Neogene. *In* Exon, N.F., Kennett, J.P., and Malone, M.J. (Eds.), *Proc. ODP, Sci. Results,* 189: College Station, TX (Ocean Drilling Program), 1–98. **doi:10.2973/odp.proc.sr.189.107.2004**

Williams, G.L., Stover, L.E., and Kidson, E.J., 1993. *Morphology and Stratigraphic Ranges of Selected Mesozoic-Cenozoic Dinoflagellate Taxa in the Northern Hemisphere:* Ottawa, ON (Geol. Surv. Can.).

Wilpshaar, M., 1995. Direct stratigraphic correlation of the Vercors carbonate platform in SE France with the Barremian stratotype by means of dinoflagellate cysts. *Cretaceous Res.,* 16(2–3):273–281. **doi:10.1006/cres.1995.1020**

Wilpshaar, M., Santarelli, A., Brinkhuis, H., and Visscher, H., 1996. Dinoflagellate cysts and mid-Oligocene chronostratigraphy in the central Mediterranean region. *J. Geol. Soc. (London, U.K.),* 153(4):553–561. **doi:10.1144/gsjgs.153.4.0553**

Wilson, G.J., 1974. Upper Campanian and Maastrichtian dinoflagellate cysts from the Maastricht region and Denmark [Ph.D. dissert.]. Nottingham Univ.

Wilson, G.J., 1988. Paleocene and Eocene dinoflagellate cysts from Waipawa, Hawkes Bay, New Zealand. *N. Z. Geol. Surv. Bull.,* 57:1–96.

Wrenn, J.H., and Hart, G.F., 1988. Paleogene dinoflagellate cyst biostratigraphy of Seymour Island, Antarctica. *Mem.—Geol. Soc. Am.,* 169:321–447.

Zevenboom, D., 1995. Dinoflagellate cysts from the Mediterranean late Oligocene and Miocene [Ph.D. thesis]. Univ. Utrecht, The Netherlands.

Zielinski, U., and Gersonde, R., 2002. Plio–Pleistocene diatom biostratigraphy from ODP Leg 177, Atlantic sector of the Southern Ocean. *Mar. Micropaleontol.,* 45:225–268. **doi:10.1016/S0377-8398(02)00031-2**

Publication: 2 July 2011
MS 318-102

Figure F1. IODP conventions for naming sites, holes, cores, and samples. CC = core catcher.

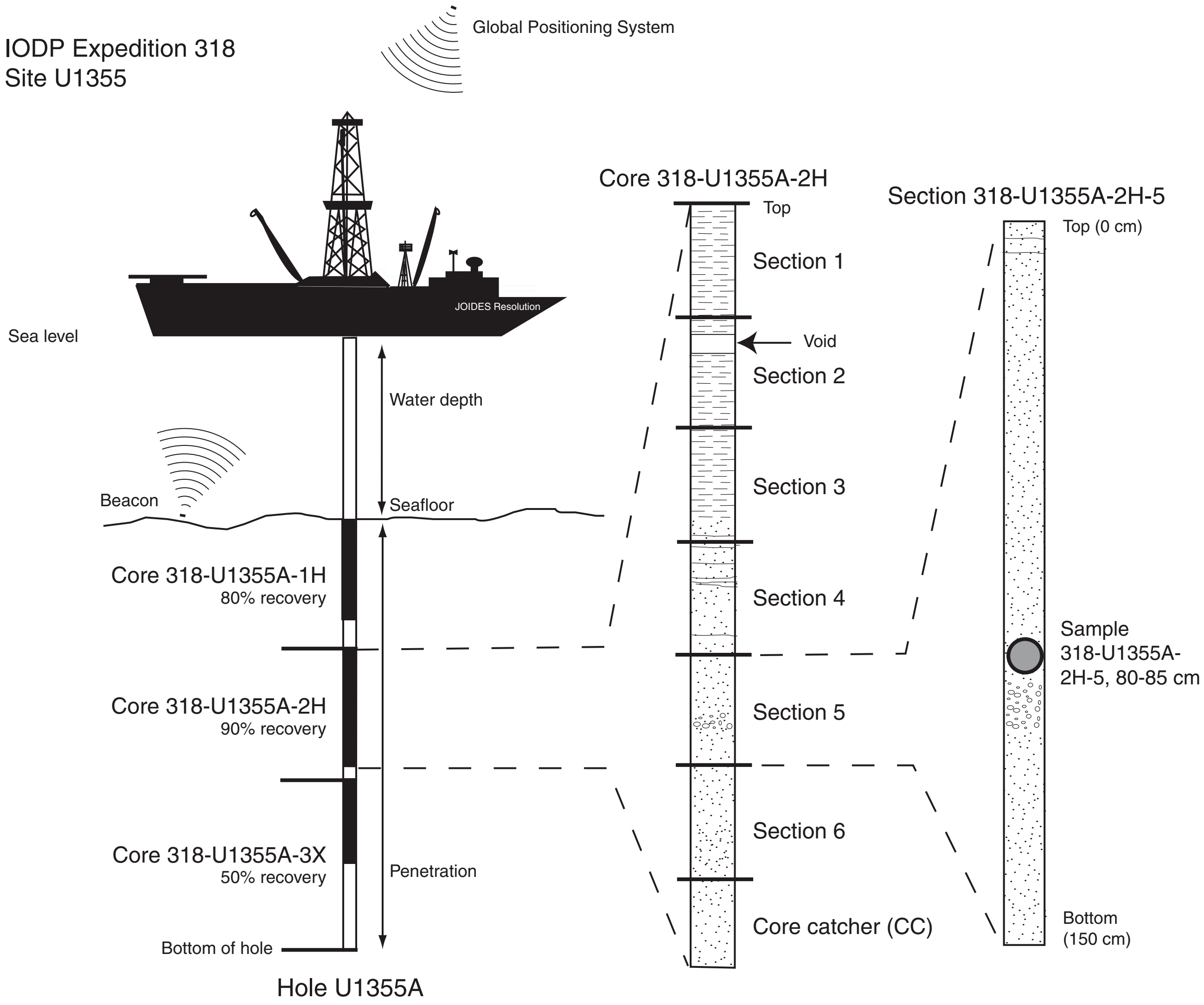

Figure F2. Barrel sheet legend, Expedition 318.

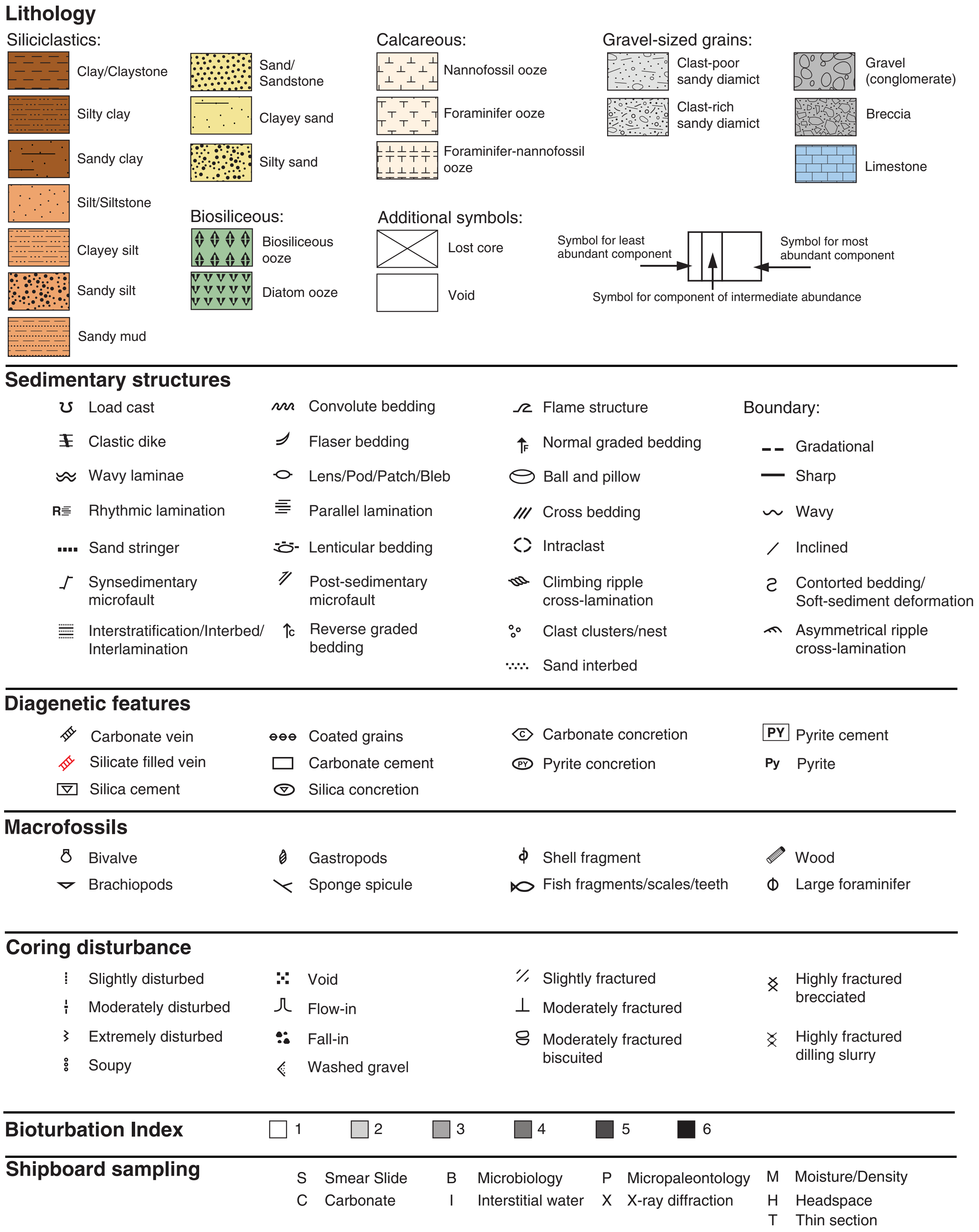

Figure F3. Classification scheme for terrigenous clastic sediments lacking a gravel component, Expedition 318 (after Mazzullo et al., 1988).

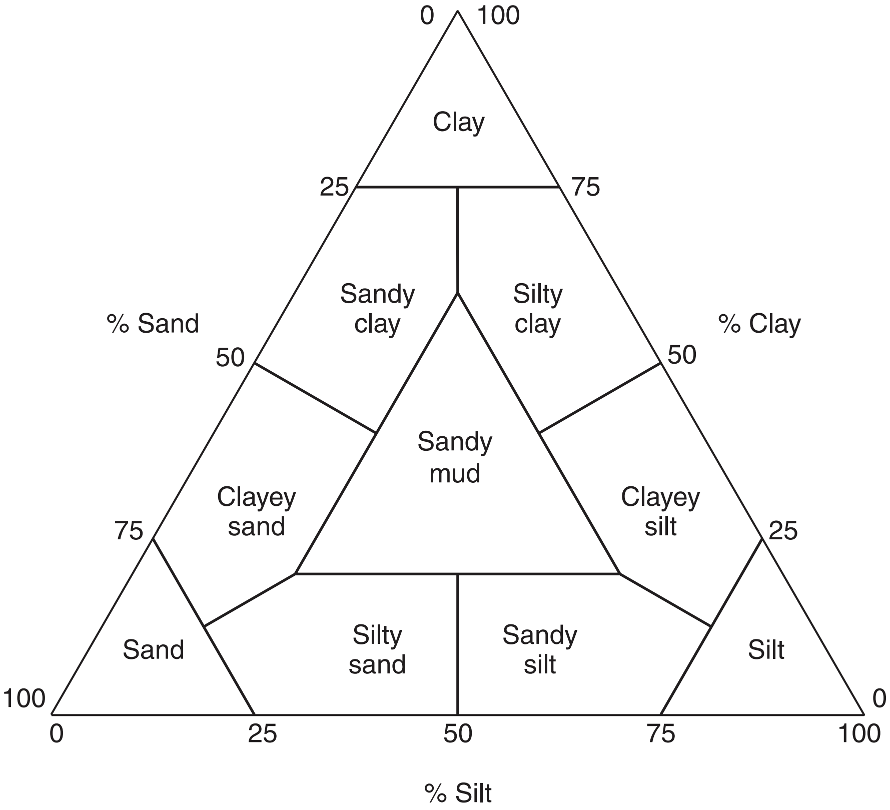

Figure F4. Classification scheme for terrigenous clastic sediments containing a gravel component, Expedition 318 (after Moncrieff, 1989).

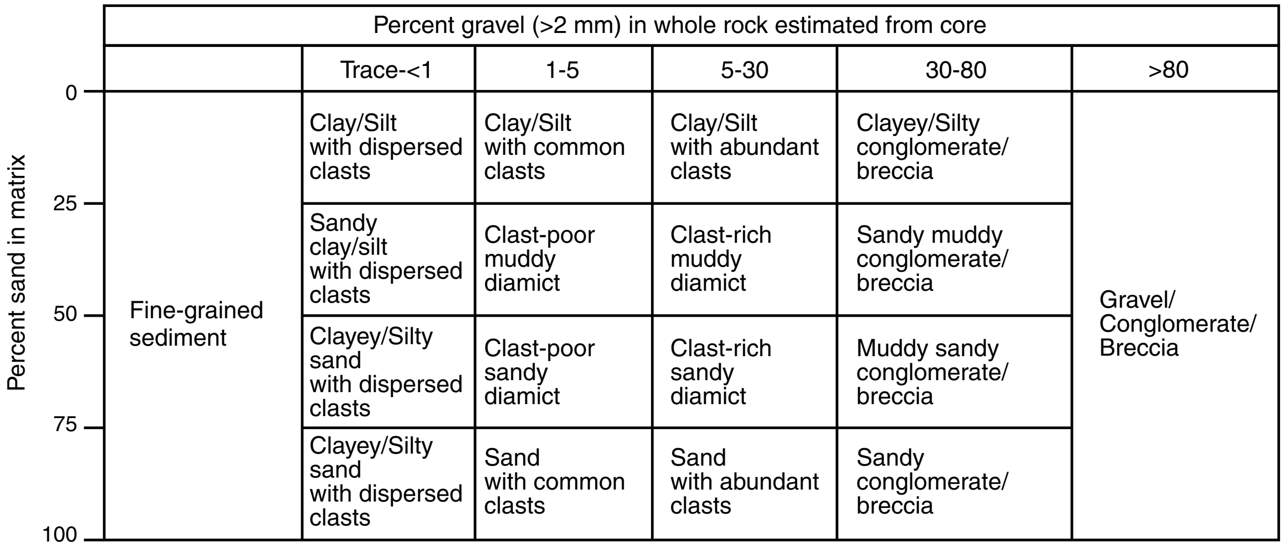

	Percent gravel (>2 mm) in whole rock estimated from core				
	Trace-<1	1-5	5-30	30-80	>80
Fine-grained sediment	Clay/Silt with dispersed clasts	Clay/Silt with common clasts	Clay/Silt with abundant clasts	Clayey/Silty conglomerate/ breccia	Gravel/ Conglomerate/ Breccia
	Sandy clay/silt with dispersed clasts	Clast-poor muddy diamict	Clast-rich muddy diamict	Sandy muddy conglomerate/ breccia	
	Clayey/Silty sand with dispersed clasts	Clast-poor sandy diamict	Clast-rich sandy diamict	Muddy sandy conglomerate/ breccia	
	Clayey/Silty sand with dispersed clasts	Sand with common clasts	Sand with abundant clasts	Sandy conglomerate/ breccia	

Figure F5. Classification scheme for sediments that are mixtures of pelagic biogenic and terrigenous clastic components, Expedition 318.

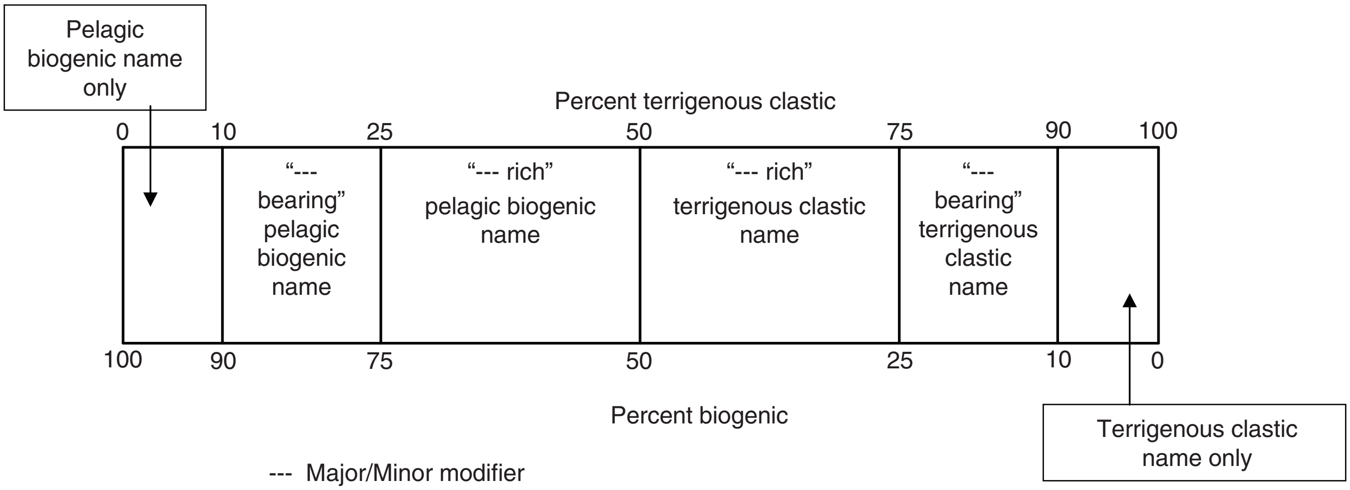

Figure F6. Composite range chart of diatom taxa used during Expedition 318 (from Cody et al., 2008). Black lines = total range model, gray shaded lines = average range model.

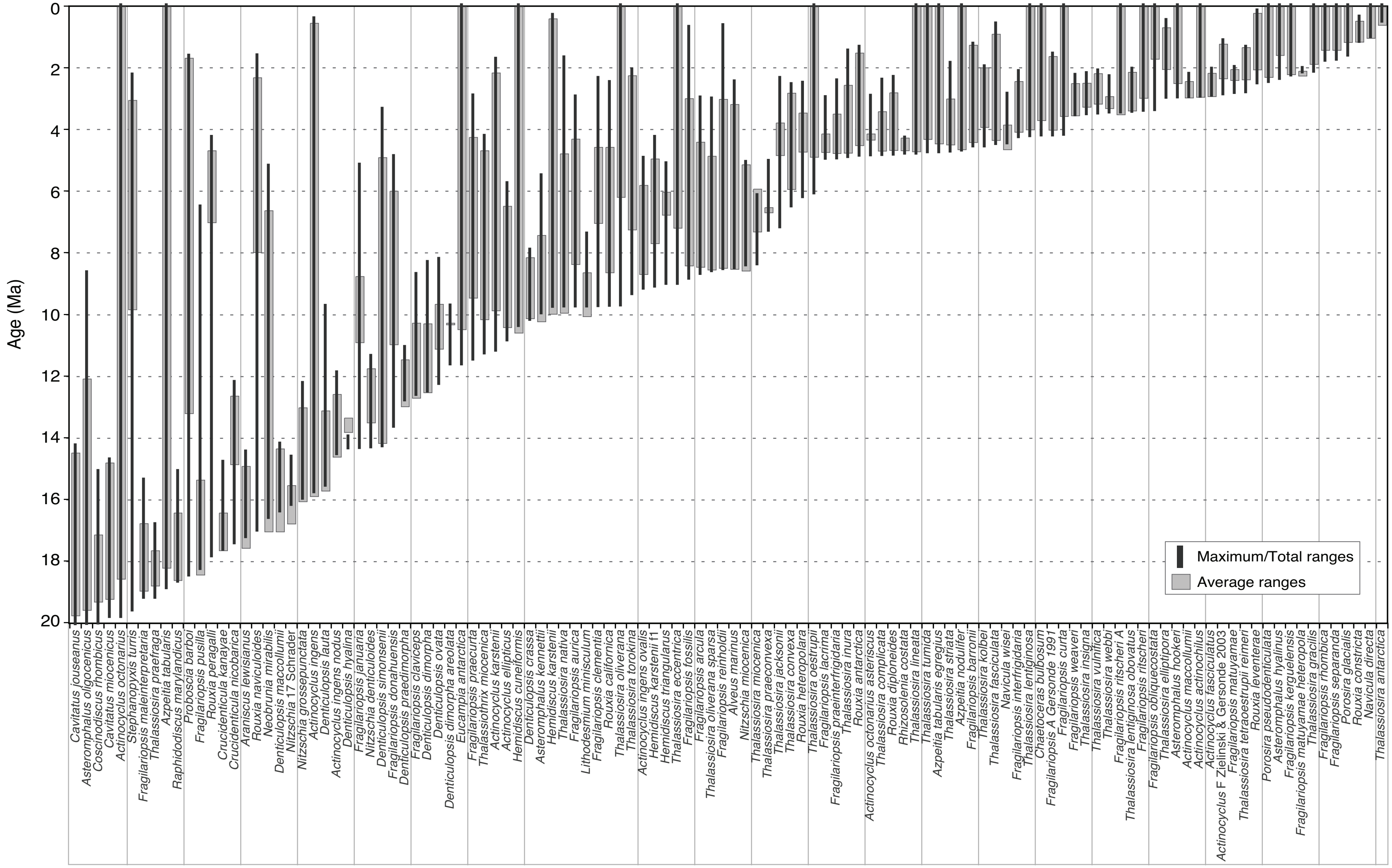

Figure F7. Stratigraphic ranges of index siliceous microfossil species or species groups in Cape Roberts Project (CRP)-2/2A (from Olney et al., 2007). Bold = taxa used in the common occurrence zonation and diatom zonation of Scherer et al. (2000). H&B = Harwood and Bohaty (2001), SB&H = Scherer et al. (2000). Cross-hatched rectangles = intervals of low microfossil abundance that were not sampled for this study. Ages followed by Sr or Ar are strontium and argon isotope ages of Lavelle (2001) and McIntosh (2000). Remaining ages are Southern Ocean diatom datums (see Olney et al., 2007, for list of references).

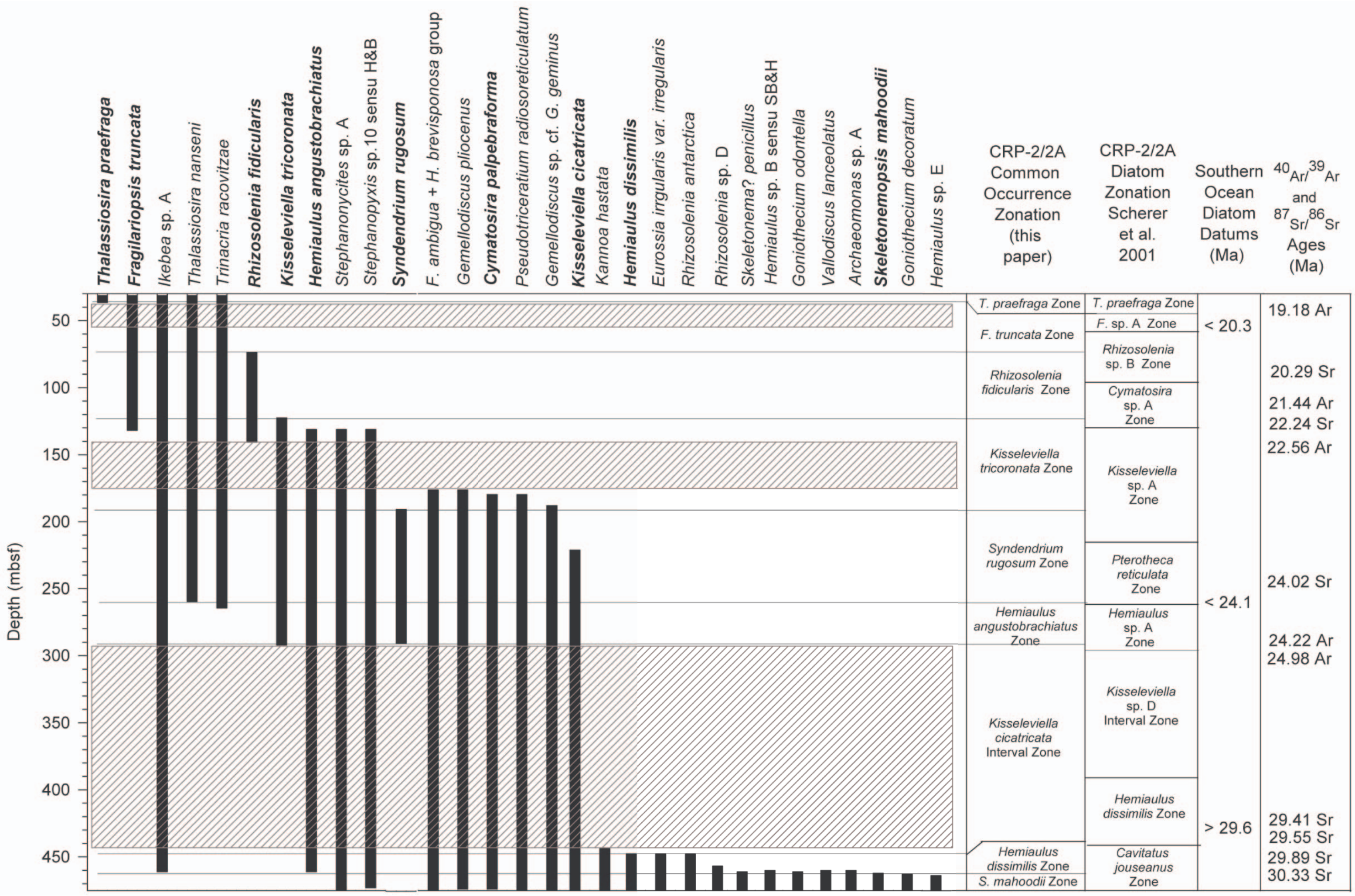

Figure F8. Radiolarian zonation used during Expedition 318. After Lazarus (1992), revised to the Gradstein et al. (2004) GPTS.

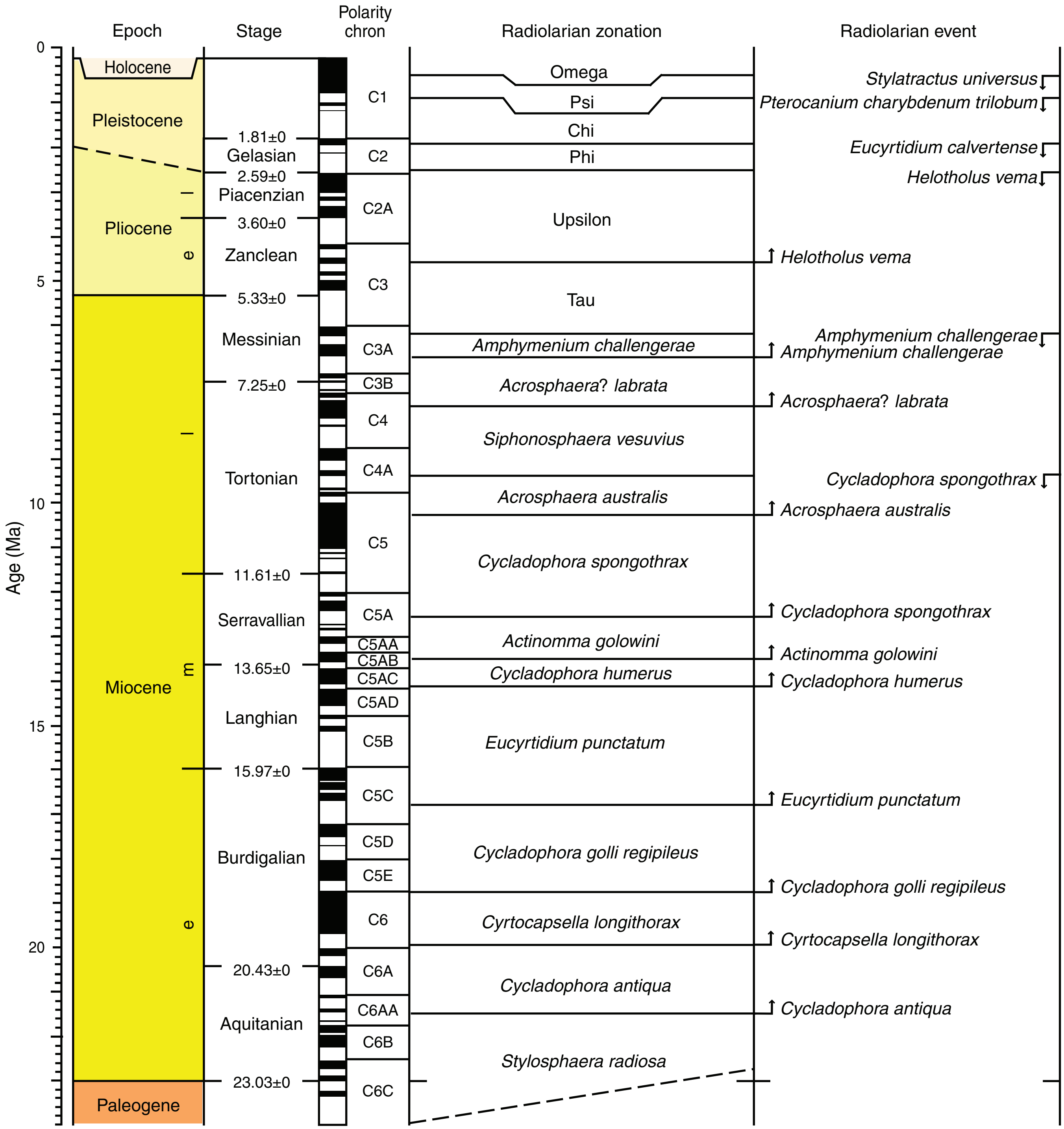

Figure F9. Coordinate systems used for archive- and working-half sections and for the super-conducting quantum interference device (SQUID) and software during Expedition 318. Note that the software and hardware conventions are different for the 2G.

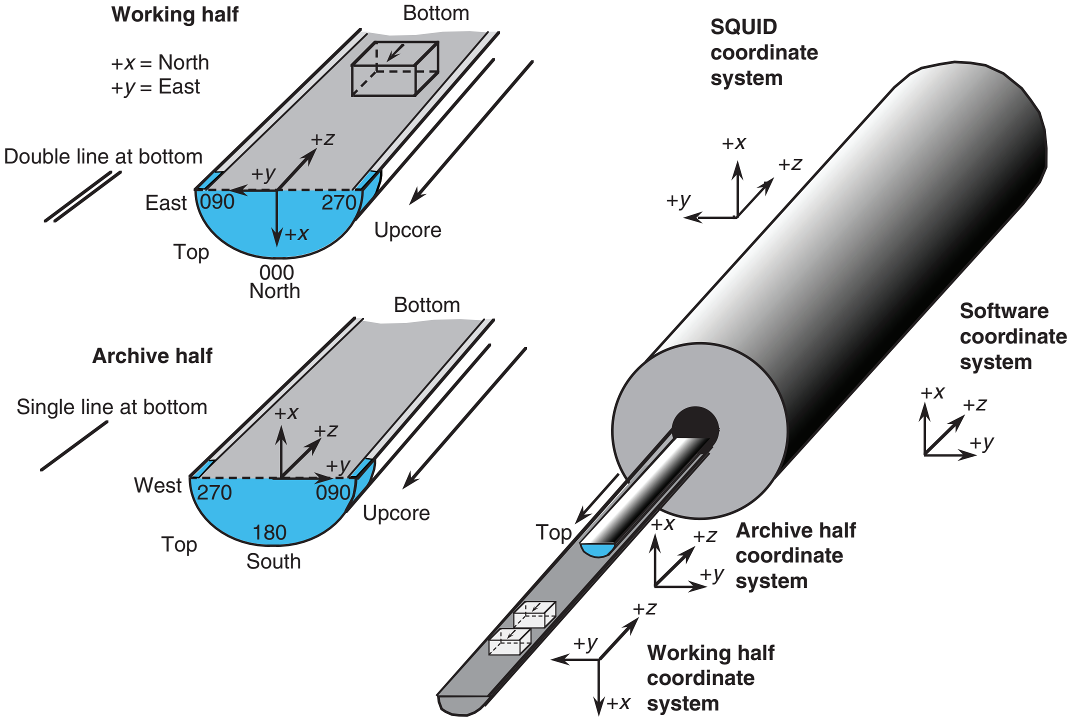

Figure F10. **A.** Natsuhara sampling cubes (7 cm^3) shown with sample coordinate system used during Expedition 318. Hatched arrow is the “up” arrow and in the $-z$ sample direction. **B.** Measurement positions. Designations (e.g., “Top-Toward”) refer to the direction of the up arrow face (gray) with respect to a user facing the magnetometer in the sample loading area and the direction of the up arrow with respect to the magnetometer $+z$-axis, therefore top-toward means samples are put into the measurement tray with the up arrow face on top and the arrow facing in the magnetometer $+z$ direction.

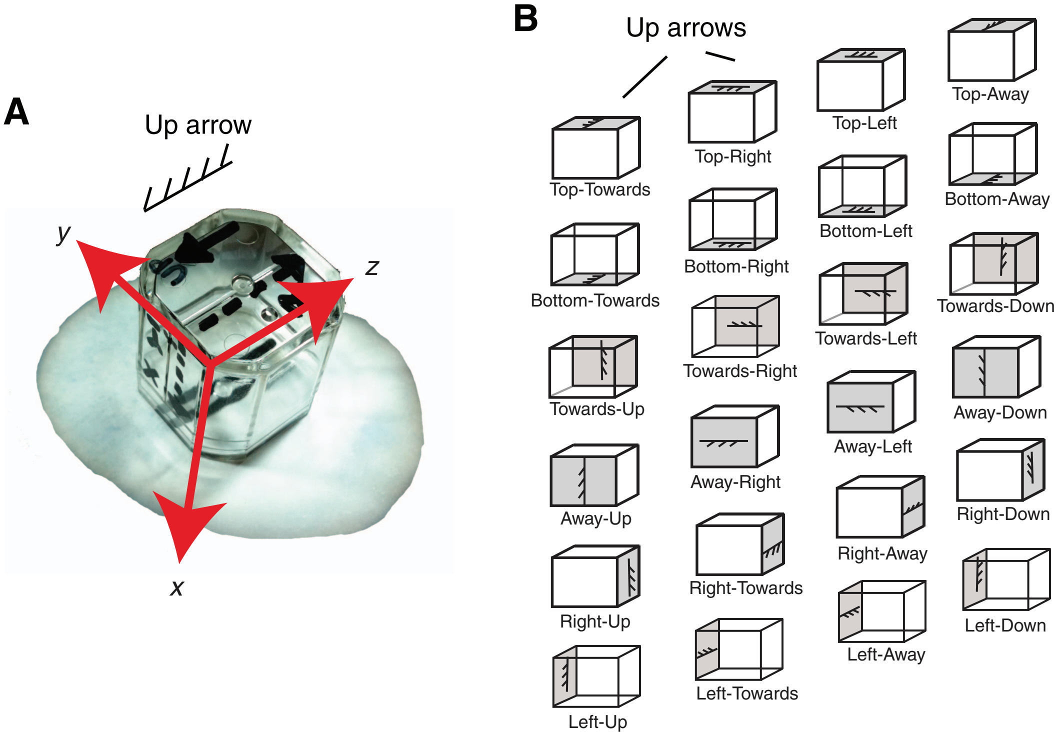

Figure F11. Discrete samples in sample tray in top-toward orientation, Expedition 318.

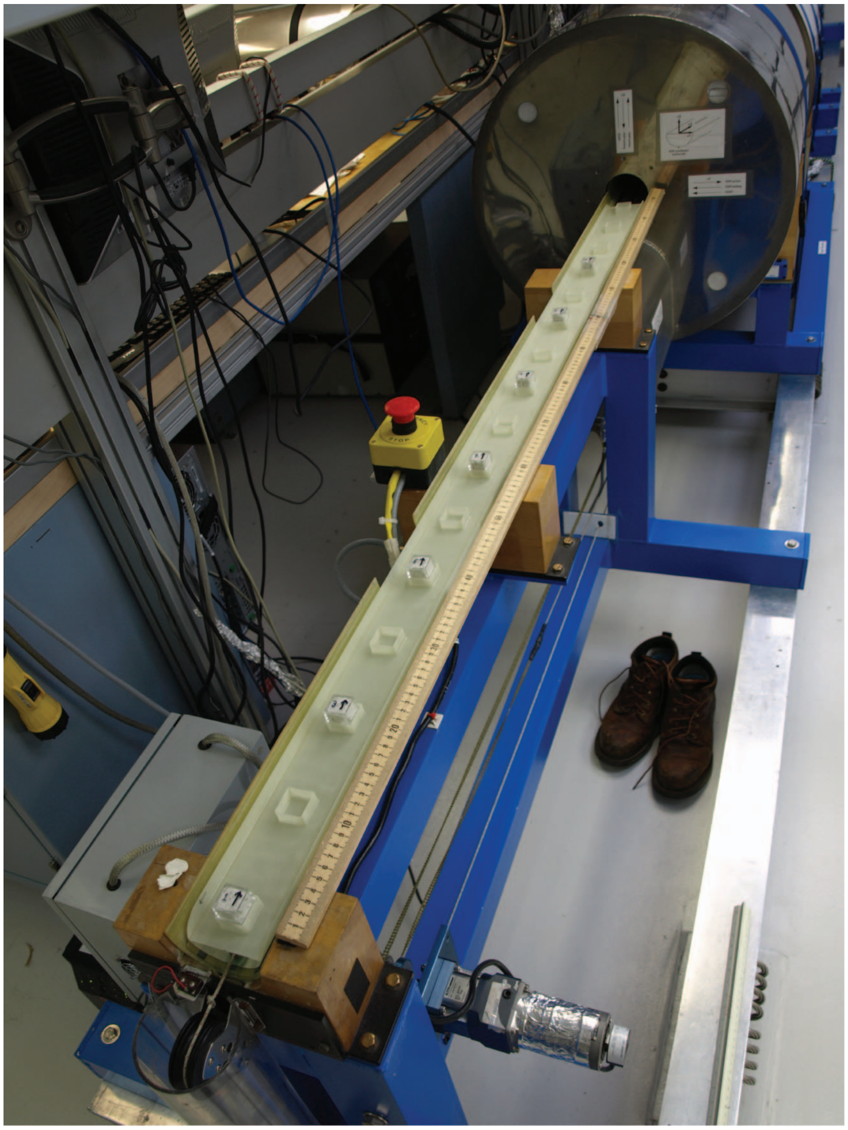

Figure F12. Measurement during Expedition 318 of standard samples placed at positions in the discrete sample tray shown by triangles in right plot. Measurements were made with the core measuring program at 0.5 cm intervals. The discrete sample program makes measurements only at the positions of the triangles and as many as 16 samples can be measured in one run.

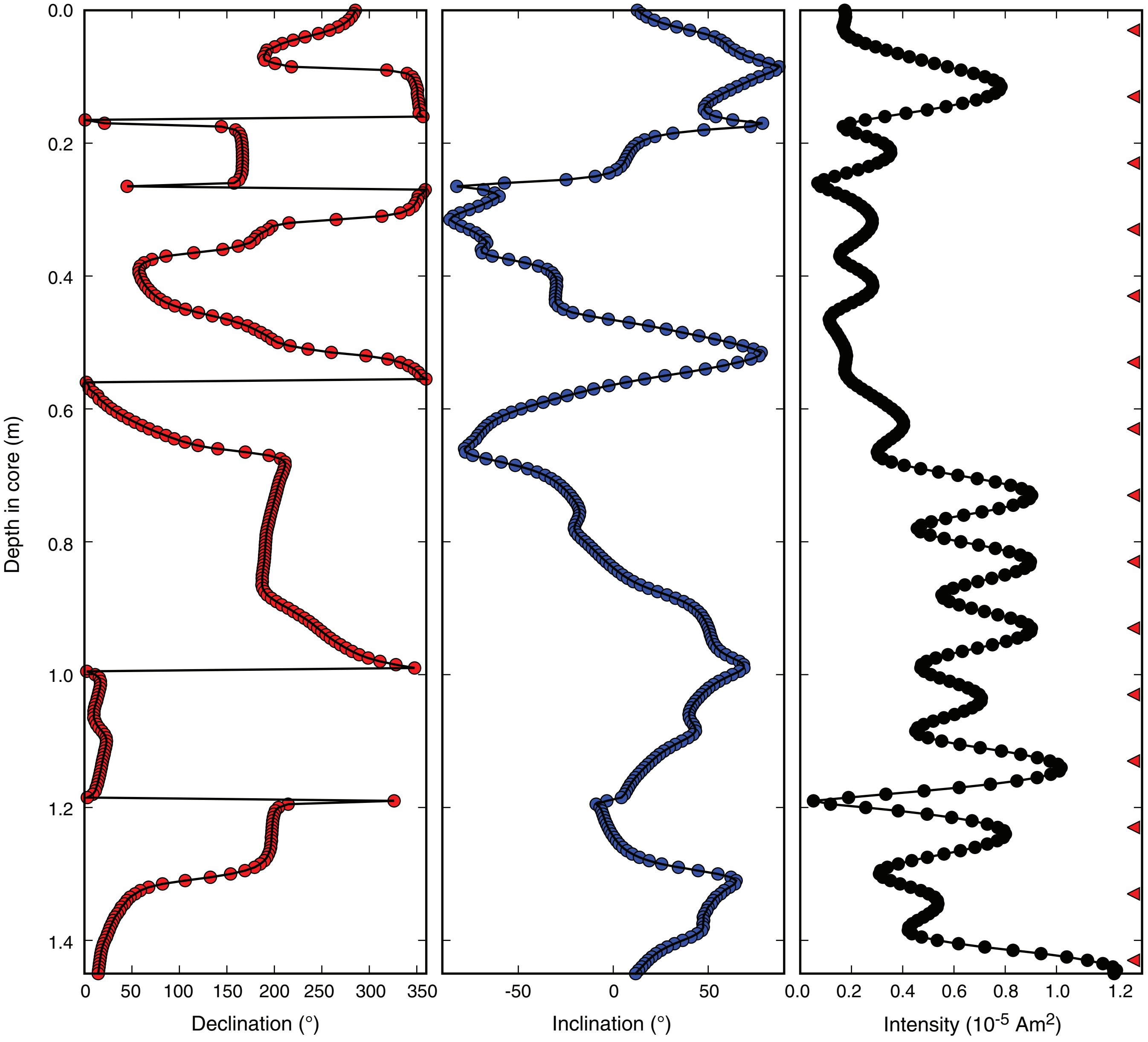

Figure F13. **A.** Data from replicate measurements in 24 positions of standard samples, Expedition 318. **B.** Means and common standard deviations for three measurements (top-toward, top-to-right, and away-up).

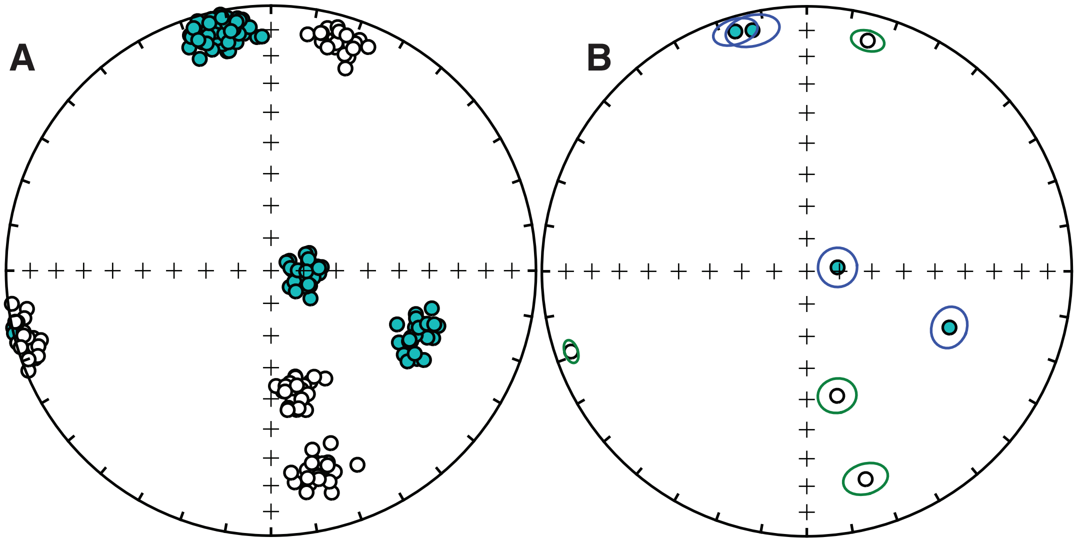

Figure F14. Example of behavior of specimen during AF demagnetization using the (A, B) inline AF demagnetizer and (C, D) Dtech D2000 AF demagnetizer during Expedition 318. **A, C.** Vector endpoint diagram of demagnetization of test specimen after imparting an ARM along the *x*-axis. Demagnetization steps are 0:0, 1:10, 2:20, 3:30, 4:40, 5:60, and 6:80 mT. Circles = projections into the *x*- and *y*-plane, squares = projections into the *x*- and *z*-plane. The specimen had been given an ARM along the *z*-direction. Inset is equal-area projection of directions at each measurement step. Open symbols are in the lower hemisphere; closed are in the lower hemisphere. **B, D.** Decay of remanence during demagnetization. For detailed explanation, see Tauxe (2010).

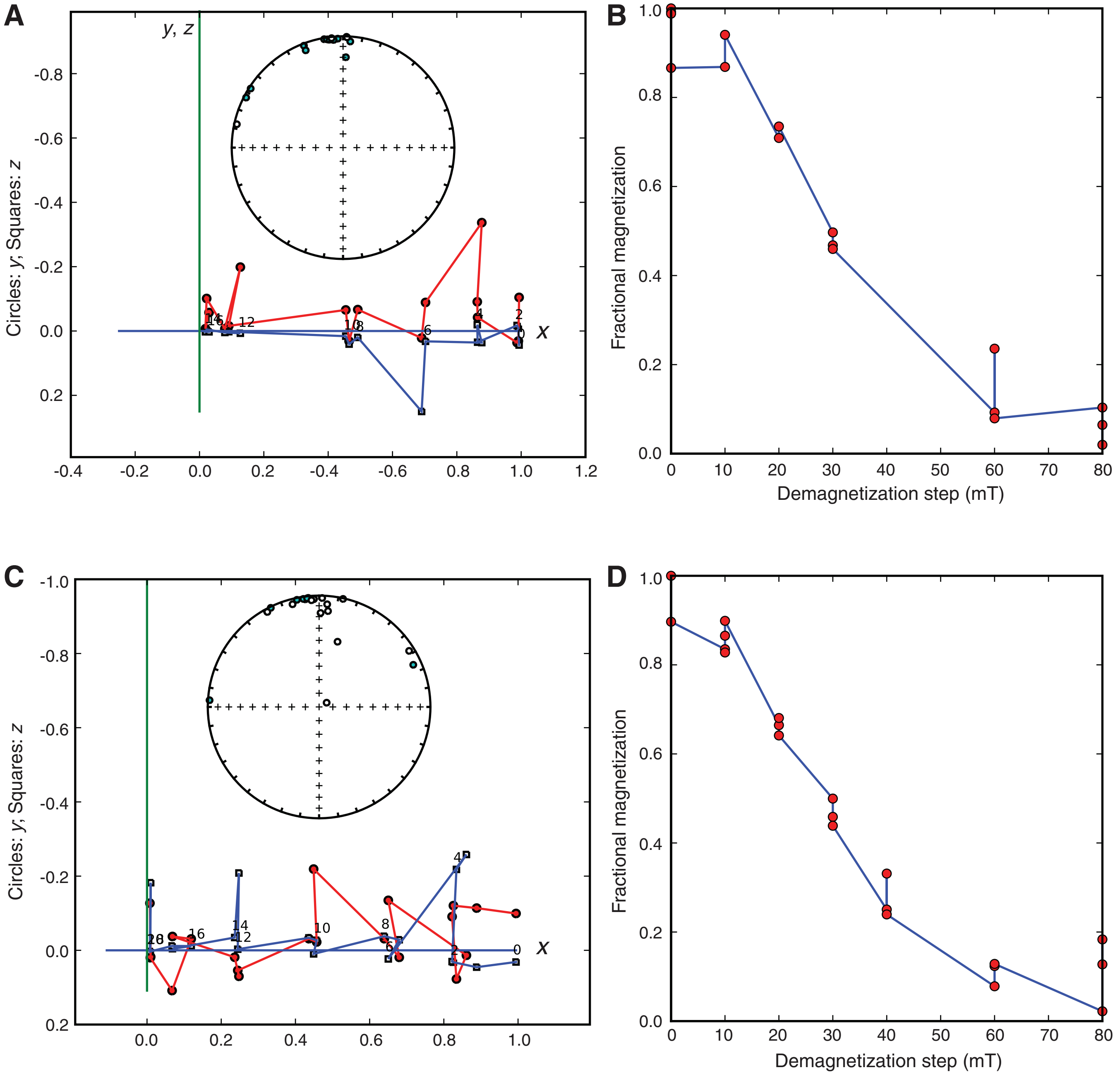

Figure F15. Interpretation of the shape of AMS data. Top balloons illustrate isotropic, oblate, prolate, and triaxial ellipsoids from left to right. **A–D.** Selected data sets plotted as eigenvector directions on equal-area projections from individual samples. Squares = directions associated with maximum eigenvalues, triangles = directions associated with intermediate eigenvalues, circles = directions associated with minimum eigenvalues. **E–H.** Bootstrapped eigenvectors from A–D, respectively. **I–L.** Cumulative distributions of the bootstrapped eigenvalues associated with the eigenvectors plotted in E–H. Bounds containing 95% of each eigenvalue: blue dash-dot lines = minimum eigenvector τ_3, black dashed lines = intermediate τ_2, solid red lines = maximum τ_1. Figure from Tauxe (2010).

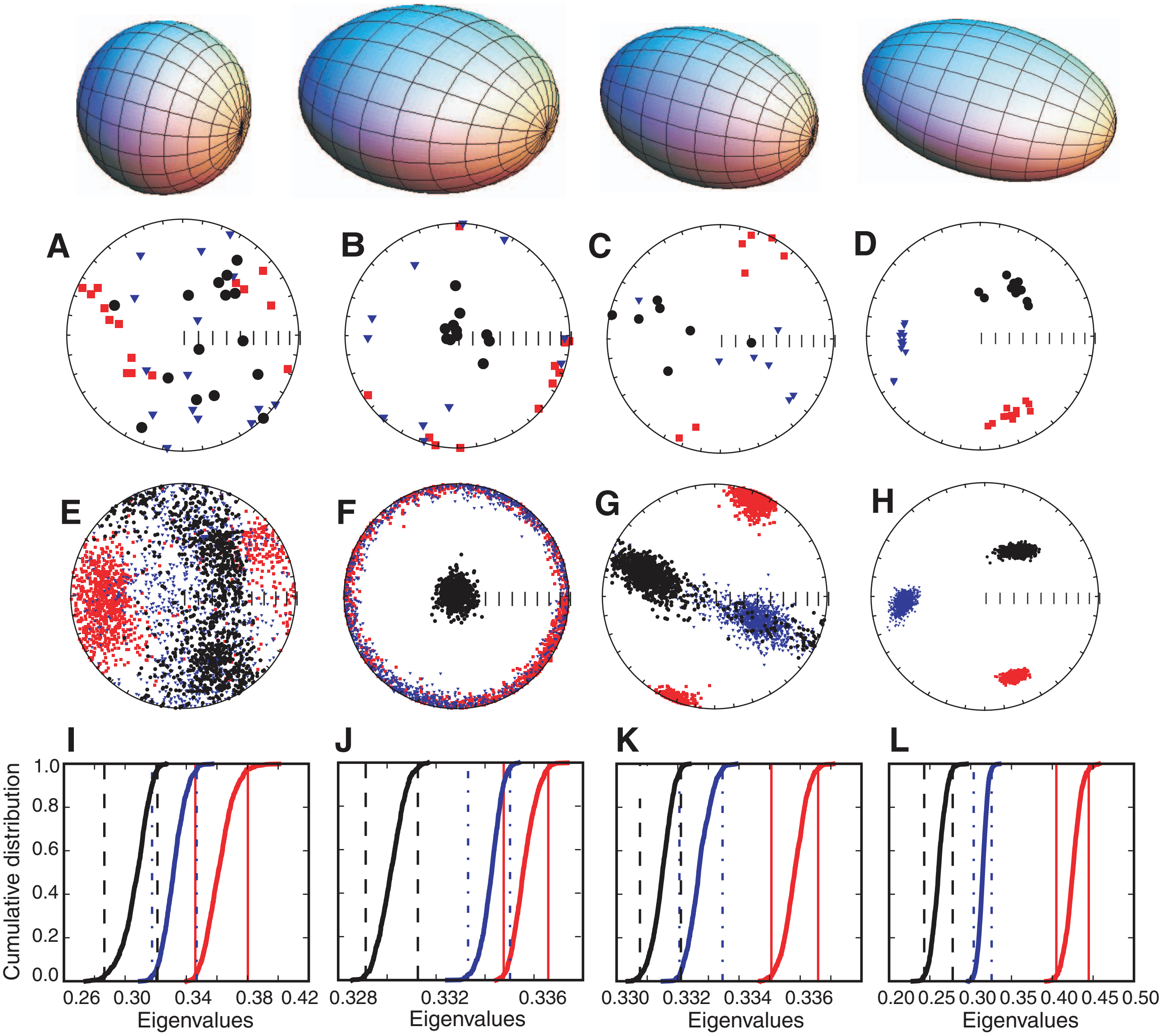

Figure F16. Acquisition of ARM in alternating magnetic field. A total ARM is acquired if the direct current field is switched on throughout the experiment (red dashed line) and a partial ARM is acquired if the field is switched on only for part of the experiment (blue dash-dot line). Figure from Tauxe (2010).

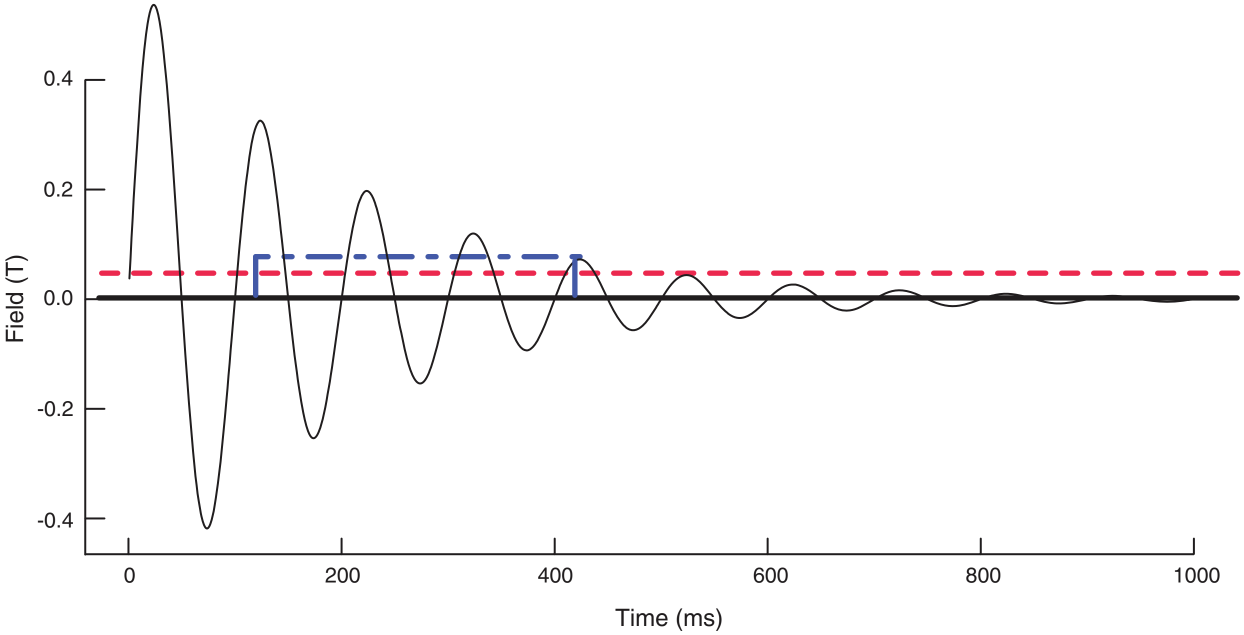

Figure F17. Plot of anhysteretic remanent magnetization (ARM) vs. susceptibility (χ) and how these data are frequently interpreted in terms of changes in grain size and magnetic concentration.

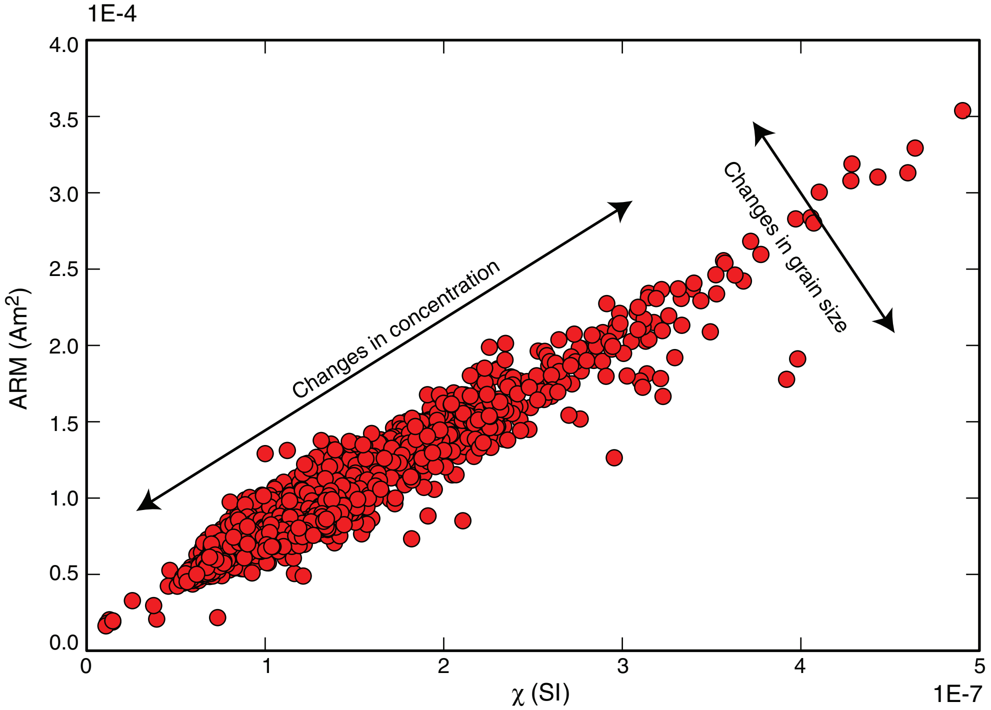

Figure F18. Geomagnetic polarity timescale of Gradstein et al. (2004) used during Expedition 318.

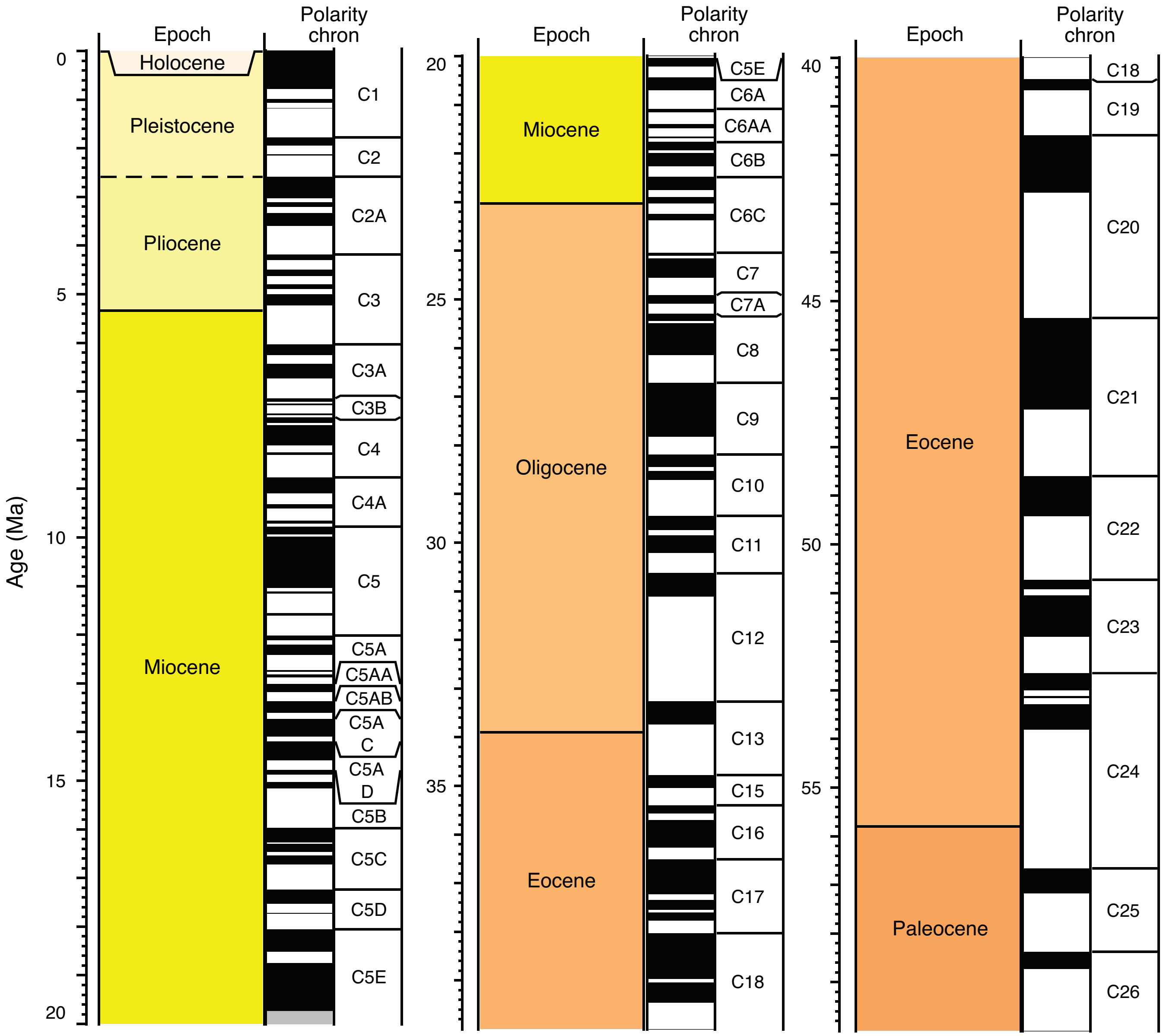

Figure F19. Biomarker protocol for Expedition 318 shipboard analysis. POM = particulate organic matter, TOC = total organic carbon, DCM = dichloromethane, MeOH = methanol, BF_3 = boron trifluoride, FAMES = fatty acid methyl esters, PAHs = polyaromatic hydrocarbons, TMS = trimethylsilyl, GC = gas chromatography, MS = mass spectrometry, C = chromatography, IRMS = infrared mass spectrometry, GDGTs = glycerol dialkyl glycerol tetraether(s), LC = lipid chromatography.

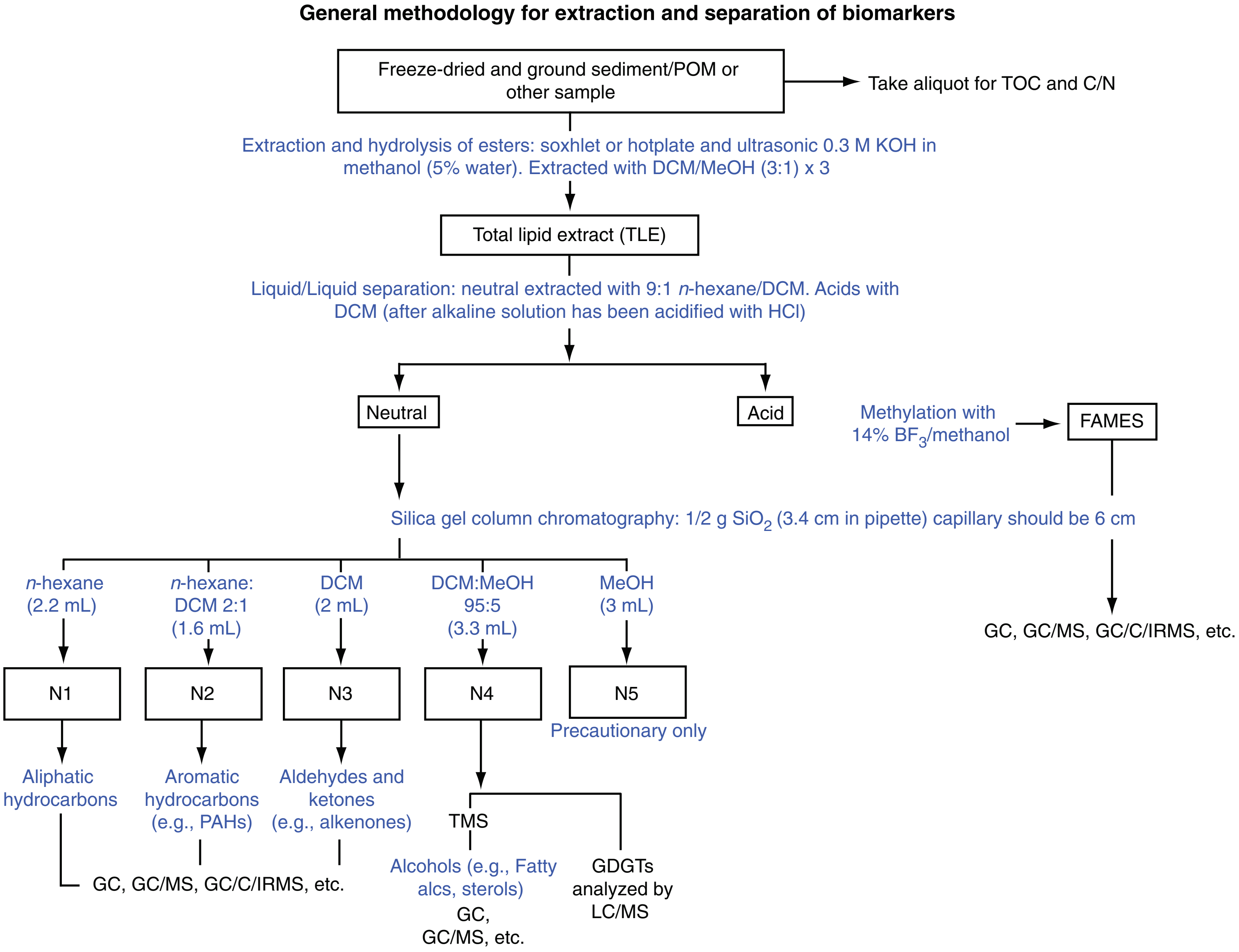

Figure F20. Wireline tool strings used during Expedition 318. See the site chapters for tool strings deployed at each site. HNGS = Hostile Environment Natural Gamma Ray Sonde, APS = Accelerator Porosity Sonde, HLDS = Hostile Environment Litho-Density Sonde, GPIT = General Purpose Inclinometry Tool, DIT = Dual Induction Tool, FMS = Formation MicroScanner, SGT = Scintillation Gamma Ray Tool, VSI = Versatile Sonic Imager.

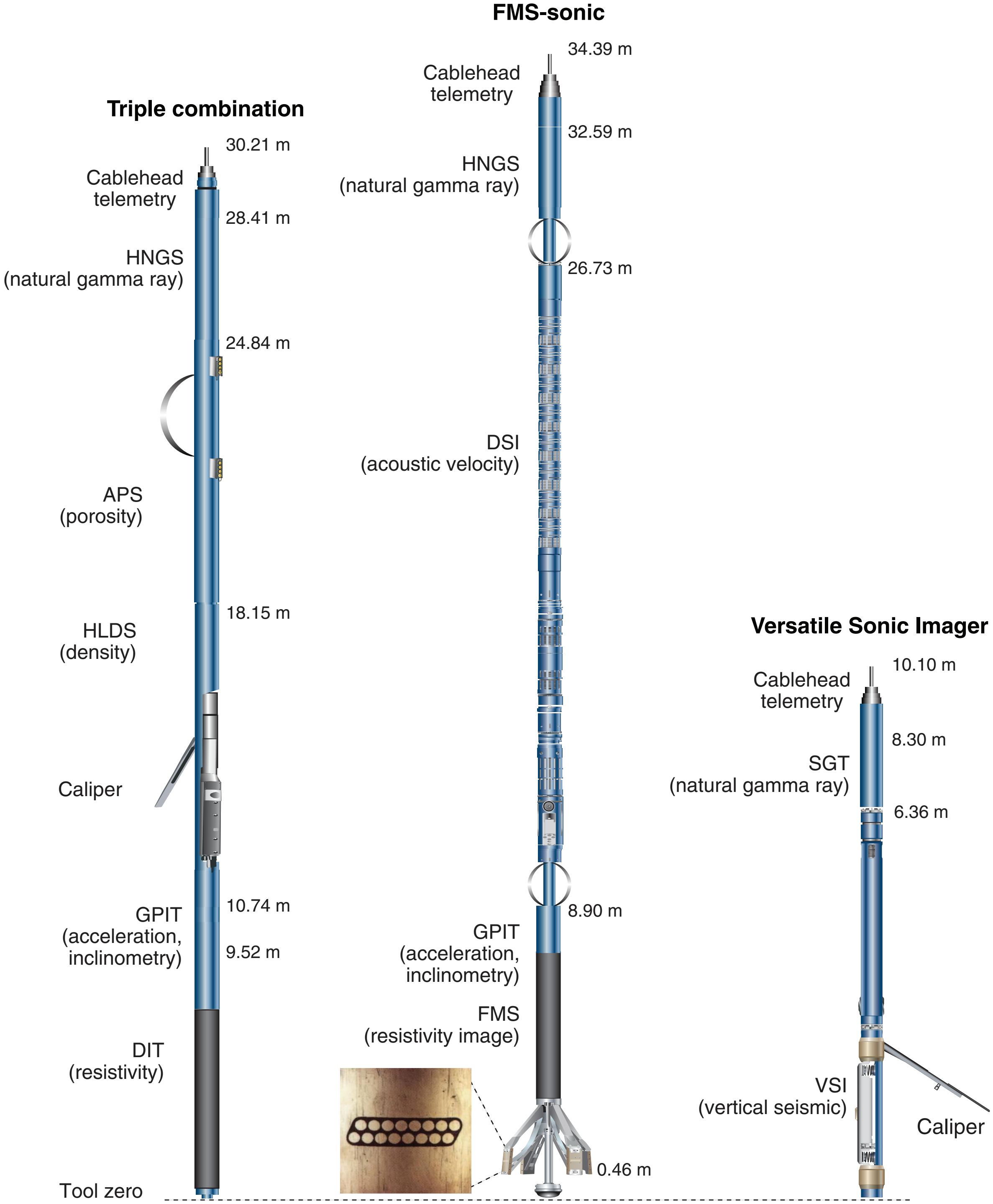

Table T1. IODP depth scale terminology. (**See table notes.**)

Depth scale name	Acronym	Origin	Method description	Submethod	Unit	Previous name	Previous unit
Drillers depth scale							
Drilling depth below rig floor	DRF	Drill floor	Add the lengths of all drill string components deployed beneath the rig floor, from bit to the point on the rig floor where the length of the deployed portion of the last string is measured.	Describe submethod of measuring drill string component length and length deployed at rig floor	m	Depth	mbrf
Drilling depth below seafloor	DSF	Seafloor	Subtract the distance between rig floor and sea level from an estimate of seafloor depth at the drilling depth below rig floor scale using one of the submethods	A. Tag seafloor B. Mudline core C. Visual control D. Inherit depth E. Other	m	Depth	mbsf
Core depth scale							
Core depth below seafloor	CSF	Seafloor	Measure core sample or measurement offset below the core top and add it to the core top's drilling depth below seafloor; apply one of the submethods.	A. Let overlap if long B. Scale if long C. Other	m	Depth	mbsf
Core composite depth	CCSF	Seafloor	Align cores from one hole or multiple adjacent holes based on one of the submethods. The result is a newly constructed depth scale.	A. Append if long B. Scale by factor C. Correlate features D. Splice E. Other	m	Depth	mcd
Wireline depth scale							
Wireline log depth below rig floor	WRF	Drill floor	Measure length of wireline extended beneath the rig floor.	Describe submethod	m	Depth	mbrf
Wireline log depth below seafloor	WSF	Seafloor	Subtract the distance between rig floor and sea level from an estimate of seafloor depth at the wireline depth below rig floor scale using one of three submethods	A. seafloor signal B. Drilling depth C. Inherit depth D. Other	m	Depth	mbsf
Wireline log speed-corrected depth below seafloor	WSSF	Seafloor	Correction for irregular motion of the tool during logging using accelerometer data; used for high-resolution logs such as microresistivity (FMS).	Describe submethod if applicable	m	Depth	mbsf
Wireline log matched depth below seafloor	WMSF	Seafloor	Pick log data from one run as a reference and map other run data using several tie points.	Describe reference log and number/type of tie points used	m	Depth	mbsf

Notes: Drillers depth scale is based on length of drill pipe lowered below the drill floor. Core depth scale is based on the actual length of core recovered and drillers depth, which can vary with time as core expands or contracts. Core depth is technically not a depth but can be used to derive a depth by cumulating all core lengths. Wireline depth scale is based on the wireline length between the downhole tool and shipboard winch. FMS = Formation MicroScanner. See IODP Depth Scale Terminology at **www.iodp.org/program-policies.**

Table T2. Time-calibrated sequences of diatom biostratigraphic events. (See table notes.) (Continued on next three pages.)

		Age (Ma)		
	Event	Average range model	Mid-point	Total range model
	LAD *Rouxia leventerae*	0.07–0.35	0.21	0.06–0.28
	LAD *Hemidiscus karstenii*	0.35–0.43	0.39	0.28–0.33
+	LAD *Rouxia constricta*	0.43–0.5	0.47	0.33–0.39
+	LAD *Actinocyclus ingens*	0.5–0.57	0.54	0.39–0.45
+	LAD *Thalassiosira elliptipora*	0.64–0.71	0.68	0.45–0.5
+	FAD *Thalassiosira antarctica*	0.57–0.64	0.61	0.5–0.56
+	LAD *Thalassiosira fasciculata*	0.89	0.89	0.56–0.61
–	LAD *Fragilariopsis reinholdii*	2.93–2.99	2.96	0.61–0.67
–	LAD *Fragilariopsis fossilis*	2.86–2.92	2.89	0.67–0.72
+	FAD *Navicula directa*	1.02–1.03	1.03	1.03
+	LAD *Actinocyclus* F of Zielinski and Gersonde 2002	1.13–1.29	1.21	1.12–1.14
+	FAD *Rouxia constricta*	1.04–1.23	1.14	1.16–1.21
+	LAD *Fragilariopsis barronii*	1.19–1.29	1.24	1.21–1.28
+	LAD *Shionodiscus tetraoestrupii* var. *reimeri*	1.31–1.34	1.33	1.26–1.43
+	LAD *Rouxia antarctica*	1.48–1.51	1.50	1.26–1.43
	LAD *Thalassiosira inura*	2.53–2.55	2.54	1.35–1.57
	LAD *Fragilariopsis* A Gersonde 1991	1.54–1.67	1.61	1.35–1.78
	LAD *Rouxia naviculoides*	2.28–2.32	2.30	1.4–1.84
	LAD *Proboscia barboi*	1.6–1.73	1.67	1.45–1.81
	FAD *Porosira glacialis*	1.07–1.23	1.15	1.45–1.81
	LAD *Actinocyclus karstenii*	2.13–2.16	2.15	1.59–1.87
–	LAD *Thalassiosira nativa*	4.73–4.79	4.76	1.4–1.97
	FAD *Fragilariopsis separanda*	1.37–1.45	1.41	1.64–1.89
	FAD *Fragilariopsis rhombica*	1.37–1.45	1.41	1.69–1.92
	LAD *Thalassiosira striata*	2.89–2.96	2.93	1.78–1.95
+	LAD *Thalassiosira kolbei*	1.98–1.98	1.98	1.97–1.99
+	LAD *Fragilariopsis matuyamae*	2–2.06	2.03	1.99–2.01
+	LAD *Fragilariopsis matuyamae* var. *heteropola*	2.08–2.11	2.10	2.02–2.06
+	LAD *Actinocyclus fasciculatus*	2.05–2.27	2.16	2.02–2.1
	LAD *Thalassiosira lentiginosa* var. *obovatus*	2.1–2.13	2.12	2.04–2.08
+	LAD *Thalassiosira torokina*	2.2–2.27	2.24	2.06–2.1
+	LAD *Thalassiosira vulnifica*	2.15–2.19	2.17	2.1–2.12
+	LAD *Fragilariopsis interfrigidaria*	2.4–2.45	2.43	2.12–2.14
	FAD *Shionodiscus gracilis*	1.87	1.87	2.15–2.16
+	FAD *Fragilariopsis matuyamae* var. *heteropola*	2.2–2.29	2.25	2.17–2.18
+	LAD *Thalassiosira insigna*	2.45–2.5	2.48	2.19–2.2
+	LAD *Actinocyclus maccollumii*	2.4–2.45	2.43	2.21–2.22
	LAD *Stephanopyxis turris*	2.96–3.08	3.02	2.23–2.24
+	LAD *Fragilariopsis weaveri*	2.45–2.53	2.49	2.25–2.27
+	FAD *Fragilariopsis kerguelensis*	2.18–2.21	2.20	2.28–2.29
+	LAD *Thalassiosira webbi*	2.65–2.77	2.71	2.3–2.31
+	LAD *Rouxia diploneides*	2.55–2.69	2.62	2.32–2.33
+	LAD *Thalassiosira jacksonii*	3.67–3.85	3.76	2.34–2.37
–	LAD *Fragilariopsis clementia*	4.51–4.6	4.56	2.34–2.37
+	FAD *Asteromphalus hyalinus*	1.54–1.62	1.58	2.38–2.39
+	LAD *Thalassiosira complicata*	3.36–3.44	3.40	2.41–2.41
	LAD *Fragilariopsis praeinterfrigidaria*	3.45–3.49	3.47	2.43–2.43
+	LAD *Alveus marinus*	3–3.33	3.17	2.45–2.48
	LAD *Rouxia californica*	4.29–4.82	4.56	2.47–2.5
	FAD *Porosira pseudodenticulata*	2.25–2.32	2.29	2.45–2.52
+	LAD *Rouxia heteropolara*	3.42–3.47	3.45	2.49–2.52
	FAD *Rouxia leventerae*	2–2.08	2.04	2.54–2.54
	LAD *Thalassiosira convexa*	2.58–2.81	2.70	2.56–2.56
+	FAD *Shionodiscus tetraoestrupii* var. *reimeri*	2.35–2.37	2.36	2.61–2.63
+	FAD *Fragilariopsis matuyamae*	2.38–2.4	2.39	2.63–2.66
+	LAD *Navicula wisei*	3.73–3.94	3.84	2.66–2.69
+	FAD *Actinocyclus* F of Zielinski and Gersonde 2002	2.33–2.34	2.34	2.69–2.71
	LAD *Fragilariopsis praecurta*	4.19–4.28	4.24	2.74
+	LAD *Actinocyclus octonarius* var. *asteriscus*	3.99–4.26	4.13	2.77–2.79
+	FAD *Actinocyclus fasciculatus*	2.65–2.77	2.71	2.77–2.79
	LAD *Fragilariopsis aurica*	4.21–4.35	4.28	2.82
	FAD *Actinocyclus actinochilus*	2.72–2.81	2.77	2.84
+	FAD *Actinocyclus maccollumii*	2.79–2.84	2.82	2.87
+	LAD *Fragilariopsis lacrima*	3.99–4.26	4.13	2.9
+	LAD *Fragilariopsis arcula*	4.29–4.49	4.39	2.92–2.95
+	FAD *Asteromphalus hookeri*	2.45–2.53	2.49	2.92–2.98

Table T2 (continued). (Continued on next page.)

		Age (Ma)		
	Event	Average range model	Mid-point	Total range model
	FAD *Thalassiosira elliptipora*	2–2.06	2.03	2.95–2.98
	LAD *Thalassiosira oliverana* var. *sparsa*	4.79–4.9	4.85	3
	LAD *Denticulopsis simonsenii*	4.83–4.95	4.89	3.36
	FAD *Fragilariopsis obliquecostata*	1.66–1.73	1.70	3.38–3.41
	FAD *Fragilariopsis ritscheri*	2.82–2.88	2.85	3.41–3.44
+	FAD *Thalassiosira lentiginosa* var. *obovatus*	3.33–3.41	3.37	3.44–3.47
	FAD *Fragilariopsis ritscheri* A	3.48–3.52	3.50	3.47–3.49
	FAD *Thalassiosira webbi*	3.17–3.44	3.31	3.38–3.57
+	FAD *Thalassiosira vulnifica*	3.12–3.18	3.15	3.49–3.52
+	FAD *Thalassiosira insigna*	3.14–3.36	3.25	3.52–3.55
+	FAD *Fragilariopsis weaveri*	3.51–3.55	3.53	3.55–3.57
	FAD *Fragilariopsis curta*	3.54–3.57	3.56	4.2–4.2
	FAD *Fragilariopsis* A Gersonde 1991	3.57–4.42	4.00	4.21–4.22
+	FAD *Chaetoceras bulbosum*	3.6–3.77	3.69	4.21–4.23
	LAD *Thalassiothrix miocenica*	4.54–4.8	4.67	4.22–4.23
+	FAD *Thalassiosira lentiginosa*	3.86–4.11	3.99	4.24–4.25
+	LAD *Hemidiscus karstenii* f1	4.74–5.12	4.93	4.25–4.28
+	LAD *Rouxia peragalli*	4.58–4.75	4.67	4.25–4.28
+	FAD *Fragilariopsis interfrigidaria*	3.93–4.19	4.06	4.27–4.29
+	LAD *Rhizosolenia costata*	4.2–4.3	4.25	4.28–4.3
	FAD *Navicula wisei*	4.56–4.7	4.63	4.25–4.69
	FAD *Thalassiosira fasciculata*	4.25–4.42	4.34	4.3–4.69
	FAD *Fragilariopsis barronii*	4.28–4.52	4.40	4.43–4.72
	FAD *Thalassiosira kolbei*	3.8–4.02	3.91	4.43–4.72
	FAD *Azpeitia nodulifer*	4.56–4.71	4.64	4.68–4.74
+	FAD *Thalassiosira striata*	4.3–4.64	4.47	4.7–4.78
	FAD *Thalassiosira tumida*	4.23–4.37	4.30	4.73–4.8
+	FAD *Azpeitia tabularis* var. *egregius*	4.3–4.57	4.44	4.7–4.82
+	FAD *Thalassiosira lineata*	4.66–4.72	4.69	4.78–4.83
+	FAD *Rhizosolenia costata*	4.58–4.74	4.66	4.78–4.83
+	FAD *Rouxia diploneides*	4.61–4.7	4.66	4.83–4.84
+	FAD *Thalassiosira complicata*	4.64–4.71	4.68	4.84–4.86
–	FAD *Actinocyclus octonarius* var. *asteriscus*	4.24–4.4	4.32	4.86–4.87
	FAD *Rouxia antarctica*	4.43–4.57	4.50	4.87–4.88
	LAD *Fragilariopsis donahuensis*	5.1–6.86	5.98	4.89–4.89
+	FAD *Thalassiosira inura*	4.71–4.77	4.74	4.92
+	LAD *Actinocyclus ingens* var. *ovalis*	4.75–6.81	5.78	4.94
+	FAD *Fragilariopsis praeinterfrigidaria*	4.72–4.78	4.75	4.96
+	FAD *Fragilariopsis lacrima*	4.69–4.74	4.72	4.98
	LAD *Thalassiosira praeconvexa*	6.1–6.92	6.51	5.04
+	LAD *Nitzschia miocenica*	5–5.24	5.12	5.08
	LAD *Hemidiscus triangularus*	5.14–6.86	6.00	5.12
–	LAD *Fragilariopsis januaria*	8.7–8.77	8.74	5.16
+	LAD *Neobrunia mirabilis*	6.25–6.97	6.61	5.2
	LAD *Asteromphalus kennettii*	6.61–8.21	7.41	5.5
	LAD *Actinocyclus ellipticus*	5.14–7.78	6.46	5.77
	FAD *Shionodiscus oestrupii*	4.8–4.95	4.88	6.05–6.13
	LAD *Thalassiosira miocenica*	4.9–6.92	5.91	6.08–6.23
	FAD *Rouxia heteropolara*	4.68–4.73	4.71	6.1–6.33
–	LAD *Fragilariopsis pusilla*	15.33–15.34	15.34	6.13–6.91
–	FAD *Thalassiosira convexa*	5.19–6.64	5.92	6.13–6.91
–	FAD *Thalassiosira jacksonii*	4.78–4.86	4.82	6.18–8.21
–	FAD *Thalassiosira praeconvexa*	6.31–7.03	6.67	6.2–8.41
–	LAD *Denticulopsis crassa*	7.92–8.33	8.13	7.53–8.3
–	LAD *Lithodesmium minisculum*	8.5–8.74	8.62	6.2–8.59
	LAD *Denticulopsis ovata*	8.57–10.71	9.64	8.11–8.34
	LAD *Denticulopsis dimorpha*	9.78–10.77	10.28	8.24–8.41
+	FAD *Thalassiosira miocenica*	6.25–8.33	7.29	8.34–8.44
	FAD *Nitzschia miocenica*	8.5–8.61	8.56	8.39–8.48
+	LAAD *Denticulopsis simonsenii*	8.57–8.68	8.63	8.43–8.52
	FAD *Alveus marinus*	8.4–8.61	8.51	8.47–8.55
	FAD *Fragilariopsis reinholdii*	8.43–8.52	8.48	8.51–8.59
+	FAD *Thalassiosira oliverana* var. *sparsa*	8.47–8.58	8.53	8.6–8.63
–	LAD *Asteromphalus oligocenicus*	12.07	12.07	8.64–8.66
	LAD *Fragilariopsis claviceps*	9.67–10.84	10.26	8.68–8.73
+	FAD *Fragilariopsis arcula*	8.4–8.49	8.45	8.68–8.73
	FAD *Fragilariopsis fossilis*	8.37–8.43	8.40	8.84–8.88
	FAD *Hemidiscus triangularus*	6.41–7.08	6.75	8.9–9.15

Table T2 (continued). (Continued on next page.)

		Age (Ma)		
	Event	Average range model	Mid-point	Total range model
–	FAD *Thalassiosira eccentrica*	6.41–7.94	7.18	8.9–9.15
	FAD *Hemidiscus karstenii* f1	6.96–8.39	7.68	8.97–9.26
	FAD *Actinocyclus ingens ovalis*	8.6–8.74	8.67	9.1–9.26
+	FAD *Thalassiosira torokina*	6.43–8.03	7.23	9.36
–	FAD *Thalassiosira oliverana*	5.14–7.21	6.18	9.73
	LAD *Denticulopsis dimorpha* var. *areolata*	9.72–10.77	10.25	9.73
–	LAD *Denticulopsis lauta*	12.46–13.73	13.10	9.74
+	FAD *Rouxia californica*	8.5–8.74	8.62	9.74
–	FAD *Fragilariopsis clementia*	6.35–7.7	7.03	9.75
+	FAD *Lithodesmium minisculum*	9.69–10.38	10.04	9.76–9.76
	FAD *Fragilariopsis aurica*	8.3–8.39	8.35	9.76–9.77
	FAD *Thalassiosira nativa*	9.68–10.18	9.93	9.76–9.77
	FAD *Hemidiscus karstenii*	9.68–10.24	9.96	9.77
	FAD *Asteromphalus kennettii*	9.7–10.71	10.21	9.94–10.03
	FAD *Denticulopsis crassa*	9.7–10.51	10.11	10.1–10.28
	FAD *Hemidiscus cuneiformis*	10.24–10.91	10.58	10.25–10.54
	LAAD *Denticulopsis dimorpha*	10.58–10.97	10.40	10.41–11.04
–	FAD *Actinocyclus ellipticus*	9.71–11.08	10.78	10.41–11.32
	LAD *Denticulopsis praedimorpha*	11.44	11.44	10.73–11.41
	FAD *Actinocyclus karstenii*	9.67–10.05	10.14	10.88–11.49
–	FAD *Thalassiothrix miocenica*	9.7–10.58	9.86	10.73–11.84
	LAD *Nitzschia denticuloides*	11.72	11.72	11.15–11.58
	FAD *Fragilariopsis praecurta*	8.77–10.11	9.44	11.29–11.67
	FAD *Denticulopsis dimorpha* var. *areolata*	9.78–10.84	10.31	11.44–11.84
	FAD *Eucampia antarctica*	10.01–10.91	10.46	11.44–11.84
	LAD *Actinocyclus ingens nodus*	12.52–12.6	12.56	11.87–11.92
+	LAD *Crucidenticula nicobarica*	12.57–12.67	12.62	12.14–12.26
+	LAD *Nitzschia grossepunctata*	12.73–13.25	12.99	12.17–12.31
	FAD *Denticulopsis ovata*	11.08–11.1	11.09	12.19–12.36
	FAD *Denticulopsis dimorpha*	12.46–12.54	12.50	12.52
+	FAD *Fragilariopsis claviceps*	12.62–12.73	12.68	12.62
	FAD *Denticulopsis praedimorpha*	12.81–13.13	12.97	12.81
–	FAD *Fragilariopsis donahuensis*	10.81–11.08	10.95	13.64–13.67
–	LAD *Denticulopsis hyalina*	13.13–13.52	13.33	13.69–14.24
	LAD *Denticulopsis maccollumii*	14.29–14.36	14.33	14.11–14.3
	LAD *Cavitatus jouseanus*	14.39–14.54	14.47	14.13–14.4
	FAD *Denticulopsis simonsenii*	14.15–14.16	14.16	14.14–14.46
–	FAD *Fragilariopsis januaria*	10.7–11.08	10.89	14.13–14.56
	FAD *Nitzschia denticuloides*	13.37–13.6	13.49	14.15–14.51
	FAD *Denticulopsis hyalina*	13.45–14.13	13.79	14.16–14.56
	LAD *Araniscus lewisianus*	14.68–15.1	14.89	14.31–14.61
	FAD *Actinocyclus ingens* var. *nodus*	14.49–14.71	14.60	14.42–14.67
	LAD *Nitzschia* 17 Schrader	15.5–15.52	15.51	14.54–14.72
	LAD *Cavitatus miocenicus*	14.58–14.98	14.78	14.65–14.77
+	LAD *Crucidenticula kanayae*	16.18–16.61	16.40	14.77–14.83
+	LAD *Raphidodiscus marylandicus*	16.18–16.61	16.40	15.07–15.12
	LAD *Coscinodiscus rhombicus*	16.35–17.88	17.12	15.07–15.12
	LAD *Fragilariopsis maleinterpretaria*	16.52–16.97	16.75	15.37
	FAD *Denticulopsis lauta*	15.67–15.7	15.69	15.57
	FAD *Actinocyclus ingens*	15.84–15.89	15.87	15.78
	FAD *Nitzschia grossepunctata*	16.01–16.07	16.04	15.99
	FAD *Nitzschia* sp. 17 Schrader	16.35–17.15	16.75	16.2
	FAD *Denticulopsis maccollumii*	16.87–17.15	17.01	16.4
	FAD *Neobrunia mirabilis*	16.7–17.34	17.02	16.61
	LAD *Thalassiosira praefraga*	17.38–17.88	17.63	16.82
–	FAD *Rouxia naviculoides*	7.53–8.39	7.96	17.02
	FAD *Araniscus lewisianus*	17.21–17.88	17.55	17.23
–	FAD *Crucidenticula nicobarica*	14.58–15.1	14.84	17.44
	FAD *Crucidenticula kanayae*	17.38–17.88	17.63	17.65
–	FAD *Rouxia peragalli*	6.38–7.61	7.00	17.85
	FAD *Fragilariopsis pusilla*	18.32–18.5	18.41	18.27
–	FAD *Proboscia barboi*	13–13.37	13.19	18.47
	FAD *Raphidodiscus marylandicus*	18.5–18.68	18.59	18.68
	FAD *Azpeitia tabularis*	18.06–18.32	18.19	18.89
	FAD *Thalassiosira praefraga*	18.68–18.85	18.77	19.1–19.3
	FAD *Fragilariopsis maleinterpretaria*	18.85–19.03	18.94	19.1–19.3
–	FAD *Stephanopyxis turris*	9.66–9.98	9.82	19.51–19.72
	FAD *Cavitatus miocenicus*	19.03–19.38	19.21	19.51–20.13

Table T2 (continued).

	Event	Age (Ma)		
		Average range model	Mid-point	Total range model
	FAD *Actinocyclus octonarius*	17.89–19.2	18.55	19.72–19.92
	FAD *Coscinodiscus rhombicus*	19.2–19.38	19.29	19.92–20.13
	FAD *Asteromphalus oligocenicus*	19.55	19.55	20.34
+	FAD *Cavitatus jouseanus*	19.73	19.73	20.55

Notes: Generated by the total range and average range models of Cody et al. (2008). Ranges are plotted in Figure F6. FAD = first appearance datum, LAD = last appearance datum. LAAD = last abundant appearance datum. + = events used as primary biostratigraphic markers in Cody et al. (2008), – = events unsuitable for biostratigraphy (Cody et al., 2008). As a first-stage attempt to resolve the best-fit sedimentation rate for all sites, an age was assigned for the stratigraphic first occurrence and last occurrence of diatom events using the mid-point age value of the FADs and LADs of the average range model by Cody et al. (2008).

Table T3. Stratigraphic ranges for selected Cenozoic dinocyst species. This table is available in an oversized format.

Table T4. Cenozoic dinocyst literature. (See table note.) (Continued on next page.)

Reference number	Reference	Geography	Realm	Calibration
1	Below, 1981	Germany	Boreal	BIOSTRAT
2	Davey and Verdier, 1971	France	Boreal	BIOSTRAT
3	Davey and Verdier, 1973	France	Boreal/Tethys	BIOSTRAT
4	Davey and Verdier, 1974	France	Boreal/Tethys	BIOSTRAT
5	Davey, 1979	England	Boreal	BIOSTRAT
6	Duxbury, 1977	Speeton	Boreal	BIOSTRAT
7	Duxbury, 1980	Speeton	Boreal	BIOSTRAT
8	Duxbury, 1983	Isle of Wight	Boreal	BIOSTRAT
9	Head et al., 1989c	Labrador Sea	High latitude NH	EXTRAP/BIOSTRAT
10	Foucher, 1979	Paris Basin	Boreal	BIOSTRAT
11	Habib and Drugg, 1983	France/Switzerland	Tethys	BIOSTRAT
12	De Gracianski et al., 1998	Europe	Boreal/Tethys	BIOSTRAT
13	Harding, 1990	Germany/England	Boreal	BIOSTRAT
14	Hoedemaeker and Leereveld, 1995	Southeast Spain	Tethys	BIOSTRAT
15	Hoek et al., 1996	Israel	Tethys	BIOSTRAT
16	Jarvis et al., 1988	England	Boreal	BIOSTRAT
17	Kirsch, 1991	South Germany	Boreal	BIOSTRAT
18	Leereveld, 1995	South Spain	Tethys	BIOSTRAT
19	Londeix, 1990	South France	Tethys	BIOSTRAT
20	Roncaglia et al., 1999	New Zealand	Mid latitude SH	BIOSTRAT
21	Monteil, 1985	South France	Tethys	BIOSTRAT
22	Monteil, 1992	South France	Tethys	BIOSTRAT
23	Pearce, 2000	England	Boreal	BIOSTRAT
24	Powell, 1992	United Kingdom	Boreal	BIOSTRAT
25	Prince et al., 1999	Isle of Wight	Boreal	BIOSTRAT
26	Prössl, 1990	North Germany	Boreal	BIOSTRAT
27	Robaszynski et al., 1982	Belgium	Boreal	BIOSTRAT
28	Brinkhuis and Schiøler, 1996	Northwest Europe	Boreal	BIOSTRAT
29	Schiøler and Wilson, 1993	Denmark	Boreal	BIOSTRAT
30	Tocher and Jarvis, 1987	South England	Boreal	BIOSTRAT
31	Verdier, 1975	North France	Boreal	BIOSTRAT
32	Wilpshaar, 1995	South France	Tethys	BIOSTRAT
33	Wilson, 1974	Northwest Europe	Boreal	BIOSTRAT
34	Utrecht/Williams/Pearce	Global	Global	BIOSTRAT
35	Williams et al., 1993	Global	Global	EXTRAPOLATED
36	deVerteuil and Norris, 1996a	Northwest Atlantic	Mid latitude NH	EXTRAP/BIOSTRAT
37	Powell et al., 1996	Northwest Europe	Mid latitude NH	MAGNETOSTRAT
38	Zevenboom, 1995	South Europe	Low latitude NH	MAGNETO/BIOSTRAT
39	Bujak et al., 1980	Northwest Europe	Mid latitude NH	BIOSTRAT
40	Bujak and Mudge, 1994	Northwest Europe	Mid latitude NH	EXTRAPOLATED
41	Mudge and Bujak, 1996	Northwest Europe	Mid latitude NH	EXTRAPOLATED
42	Heilmann-Clausen, 1985	Northwest Europe	Mid latitude NH	BIOSTRAT
43	Köthe, 1990	Northwest Europe	Mid latitude NH	EXTRAP/BIOSTRAT

Table T4 (continued).

Reference number	Reference	Geography	Realm	Calibration
44	Wilson, 1988	New Zealand	Mid latitude SH	EXTRAP/BIOSTRAT
45	Stover and Hardenbol, 1994	Northwest Europe	Mid latitude NH	BIOSTRAT
46	McMinn, 1992	Australia, ODP123	Low latitude SH	BIOSTRAT
47	Heilmann-Clausen and Costa, 1989	Northwest Europe	Mid latitude NH	BIOSTRAT
48	Brinkhuis and Biffi, 1993	Italy	Low latitude NH	MAGNETOSTRAT
49	Wrenn and Hart, 1988	Antarctica	High latitude SH	MAGNETO/BIOSTRAT
50	Brinkhuis et al., 1998	Africa, Northwest Europe	Low–mid latitude NH	BIOSTRAT
51	Helby et al., 1987	Australia	Low–mid latitude SH	BIOSTRAT
52	Brinkhuis and Leereveld, 1988	North Africa	Low latitude NH	BIOSTRAT
53	Brinkhuis and Zachariasse, 1988	North Africa	Low latitude NH	BIOSTRAT
54	Raine et al., 1997	New Zealand	Mid latitude SH	EXTRAP/BIOSTRAT
55	Wilpshaar et al., 1996	Italy	Low latitude NH	MAGNETOSTRAT
56	Stover and Williams, 1995	Global	Global	EXTRAP/BIOSTRAT
57	Brinkhuis et al., 1992	Italy	Low latitude NH	MAGNETOSTRAT
58	Brinkhuis et al., 2003a	Offshore Tasmasia	Low–mid latitude SH	MAGNETO/BIOSTRAT
59	Brinkhuis et al., 2003b	Offshore Tasmasia	High latitude SH	MAGNETO/BIOSTRAT
60	Pearce et al., 2003	England	Boreal	BIOSTRAT
61	Prince, 1997	England	Boreal	BIOSTRAT
62	Eldrett et al., 2004	North Atlantic	High latitude NH	MAGNETO/BIOSTRAT
63	Van Simaeys et al., 2005	Belgium, Germany	Low latitude NH	MAGNETO/BIOSTRAT
64	Munsterman and Brinkhuis, 2005	Netherlands	Mid latitude NH	SEQ STRAT/BIOSTRAT
65	Kuhlmann et al., 2006	Netherlands	Mid latitude NH	MAGNETO/BIOSTRAT
66	Williams et al., 1993	North Atlantic	Mid latitude NH	BIOSTRAT
67	Sluijs and Brinkhuis, 2009	Global	Global	MAGNETO/BIOSTRAT
68	Torricelli, 2006	Spain	Low latitude NH	BIOSTRAT
69	Louwye et al., 2004	North Atlantic, Belgium	Mid latitude NH	BIOSTRAT
70	Head, 1993	England	Mid latitude NH	BIOSTRAT
71	Head and Norris, 2003	Western North Atlantic	Mid latitude NH	MAGNETO/BIOSTRAT
72	Versteegh and Zevenboom, 1995	North Atlantic and Italy	Low–mid latitude NH	MAGNETO/BIOSTRAT
73	Versteegh, 1997	North Atlantic and Italy	Low–mid latitude NH	MAGNETO/BIOSTRAT
74	Head, 2000	Northwest Europe and North Atlantic	Mid latitude NH	MAGNETO/BIOSTRAT
75	Head, 1998	Northwest Europe and North Atlantic	Mid–high latitude NH	MAGNETO/BIOSTRAT
76	Londeix and Jan du Chêne, 1998	France	Mid latitude NH	EXTRAP/BIOSTRAT
77	Pross et al., 2010	Central Italy	Low Latitude NH	MAGNETOSTRAT
78	Houben et al., submitted	Kerguelen Plateau	High Latitude SH	EXTRAP/BIOSTRAT
79	De Schepper and Head, 2008	North Atlantic	Mid latitude NH	MAGNETO/BIOSTRAT
80	Louwye and Mertens, 2008	North Atlantic	Mid latitude NH	MAGNETOSTRAT
81	Bijl et al., in press	Southwest Pacific	High latitude SH	MAGNETO/BIOSTRAT
82	Hollis et al., 2009	South Pacific	Mid latitude SH	BIOSTRAT

Note: NH = Northern Hemisphere, SH = Southern Hemisphere.

Table T5. Geomagnetic polarity timescale used for Expedition 318. (See table note.) (Continued on next page.)

Chron	Age (Ma) Young	Age (Ma) Old	Alternate chron names	Subchrons
C1n	0.000	0.781	Brunhes	
C1r.1r	0.781	0.988	Matuyama	
C1r.1n	0.988	1.072		Jaramillo
C1r.2r	1.072	1.173		
C1r.2n	1.173	1.185		Cobb Mountain
C1r.3r	1.185	1.778		
C2n	1.778	1.945		Olduvai
C2r.1r	1.945	2.128		
C2r.1n	2.128	2.148		Reunion
C2r.2r	2.148	2.581		
C2An.1n	2.581	3.032	Gauss	
C2An.1r	3.032	3.116		Kaena
C2An.2n	3.116	3.207		
C2An.2r	3.207	3.330		Mammoth
C2An.3n	3.330	3.596		
C2Ar	3.596	4.187	Gilbert	
C3n.1n	4.187	4.300		Cochiti
C3n.1r	4.300	4.493		
C3n.2n	4.493	4.631		Nunivak
C3n.2r	4.631	4.799		
C3n.3n	4.799	4.896		Sidufjall
C3n.3r	4.896	4.997		
C3n.4n	4.997	5.235		Thvera
C3r	5.235	6.033		
C3An.1n	6.033	6.252		
C3An.1r	6.252	6.436		
C3An.2n	6.436	6.733		
C3Ar	6.733	7.140		
C3Bn	7.140	7.212		
C3Br.1r	7.212	7.251		
C3Br.1n	7.251	7.285		
C3Br.2r	7.285	7.454		
C3Br.2n	7.454	7.489		
C3Br.3r	7.489	7.528		
C4n.1r	7.528	7.642		
C4n.1r	7.642	7.695		
C4n.2n	7.695	8.108		
C4n.1r	8.108	8.254		
C4n.1r	8.254	8.300		
C4n.2r	8.300	8.769		
C4An	8.769	9.098		
C4Ar.1r	9.098	9.312		
C4Ar.1n	9.312	9.409		
C4Ar.2r	9.409	9.656		
C4Ar.2n	9.656	9.717		
C4Ar.3r	9.717	9.779		
C5n.1n	9.779	9.934		
C5n.1r	9.934	9.987		
C5n.2n	9.987	11.040		
C5r.1r	11.040	11.118		
C5r.1n	11.118	11.154		
C5r.2r	11.154	11.554		
C5r.2n	11.554	11.614		
C5r.3r	11.614	12.014		
C5An.1n	12.014	12.116		
C5An.1r	12.116	12.207		
C5An.2n	12.207	12.415		
C5Ar.1r	12.415	12.730		
C5Ar.1n	12.730	12.765		
C5Ar.2r	12.765	12.820		
C5Ar.2n	12.820	12.878		
C5Ar.3r	12.878	13.015		
C5AAn	13.015	13.183		
C5AAr	13.183	13.369		
C5ABn	13.369	13.605		
C5ABr	13.605	13.734		
C5ACn	13.734	14.095		
C5ACr	14.095	14.194		
C5ADn	14.194	14.581		
C5ADr	14.581	14.784		
C5Bn.1n	14.784	14.877		
C5Bn.1r	14.877	15.032		
C5Bn.2n	15.032	15.160		
C5Br	15.160	15.974		
C5Cn.1n	15.974	16.268		
C5Cn.1r	16.268	16.303		
C5Cn.2n	16.303	16.472		
C5Cn.2r	16.472	16.543		
C5Cn.3n	16.543	16.721		
C5Cr	16.721	17.235		
C5Dn	17.235	17.533		
C5Dr	17.533	17.717		
C5Dr.1n	17.717	17.740		
C5Dr.2r	17.740	18.056		
C5En	18.056	18.524		
C5Er	18.524	18.748		
C6n	18.748	19.772		
C6r	19.772	20.040		
C6An.1n	20.040	20.213		
C6An.1r	20.213	20.439		
C6An.2n	20.439	20.709		
C6Ar	20.709	21.083		
C6AAn	21.083	21.159		
C6AAr.1r	21.159	21.403		
C6AAr.1n	21.403	21.483		
C6AAr.2r	21.483	21.659		
C6AAr.2n	21.659	21.688		
C6AAr.3r	21.688	21.767		
C6Bn.1n	21.767	21.936		
C6Bn.1r	21.936	21.992		
C6Bn.2n	21.992	22.268		
C6Br	22.268	22.564		
C6Cn.1n	22.564	22.754		
C6Cn.1r	22.754	22.902		
C6Cn.2n	22.902	23.030		
C6Cn.2r	23.030	23.249		
C6Cn.3n	23.249	23.375		
C6Cr	23.375	24.044		
C7n.1n	24.044	24.102		
C7n.1r	24.102	24.163		
C7n.2n	24.163	24.556		
C7r	24.556	24.919		
C7An	24.919	25.091		
C7Ar	25.091	25.295		
C8n.1n	25.295	25.444		
C8n.1r	25.444	25.492		
C8n.2n	25.492	26.154		
C8r	26.154	26.714		
C9n	26.714	27.826		
C9r	27.826	28.186		
C10n.1n	28.186	28.450		
C10n.1r	28.450	28.525		
C10n.2n	28.525	28.715		
C10.r	28.715	29.451		
C11n.1n	29.451	29.740		
C11n.1r	29.740	29.853		
C11n.2n	29.853	30.217		
C11r	30.217	30.627		
C12n	30.627	31.116		
C12r	31.116	33.266		
C13n	33.266	33.738		
C13r	33.738	34.782		
C15n	34.782	35.043		
C15r	35.043	35.404		
C16n.1n	35.404	35.567		
C16n.1r	35.567	35.707		

Table T5 (continued).

Chron	Age (Ma)		Alternate chron names	Subchrons
	Young	Old		
C16n.2n	35.707	36.276		
C16r	36.276	36.512		
C17n.1n	36.512	37.235		
C17n.1r	37.235	37.345		
C17n.2n	37.345	37.549		
C17n.2r	37.549	37.610		
C17n.3n	37.610	37.771		
C17r	37.771	38.032		
C18n.1n	38.032	38.975		
C18n.1r	38.975	39.041		
C18n.2n	39.041	39.464		
C18r	39.464	40.439		
C19n	40.439	40.671		
C19r	40.671	41.590		
C20n	41.590	42.774		
C20r	42.774	45.346		
C21n	45.346	47.235		
C21r	47.235	48.599		
C22n	48.599	49.427		
C22r	49.427	50.730		
C23n.1n	50.730	50.932		
C23n.1r	50.932	51.057		
C23n.2n	51.057	51.901		
C23r	51.901	52.648		
C24n.1n	52.648	53.004		
C24n.1r	53.004	53.116		
C24n.2n	53.116	53.167		
C24n.2r	53.167	53.286		
C24n.3n	53.286	53.808		
C24r	53.808	56.665		
C25n	56.665	57.180		
C25r	57.180	58.379		
C26n	58.379	58.737		
C26r	58.737	61.650		
C27n	61.650	61.938		
C27r	61.938	63.104		
C28n	63.104	64.128		
C28r	64.128	64.432		
C29n	64.432	65.118		
C29r	65.118	65.861		
C30n	65.861	67.696		
C30r	67.696	67.809		
C31n	67.809	68.732		
C31r	68.732	70.961		
C32n.1n	70.961	71.225		
C32n.1r	71.225	71.474		
C32n.2n	71.474	72.929		
C32r.1r	72.929	73.231		
C32r.1n	73.231	73.318		
C32r.2r	73.318	73.577		
C33n	73.577	79.543		
C33r	79.543	84.000		
C34n	84.000	124.610		

Note: Data from Gradstein et al. (2004).

Table T6. Wireline tool string downhole measurements, Expedition 318. (**See table notes.**)

Tool string	Tool	Measurement	Sampling interval (cm)	Approximate vertical resolution (cm)
Triple combination	HNGS	Spectral gamma ray	15	20–30
	GPIT	Tool orientation	3.8	15
	HLDS	Bulk density	2.5 and 15	38
	DIT	Resistivity	15	240/180/92
	APS	Porosity	5 and 15	36
Formation MicroScanner-sonic	HNGS	Spectral gamma ray	15	20–30
	GPIT	Tool orientation	3.8	15
	FMS	Microresistivity	0.25	0.5
	DSI	Acoustic velocity	15	107
Versatile Seismic Imager	SGT	Total gamma ray	5 and 15	30
	VSI	Acoustic traveltime	Stations at 25 m	NA

Notes: All tool and tool string names are trademarks of Schlumberger. NA = not applicable. For definitions of tool acronyms, see Table **T7**.

Table T7. Acronyms and units used for downhole wireline tools and measurements. (**See table note.**)

Tool	Output	Description	Unit
APS		Accelerator Porosity Sonde	
	APLC	Near/Array limestone porosity corrected	%
	STOF	Computed standoff	Inch
	SIGF	Formation capture cross section	Capture units
DIT		Dual Induction Tool	
	IDPH	Deep induction resistivity	Ωm
	IMPH	Medium induction resistivity	Ωm
	SFLU	Spherically focused resistivity	Ωm
DSI		Dipole Sonic Imager	
	DTCO	Compressional wave slowness (Δt)	µs/ft
	DTSM	Shear wave slowness (Δt)	µs/ft
FMS		Formation MicroScanner	
	C1, C2	Orthogonal hole diameters	Inch
	P1AZ	Pad 1 azimuth	%
		Spatially oriented resistivity images of borehole wall	
GPIT		General Purpose Inclinometer Tool	
	DEVI	Hole deviation	%
	HAZI	Hole azimuth	%
	F_x, F_y, F_z	Earth's magnetic field (three orthogonal components)	%
	A_x, A_y, A_z	Acceleration (three orthogonal components)	m/s^2
HLDS		Hostile Environment Litho-Density Sonde	
	RHOM	Bulk density	g/cm^3
	PEFL	Photoelectric effect	b/e^-
	LCAL	Caliper (measure of borehole diameter)	Inch
	DRH	Bulk density correction	g/cm^3
HNGS		Hostile Environment Natural Gamma Ray Sonde	
	HSGR	Standard (total) gamma ray	gAPI
	HCGR	Computed gamma ray (HSGR minus uranium contribution)	gAPI
	HFK	Potassium	wt%
	HTHO	Thorium	ppm
	HURA	Uranium	ppm
SGT		Scintillation Gamma Ray Tool	
	GR	Total gamma ray	gAPI
	ECGR	Environmentally-corrected gamma ray	gAPI
	EHGR	High-resolution environmentally-corrected gamma ray	gAPI
VSI		Versatile Seismic Imager	
		Acoustic travel time	ms

Note: For the complete list of acronyms used in IODP and for additional information about tool physics, consult IODP-USIO Science Services, LDEO, at **iodp.ldeo.columbia.edu/TOOLS_LABS/tools.html.**